NCGT
Accept Nothing on Authority

An International Journal for
New Concepts in Global Tectonics

Volume 12
Number 1
March 2024

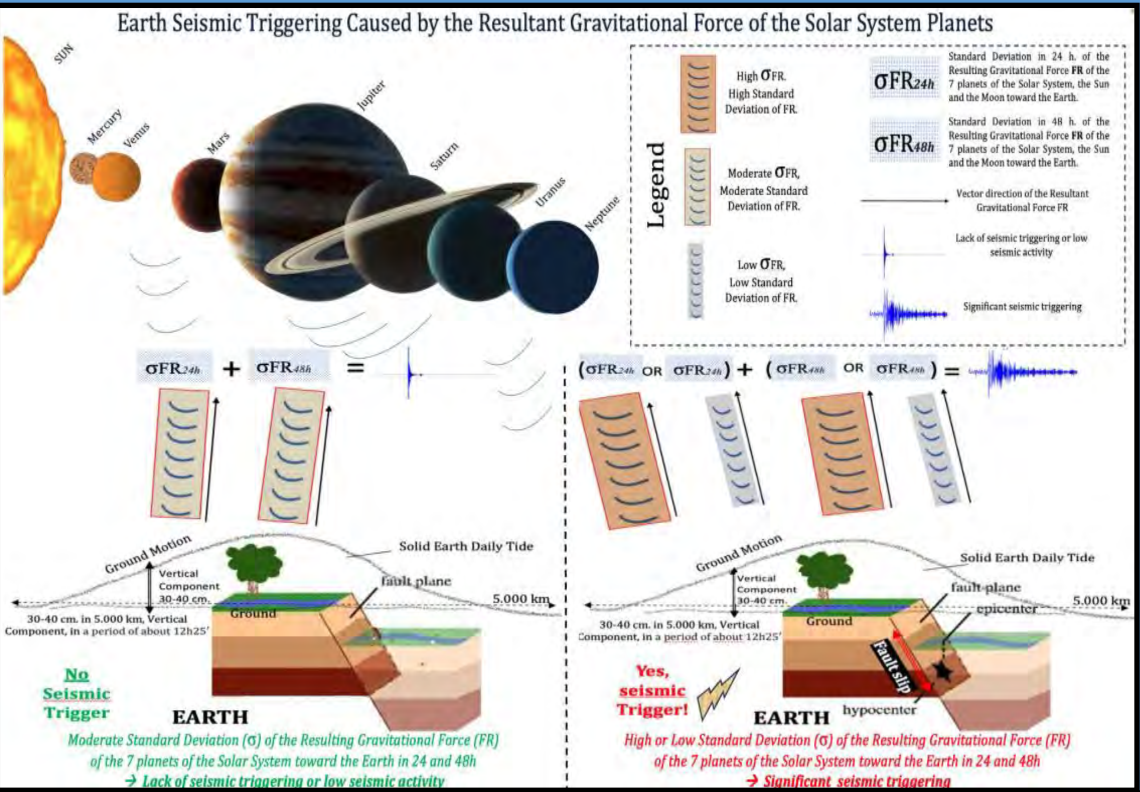

A Collective Gravitational Focus for Earthquakes

NCGT Journal Volume 12, Number 1, March 2024, ISSN 2202-0039

Editor-in-Chief: Louis HISSINK (louis.hissink@outlook.com)

Contents

For donations please feel free to contact the Research Director of the Geoplasma Research Institute, Mr. Bruce Leybourne, at leybourneb@iascc.org. For contact, correspondence, or inclusion of material in the NCGT Journal please use the following methods: *NEW CONCEPTS IN GLOBAL TECTONICS.* 1. E-mail: louis.hissink@outlook.com (files in MS Word or ODT format, and figures in png, gif, bmp or tif format) as separate files; 3. Telephone, +61 402 509 420. *DISCLAIMER*: The opinions, observations and ideas published in this journal are the responsibility of the contributors and do not necessarily reflect those of the Editor and the Editorial Board. *NCGT Journal* is a refereed quarterly international online journal and appears in March, June, September and December. *ISSN number*; ISSN 2202-0039

Space weather related to potentially destructive seismic activity that has been recorded globally between 2012 and 2023

Valentino Straser[1], Gabriele Cataldi[2], Daniele Cataldi[2-3]

(1) Department of Science and Environment UPKL Brussel (B). valentino.straser@gmail.com
(2) Radio Emissions Project (I). ltpaobserverproject@gmail.com
(3) Fondazione Permanente G. Giuliani - Onlus (I). daniele77c@hotmail.it

Abstract

The analysis of space weather has allowed the authors to understand the existence of a close correlation between variations in the solar proton flux (increases) and potentially destructive seismic activity (M6+) that has been recorded on a global scale since 2012. This study will present the results of twelve years of observations that the authors have conducted on solar activity and potentially destructive seismic activity that has been recorded on a global scale between 2012 and 2023.

Keywords: space weather, proton density, seismic precursors, potentially destructive seismic events, solar ion flux.

Introduction

Between January 1, 2012 and December 31, 2023, 1567 potentially destructive seismic events with magnitude (Mw) 6 or higher were recorded on our planet (Fig. 1). On average, about 131 seismic events are recorded per Year. During this period, the Earth was impacted by varying intensities of solar proton flux increases, which were followed by potentially destructive seismic events on a global scale. On average, each proton flux increase is followed by 2.87 strong seismic events (M6+), while approximately 99 hours pass on average between the start of the proton flux increase and the potentially destructive seismic events associated with it.

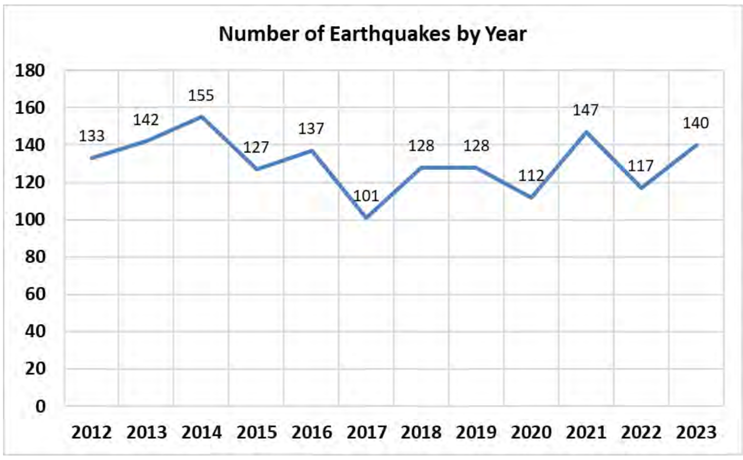

Fig. 1 – Distribution of potentially destructive seismic events (M6+) recorded on a global scale between 2012-2023*. In the chart at the top, the annual distribution of potentially destructive seismic events recorded on a global scale is visible. Credit: Radio Emissions Project.*

These are the results of the most extensive study ever conducted by man on space weather related to potentially destructive seismic activity [1-45].

Methods and data

This study analyzed 1567 destructive seismic events recorded globally between January 1, 2012, and December 31, 2023. The catalog on potentially destructive seismic activity (M6+) was provided by the USGS (United States Geological Survey), and the data on the M6+ activity to conduct this study were collected almost

in real time. However, it is possible that over longer time frames, some data have been updated or the number of potentially destructive seismic events has changed due to more precise analyses conducted on the energy released by the seismic events.
To determine whether there is a strong correlation between increases in solar ionic flux and potentially destructive seismic activity recorded on a global scale, the authors conducted a detailed analysis of the proton variation curve of the solar wind, utilizing data provided by two artificial satellites located in Lagrangian orbit:

a) Advanced Composition Explorer (ACE) Satellite;
b) Deep Space Climate Observatory (DSCOVR) Satellite.

More specifically, the data analyzed by the authors were the following:

ACE Satellite:

- differential proton flux 1060-1900 keV (p/cm^2-sec-ster-MeV);
- differential proton flux 761-1220 keV (p/cm^2-sec-ster-MeV);
- differential proton flux 310-580 keV (p/cm^2-sec-ster-MeV).

DSCOVR Satellite:

- proton density (p/cm^3).

Discussion

Studies conducted by the authors in 2011 on the characteristics of the solar wind have revealed that variations in the proton density of the solar wind are always correlated with an increase in potentially destructive seismic activity observed on a global scale. The variation of the interplanetary magnetic field (IMF), the magnitude of the dynamic pressure of the solar wind, or the temperature of the solar ionic flux, are not always events that can be correlated with a resurgence of global seismic activity M6+. For now, the only phenomenon that has proven to be reliable in the context of this type of correlation is represented solely by variations in the proton density of the solar ionic flux.

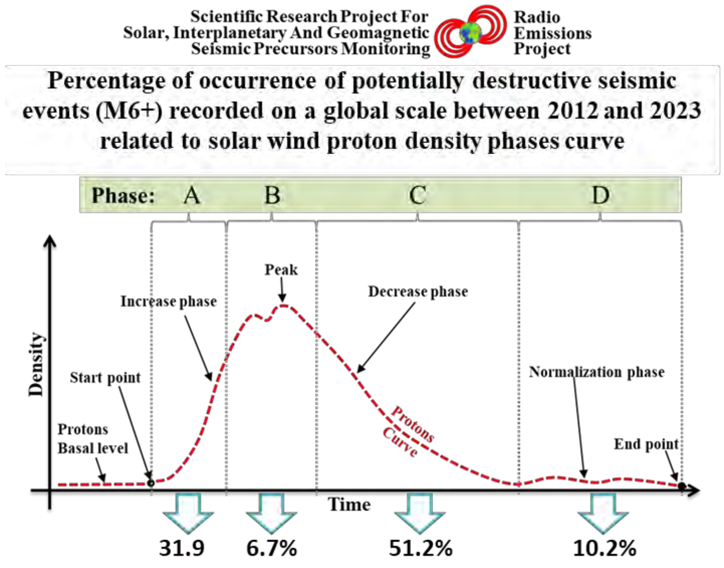

Fig. 2 – Distribution of potentially destructive seismic events (M6+) recorded on a global scale with respect to the proton variation curve*. In the graph above the typical proton curve of a "gradual" type event has been reproduced. The authors divided the variation curve into four distinct phases to simplify the description in relation to the correlation data with the M6+ global seismic activity provided by the study. Credits: Radio Emissions Project.*

In the study conducted by the authors between 2012 and 2023 it was clarified that potentially destructive seismic events occurring on a global scale are distributed in different percentages along the proton variation curve (Fig. 2): most earthquakes (51.2%) are recorded during the reduction phase (phase C) of the proton density, while another large percentage (31.9%) occurs during the initial phase of increasing proton density (phase A). Therefore, more than 83.1% of potentially destructive seismic events are recorded while the density of the solar proton flux increases or decreases. Instead, 10.2% of potentially destructive seismic events are recorded during the stabilization phase of the proton density, a phase in which the proton density level will slowly return to pre-increase levels.

Scientific Research Project For
Solar, Interplanetary And Geomagnetic
Seismic Precursors Monitoring
Radio
Emissions
Project

Distribution of the number of seismic events (M6+) recorded globally between 2012 and 2023 in relation to the phases of increase in the proton density of the solar wind.

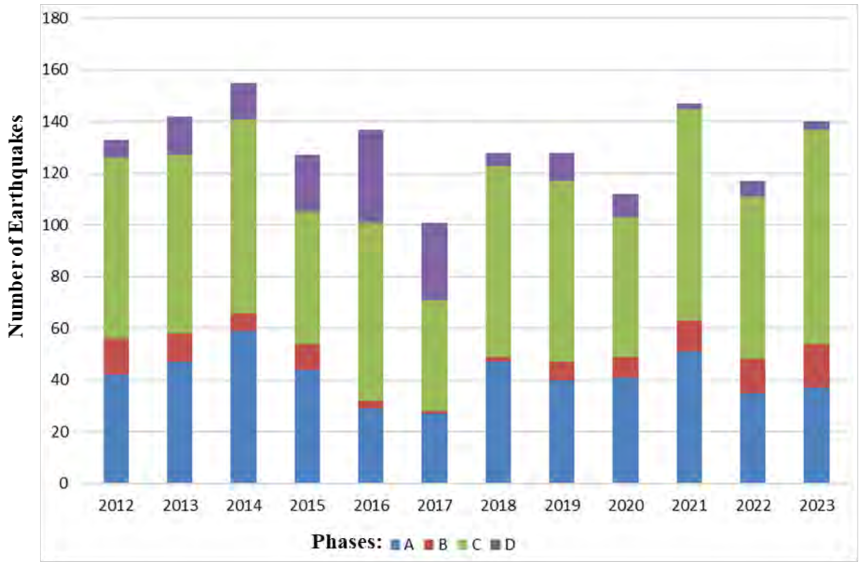

Fig. 3 – Distribution of the number of seismic events (M6+) in relation to the phases of increase in the proton density of the solar wind*. In the graph, it is possible to observe the distribution of potentially destructive earthquakes in relation to the characteristics of the proton variation curve visible in Fig. 2. Credits: Radio Emissions Project.*

Observing Fig. 3, it is possible to understand that the number of earthquakes correlated with the different phases of proton variation maintains a certain regularity over the years: phase C is the one during which more earthquakes occur compared to the other phases; phase A is the second in terms of the number of earthquakes; phase D is the third in terms of the number of earthquakes, and finally, phase B is the last in terms of the number of earthquakes. This suggests that most seismic events occur during a variation (increase or decrease) in the proton density of the solar wind, while the smallest number of earthquakes (16.9%) occurs when the variation curve does not show significant and prolonged oscillations.

As proposed by the authors, the reason could be traced back to a form of electromagnetic interaction as a seismogenic cause induced by the variation in the density of the solar ionic flux. This interaction might affect the superficial layers of the Earth's crust where the formation of electronic currents due to tectonic stress caused by geodynamics is possible. The formation of these electrical charges, being within the Earth's magnetic field (a magnetic field that is not static, but variable over time and influenced by the density of the solar ionic flux), could, through the Lorentz force, contribute to altering the static equilibrium of faults.

This would also explain why more potentially destructive seismic events are observed during phases A and C rather than during phases B and D (Fig. 2): when the intensity of the Earth's magnetic field is greater, the Lorentz force will also be greater. When the intensity of the Earth's magnetic field oscillates rapidly, the

Lorentz force will also exhibit rapid oscillations. All this would explain why an increase in global seismic activity M6+ is observed during a disturbance of the Earth's geomagnetic field.

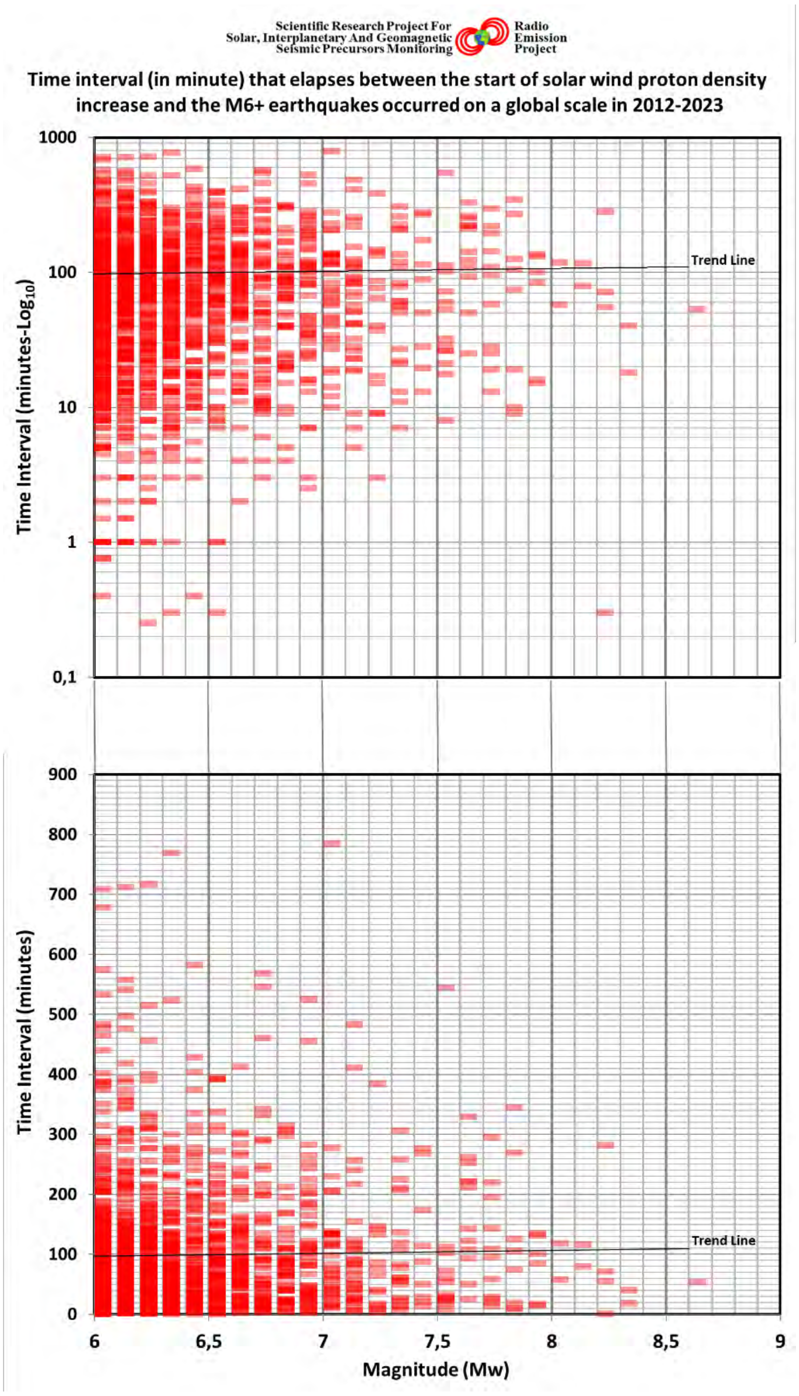

***Fig. 4 – Distribution of time intervals**. In the chart above, it is possible to observe the distribution of time intervals recorded between the beginning of the protonic increase of the solar wind and the potentially destructive seismic events related to the ionic increase. The data sample used corresponds to 1,567 potentially destructive seismic events recorded on a global scale. Credits: Radio Emissions Project.*

The study also allowed for the measurement of so-called "time intervals" that occurred between the start of the protonic increase of the solar wind and the seismic events associated with it. On average, each increase in the solar ionic flux is followed by 2.87 potentially destructive seismic events; meanwhile, the average recorded time interval is equivalent to 99 hours (4.13 days) (Fig. 4). The start of the increase in the solar ionic flux has been identified as the baseline level that the density of the solar ionic flux assumes between phase D and phase A of the proton variation curve (Fig. 2).

Conclusions

The study conducted by the authors has confirmed that there is a close relationship between the increase in solar ionic flux and potentially destructive seismic activity (M6+) recorded on a global scale. The analysis of the proton variation curve of the solar wind, its temporal modulation, has made it possible to understand that the potentially destructive seismic activity recorded globally follows a specific distribution relative to the proton variation curve (Fig. 2), and this finding cannot be explained as a causal distribution of earthquakes. The authors have repeatedly proposed that the basis of this distribution is a form of electromagnetic interaction between the solar ionic flux and the potentially destructive seismic activity recorded globally (see previous chapter).

The observed phenomenon has predictive potentials that have never been observed in any other phenomenon of solar or terrestrial origin, and it is evident that it would be possible to use the data obtained by the authors within the framework of an innovative seismic prediction project, not based on statistical data.

Credits

[1] G. Cataldi, D. Cataldi, V. Straser. (2013). Variations Of Terrestrial Geomagnetic Activity Correlated To M6+ Global Seismic Activity. EGU (European Geosciences Union) 2013, General Assembly, Seismology Section (SM3.1), Earthquake precursors, bio-anomalies prior to earthquakes and prediction, Geophysical Research Abstracts, Vol. 15. EGU2013-2617, Vienna, Austria.

[2] G. Cataldi, D. Cataldi and V. Straser. (2014). Earth’s magnetic field anomalies that precede the M6+ global seismic activity. European Geosciences Union (EGU) General Assembly 2014, Geophysical Research Abstract, Vol. 16, EGU2014-1068, Vienna, Austria.

[3] D. Cataldi, G. Cataldi and V. Straser. (2014). Variations of the Electromagnetic field that preceded the Peruvian M7.0 earthquake occurred on September 25, 2013. European Geosciences Union (EGU) General Assembly 2014, Geophysical Research Abstract, Vol. 16, EGU2014-1075, Natural Hazard Section (NH4.3), Electro-magnetic phenomena and connections with seismo-tectonic activity, Vienna, Austria.

[4] T. Rabeh, G. Cataldi, V. Straser. (2014). Possibility of coupling the magnetosphere–ionosphere during the time of earthquakes. European Geosciences Union (EGU) General Assembly 2014, Geophysical Research Abstract, Vol. 16, EGU2014-1067, Vienna, Austria.

[5] V. Straser, G. Cataldi. (2014). Solar wind proton density increase and geomagnetic background anomalies before strong M6+ earthquakes. Space Research Institute of Moscow, Russian Academy of Sciences, MSS-14. 2014. Moscow, Russia. pp280-286.

[6] V. Straser, G. Cataldi. (2015). Solar wind ionic variation associated with earthquakes greater than magnitude M6.0. New Concepts in Global Tectonics Journal, V. 3, No. 2, June 2015, Australia. P.140-154.

[7] G. Cataldi, D. Cataldi, V. Straser. (2015). Solar wind proton density variations that preceded the M6+ earthquakes occurring on a global scale between 17 and 20 April 2014. European Geosciences Union (EGU) General Assembly 2015, Geophysical Research Abstract, Vol. 17, EGU2015-4157-2, Vienna, Austria.

[8] G. Cataldi, D. Cataldi, V. Straser. (2015). Solar wind ion density variations that preceded the M6+ earthquakes occurring on a global scale between 3 and 15 September 2013. European Geosciences Union (EGU) General Assembly 2015, Geophysical Research Abstract, Vol. 17, EGU2015-4581, Vienna, Austria.

[9] G. Cataldi, D. Cataldi, V. Straser. (2015). Solar wind proton density variations that preceded the M6,1 earthquake occurred in New Caledonia on November 10, 2014. European Geosciences Union (EGU) General Assembly 2015, Geophysical Research Abstract, Vol. 17, EGU2015-4167, Vienna, Austria.

[10] V. Straser, G. Cataldi, D. Cataldi. (2015). Solar wind ionic and geomagnetic variations preceding the Md8.3 Chile Earthquake. New Concepts in Global Tectonics Journal, V. 3, No. 3, September 2015, Australia. P.394-399.

[11] G. Cataldi, D. Cataldi, V. Straser. (2016). Solar activity correlated to the M7.0 Japan earthquake occurred on April 15, 2016. New Concepts in Global Tectonics Journal, V. 4, No. 2, pp202-208, June 2016.

[12] G. Cataldi, D. Cataldi, V. Straser. (2016). Tsunami related to solar and geomagnetic activity. European Geosciences Union (EGU) General Assembly 2016, Natural Hazard Section (NH5.6), Complex modeling of earthquake, landslide, and volcano tsunami sources. Geophysical Research Abstract, Vol. 18, EGU2016-9626, Vienna, Austria.

[13] G. Cataldi, D. Cataldi, V. Straser. (2017). SELF-VLF electromagnetic signals and solar wind proton density variations that preceded the M6.2 Central Italy earthquake on August 24, 2016. International Journal of Modern Research in Electrical and Electronic Engineering, Vol. 1, No. 1, 1-15. DOI: 10.20448/journal.526/2017.1.1/526.1.1.15.

[14] G. Cataldi, D. Cataldi, V. Straser. (2017). Solar wind proton density increase that preceded Central Italy earthquakes occurred between 26 and 30 October 2016. European Geosciences Union (EGU), General Assembly 2017. Geophysical Research Abstracts Vol. 19, EGU2017-3774, 2017, Vienna, Austria.

[15] V. Straser, G. Cataldi, D. Cataldi. (2017). Solar and electromagnetic signal before Mexican Earthquake M8.1, September 2017. New Concepts in Global Tectonics Journal, V. 5, No. 4, December 2017. pp600-609.

[16] G. Cataldi, D. Cataldi, V. Straser. (2017). Solar and Geomagnetic Activity Variations Correlated to Italian M6+ Earthquakes Occurred in 2016. EGU General Assembly 2017. EGU2017-3681, Vol. 19. Vienna, Austria.

[17] G. Cataldi, D. Cataldi, V. Straser. (2019). Solar wind ionic density variations related to M6+ global seismic activity between 2012 and 2018. European Geosciences Union (EGU) General Assembly 2019, Geophysical Research Abstract, Vol. 21, EGU2019-3067, 2019, Vienna, Austria.

[18] V. Straser, G. Cataldi, D. Cataldi. (2019). Namazu’s Tail – RDF: a new perspective for the study of seismic precursors of Japan. Lulu Editore, 2019.

[19] G. Cataldi. (2020). Precursori Sismici – Monitoraggio Elettromagnetico. Kindle-Amazon, ISNB: 9798664537970. ASIN Code: B08CPDBGX9.

[20] G. Cataldi, D. Cataldi, V. Straser. (2019). Wolf Number Related To M6+ Global Seismic Activity. New Concepts in Global Tectonics Journal, Volume 7, Number 3, December 2019, pp178-186.

[21] V. Straser, G. Cataldi, D. Cataldi. (2020). The Space Weather Related to the M7+ Seismic Activity Recorded on a Global Scale between 28 January and 25 March 2020. Acta Scientific Agriculture 4.12 (2020): pp55-62.

[22] G. Cataldi, V. Straser, D. Cataldi. (2020). Space weather related to potentially destructive seismic activity recorded on a global scale. New Concepts in Global Tectonics Journal. Vol.8, No.3, pp233-253, December 2020. ISSN 2202-0039.

[23] G. Cataldi. (2021). Radio Emissions Project – A new approach to seismic prediction. Kindle-Amazon, ISNB: 9798709593411.

[24] G. Cataldi, D. Cataldi, V. Straser. (2021). Space weather and geomagnetic activity related to the Japan M7.1 earthquake recorded on February 13, 2021. New Concepts in Global Tectonics Journal, Vol. 9, No. 1, pp16-23. March 2021.

[25] G. Cataldi, D. Cataldi, V. Straser. (2021). Space weather and geomagnetic activity related to the Chilean M6.7 earthquake recorded on February 3, 2021. New Concepts in Global Tectonics Journal, Vol. 9, No. 1, pp3-9. March 2021.

[26] G. Cataldi, D. Cataldi, V. Straser. (2021). Space weather and geomagnetic activity related to M6+ global seismic activity recorded on February 7, 2021. New Concepts in Global Tectonics Journal, Vol. 9, No. 1, pp24-30. March 2021.

[27] G. Cataldi, D. Cataldi, V. Straser. (2021). Space Weather and geomagnetic activity related to Ecuadorean M7.5 earthquake recorded on February 22, 2019. New Concepts in Global Tectonics Journal, Vol. 9, No. 2, pp79-86. June 2021.

[28] G. Cataldi, D. Cataldi, V. Straser. (2021). Solar Activity and geomagnetic activity related to M6+ global seismic activity recorded on March 20, 2021. New Concepts in Global Tectonics Journal, Vol. 9, No. 2, pp87-93. June 2021.

[29] G. Cataldi, D. Cataldi, V. Straser. (2021). Space weather and geomagnetic activity related to M6+ global seismic activity recorded on 3-4 March 2021. New Concepts in Global Tectonics Journal, Vol. 9, No. 2, pp94-98. June 2021.

[30] G. Cataldi, D. Cataldi, V. Straser. (2021). Solar activity and geomagnetic activity related to M6.0 South Sandwich Islands region earthquake recorded March 14, 2021. New Concepts in Global Tectonics Journal, Vol. 9, No. 2, pp99-105. June 2021.

[31] G. Cataldi, D. Cataldi, V. Straser. (2021). Space weather and geomagnetic activity related to the Vanuatu M6.3 earthquake recorded on March 20, 2019. New Concepts in Global Tectonics Journal, Vol. 9, No. 2, pp106-111. June 2021.

[32] G. Cataldi, D. Cataldi, V. Straser. (2021). Space weather and geomagnetic activity related to M6+ earthquakes recorded between 7 and 20 November 2017. New Concepts in Global Tectonics Journal, Volume 9, Number 3, September 2021. pp137-144. ISSN 2202-0039.

[33] G. Cataldi, D. Cataldi, V. Straser. (2021). Space weather and geomagnetic activity related to M6+ earthquakes recorded between 12 and 15 April 2012. New Concepts in Global Tectonics Journal, Volume 9, Number 3, September 2021. Pp145-154. ISSN 2202-0039.

[34] G. Cataldi, D. Cataldi, V. Straser. (2021). Space weather and geomagnetic activity related to M6+ earthquakes recorded between 13 and 16 April 2016. New Concepts in Global Tectonics Journal, Volume 9, Number 3, September 2021. pp158-163. ISSN 2202-0039.

[35] G. Cataldi, D. Cataldi, V. Straser. (2021). Space weather and geomagnetic activity related to M6+ earthquakes recorded between 17 and 19 July 2017. New Concepts in Global Tectonics Journal, Volume 9, Number 3, September 2021. pp164-169. ISSN 2202-0039.

[36] G. Cataldi, D. Cataldi, V. Straser. (2021). Space weather related to M6+ earthquakes recorded on June 24, 2019. New Concepts in Global Tectonics Journal, Volume 9, Number 3, September 2021. pp132-136. ISSN 2202-0039.

[37] G. Cataldi, V. Straser, D. Cataldi. (2021). Space weather related to M6.1 Indonesia earthquake recorded on June 3, 2021. New Concepts in Global Tectonics Journal. Volume 9, No 4, December 2021. Pp 185-193.

[38] G. Cataldi, V. Straser, D. Cataldi. (2021). Space weather related to M6.0 Tonga earthquake recorded on March 17, 2020. New Concepts in Global Tectonics Journal. Volume 9, No 4, December 2021. Pp 206-214.

[39] G. Cataldi, V. Straser, D. Cataldi. (2021). Space weather related to M8.2 earthquake recorded in Alaska on 29 July 2021. New Concepts in Global Tectonics Journal. Volume 9, No 4, December 2021. Pp 194-205.

[40] D. Cataldi, E. Cavina, G. Cataldi, V. Straser. (2022). Reverse Migration of the Wood Pigeons and electromagnetic emissions, before the Mw 3.7 earthquake occurred in Visso-Macerata, Central Italy on October 18, 2021. iJournals: International Journal of Social Relevance & Concern (IJSRC), ISSN-2347-9698, Volume 10, Issue 1 January 2022. pp. 24-40.

[41] V. Straser, D. Cataldi, G. Cataldi. (2022). Pre-seismic phenomena that preceded the M7.0 earthquake recorded in Acapulco (Mexico) on September 8, 2021. iJournals: International Journal of Social Relevance & Concern (IJSRC), ISSN-2347-9698, Volume 10, Issue 1 January 2022. pp. 41-57.

[42] . Straser, G. Cataldi, D. Cataldi. (2022). Space weather related to M6+ potentially destructive seismic events recorded on a global scale between 13 and 16 March 2022. New Concepts in Global Tectonics Journal. Volume 10, Number 1, March 2022. ISSN 2202-0039. pp. 3-10.

[43] V. Straser, G. Cataldi, D. Cataldi. (2022). Space weather related to M6+ potentially destructive seismic events recorded on a global scale between 2012 and 2021. New Concepts in Global Tectonics Journal. Volume 10, Number 1, March 2022. ISSN 2202-0039. pp. 11-21.

[44] V. Straser, D. Cataldi, G. Cataldi. (2023). Weather Events Associated with Strong Earthquakes and Seismic Swarms in Italy. Advances in Geological and Geotechnical Engineering Research. Volume 05, Issue 03, Pp 39-54. July 2023.

[45] V. Straser, G. Cataldi, D. Cataldi. (2023). Magnitude of potentially destructive earthquakes recorded in Mexico correlated to the extent of the solar proton flux. New Concepts In Global Tectonics Journal. Vol 11, N 4, December 2023. ISSN 2202-0039. Pp 261-266.

Solar Activity and Electromagnetic Signals that preceded the M7.5 Earthquake of January 1, 2024, in Japan

Daniele Cataldi[1-2], Gabriele Cataldi[1], Valentino Straser[3]

(1) Radio Emissions Project (I). ltpaobserverproject@gmail.com
(2) LTPA Observer Project (I). daniele77c@hotmail.it
(3) Department of Science and Environment UPKL Brussel (B). valentino.straser@gmail.com

Abstract

On January 1, 2024, a strong earthquake occurred in Japan, causing deaths and damage to Japanese infrastructure. This study discusses the electromagnetic and solar signals that anticipated the strong earthquake. This earthquake was preceded by a series of electromagnetic signals recorded by the RDF network developed by the Radio Emissions Project in Italy and by peculiar solar activity that occurred in the days before the disastrous quake. The authors believe that there may be a relationship linking telluric activity with space weather, evidenced by electromagnetic signals detectable in the phases preceding the earthquake in a time window of about five days. The results of the experiment show that the data can be compared with other known cases in the scientific literature, in the context of a crustal diagnosis and seismic precursor candidates.

Keywords: Japan Earthquake, Electromagnetic Seismic Precursors, Earthquake Precursors, Radio Direction Finding, Solar Activity.

1 - Introduction

The issue of safety to protect communities, infrastructure, and to contain the economic damages resulting from destructive seismic events has led research to investigate physical, chemical, and biological signals, now also employing artificial satellites and AI, to mitigate the impact of earthquakes. Research on seismic precursor candidates covers an extremely broad field of study, with numerous precursor phenomena historically classified and experimented by international research teams. In recent years, the Radio Emissions Project, based in Rome, Italy, has conducted multiple studies on electromagnetic precursor phenomena that seem to be associated with endogenous, seismic, and volcanic activity. These electromagnetic precursor phenomena appear to be mediated by solar activity [1][2][3], which in this context seems to facilitate seismic triggering on a global scale. [4] [5] [6] [15] [16] [17] [18] [19] [20] [21]

Since 2017, the Radio Emissions Project has established an electromagnetic monitoring network (RDF), based on radio receiving stations that use Radio Direction Finding technology, capable of detecting the direction of arrival of electromagnetic signals and measuring their intensity and behavior over time. [7]

The experimentation of this detection network has shown that before strong earthquakes there are recurrent local emissions, emitted in a geographical area, identified as the future epicentral zone of an impending earthquake [8] [9] [10].

The same investigative methodology was applied to the Japanese earthquake, thanks to the 24/7 data detection of RDF signals from the respective network monitoring stations, and the retrieval of data from the spaceweather website to perform a real-time comparison with electromagnetic data.

2 - Method and Data

The method used to compile this study is that of comparison, while the electromagnetic detection data come from the recordings made by the Italian RDF network:

1. RDF Station in Pontedera PI, located in Northern Italy.
2. RDF Station in Lariano RM, located in Central Italy.

Both stations provided evidence of clear natural signals, originating from the geographic area where the earthquake occurred. The seismic data examined in this study are those of the USGS (https://www.usgs.gov/), updated and temporally related to the evidence of electromagnetic signals highlighted by the Italian RDF network. The space weather data were retrieved from the institutional website iSWA (https://iswa.ccmc.gsfc.nasa.gov/IswaSystemWebApp/) and from satellites.

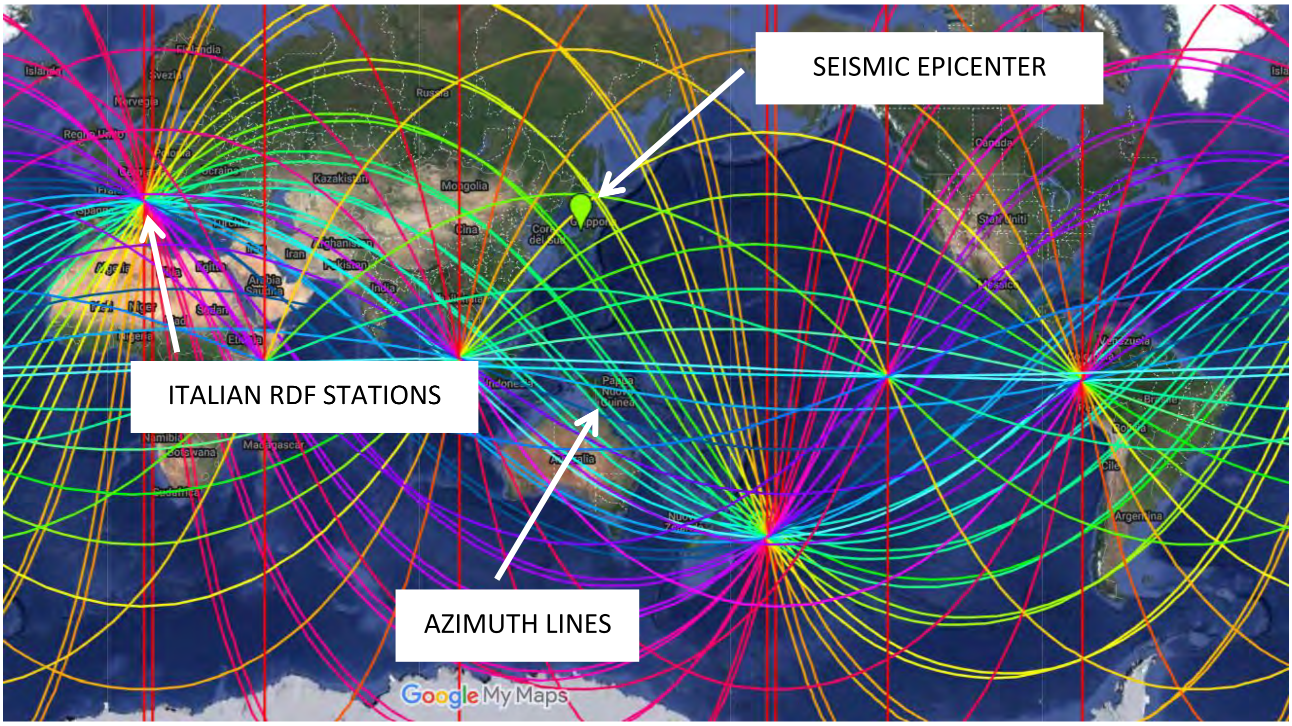
SEISMIC EPICENTER

ITALIAN RDF STATIONS

AZIMUTH LINES

Fig. 1 - Colorimetric Map of the Global RDF Network developed by the Radio Emissions Project, which shows the presence of the Japanese seismic epicenter (in green). The colored lines represent the azimuths relative to the various RDF stations located globally, including those in Italy. Credits: Radio Emissions Project; Google My Maps.

The first electromagnetic recordings made by the Italian RDF network, related to the precursory signals of the Japanese earthquake, were registered from November 1, 2023, at around 11:00 UTC (Fig. 2) by the Pontedera PI RDF station. These signals, appearing suddenly for the first time in a period when there had been no evidence of such radio emissions, were extremely evident compared to the normal natural electromagnetic background, lasting about 2.4 hours.

The emissions reappeared around 17:30 UTC on November 1, 2023 (Fig. 3), this time lasting approximately 3.3 hours. The electromagnetic signals continued to appear for days and weeks until December 6, 2023 (Fig. 4), when an extensive electromagnetic emission, also from the azimuth in yellow relative to the Pontedera PI station, was observed. It started at 06:00 UTC and lasted until about 12:00 UTC, with a duration of a full 6 hours. This signal was again centered around 13 kHz. From this date, electromagnetic signals with a yellow azimuth became increasingly frequent. On December 14, 2023 (Fig. 5), the signals remained extremely interesting, this time a signal on the yellow azimuth from the Pontedera PI station appeared at 14:00 UTC, 18:35 UTC, lasting 4.5 continuous hours. This signal was preceded and followed by other intense electromagnetic emissions with different azimuths. The signals continued for several more days, indicating an ongoing accumulation of crustal energy in an area located on the yellow azimuth. Ten days later, specifically on December 24, 2023 (Fig. 6), a new extensive electromagnetic emission was recorded, lasting 4.1 hours, starting at 07:40 UTC, and ending around 12:00 UTC.

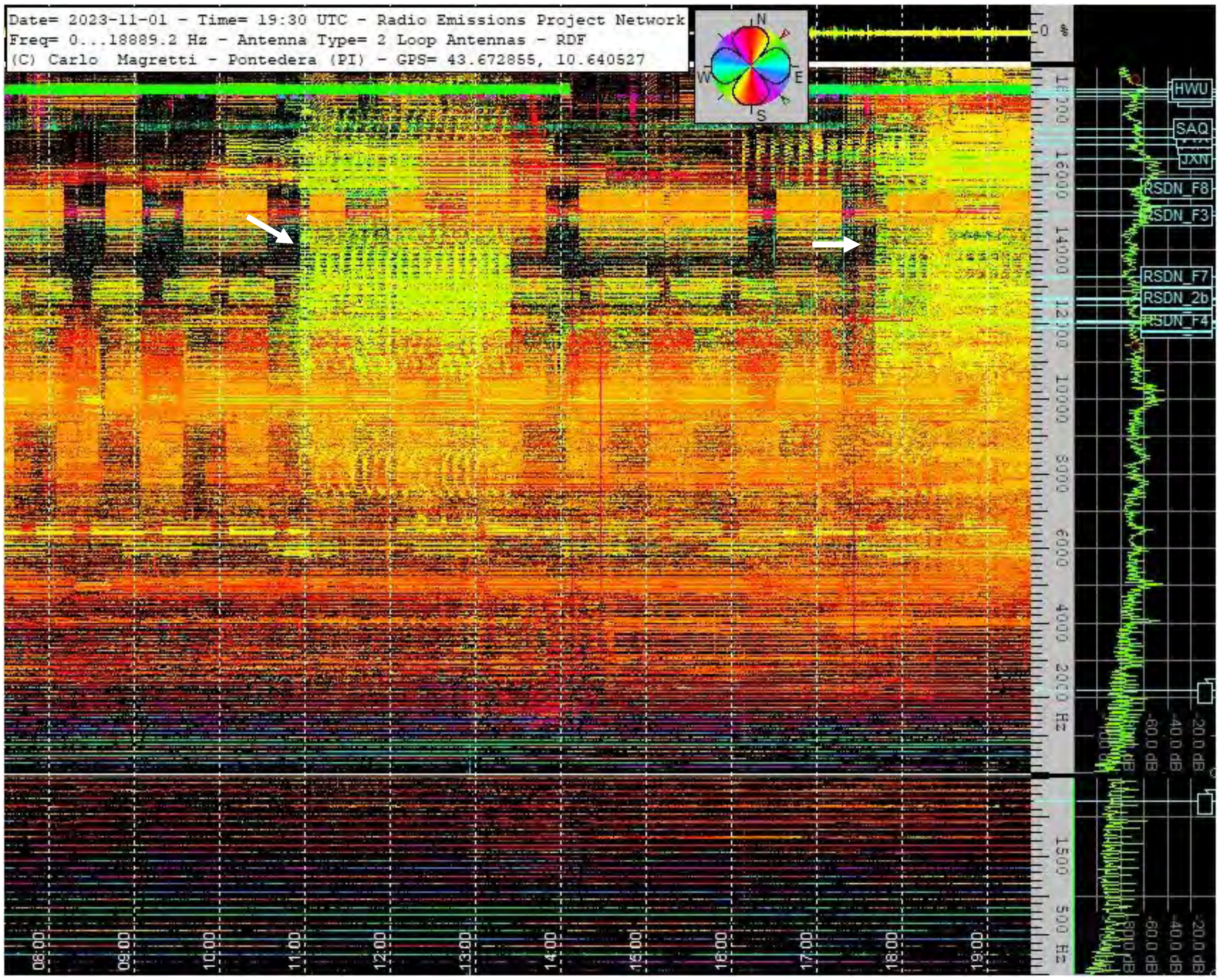

Fig. 2 – Dynamic Spectrogram recorded by the Pontedera PI RDF station, managed by Carlo Magretti, which highlights the presence of strong electromagnetic signals on the yellow azimuth, appearing at an average electromagnetic frequency of 13 kHz. Credits: Radio Emissions Project; Carlo Magretti.

The electromagnetic emissions recorded by the Pontedera PI station proved to be extremely interesting to the research group, who noted the evolution of these signals that were previously invisible but now seem to increase in repetitiveness. On December 31, 2023 (Fig. 7), the electromagnetic signals recorded by the Pontedera PI RDF station reappeared at 08:00 UTC and ended around 11:10 UTC, with a total duration of the emissions of 3.1 hours. In this case, too, this radio signal was important in a predictive context, preceded by other electromagnetic appearances at the same frequency (13 kHz).

On January 1, 2024 (Fig. 8) at 07:10:09 (UTC), a strong earthquake struck Japan with a magnitude of Mw 7.5, causing deaths and the collapse of some homes. This event caused significant damage to Japanese infrastructure. In the recorded spectrogram, a faint reddish emission is visible at the moment the strong earthquake occurred, but there were no other electromagnetic emissions indicating the yellow azimuth. Only subsequently (a few hours later) were there other electromagnetic signals with the same azimuth, probably produced by the Earth's crust near the seismic hypocenter, under significant energetic increase (tectonic stress). The RDF station in Lariano RM also recorded an intense emission, not preceded and not followed by other similar emissions, which had alerted the researchers involved in this study. The emission visible in Fig. 9.

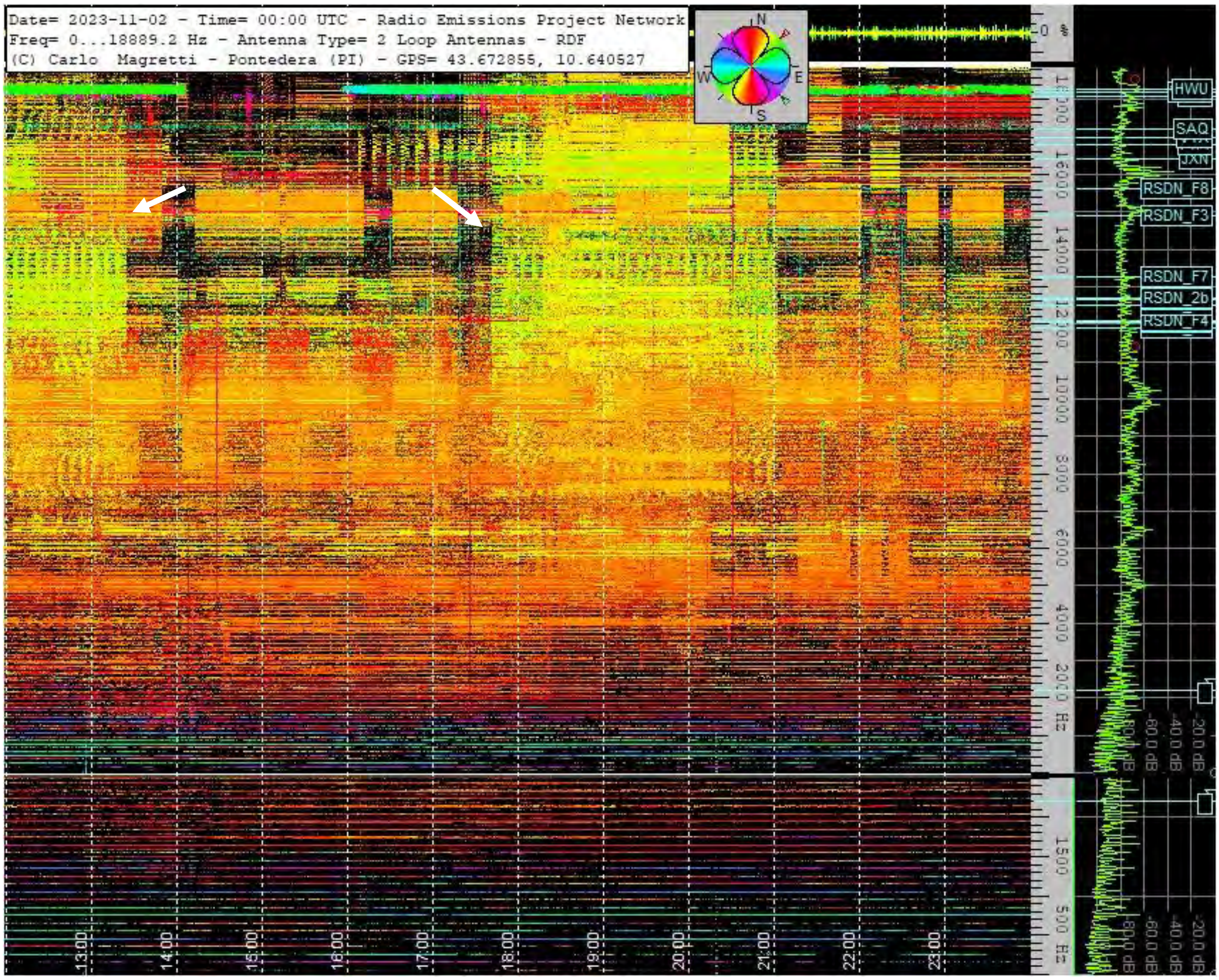

Fig. 3 – Dynamic Spectrogram recorded by the Pontedera PI RDF station, managed by Carlo Magretti, which highlights the presence of strong electromagnetic signals on the yellow azimuth, appearing at an average electromagnetic frequency of 13 kHz. Credits: Radio Emissions Project; Carlo Magretti.

On December 29, 2023 (Fig. 9), the Lariano RM RDF station highlighted the presence of a strong electromagnetic emission, appearing around 18:00 UTC and lasting until approximately 20:35 UTC, with an electromagnetic frequency ranging from 0.0 Hz to 1 Hz, and repeated resonance harmonics reaching up to 4 Hz. This evidently 'anomalous' signal aroused interest among the research group involved in this study, given that the green azimuth had not appeared for weeks.

On January 1, 2024 (Fig. 10), the Lariano RM RDF station again showed the appearance of electromagnetic signals on the green azimuth. As visible in Fig. 10, around 23:00 UTC on December 31, 2023, the natural geomagnetic background shifted in color on the greenish azimuth, and around 07:05 UTC the earthquake occurred. This earthquake remained within the temporal range in which the azimuth variation indicated the color green, relative to the Lariano RM station.

Regarding the activity of space weather, namely the space phenomena generated by solar activity present during the period in which this earthquake occurred, it can certainly be considered that the Earth had just entered a stream of solar wind faster than usual, as visible in Fig. 13.

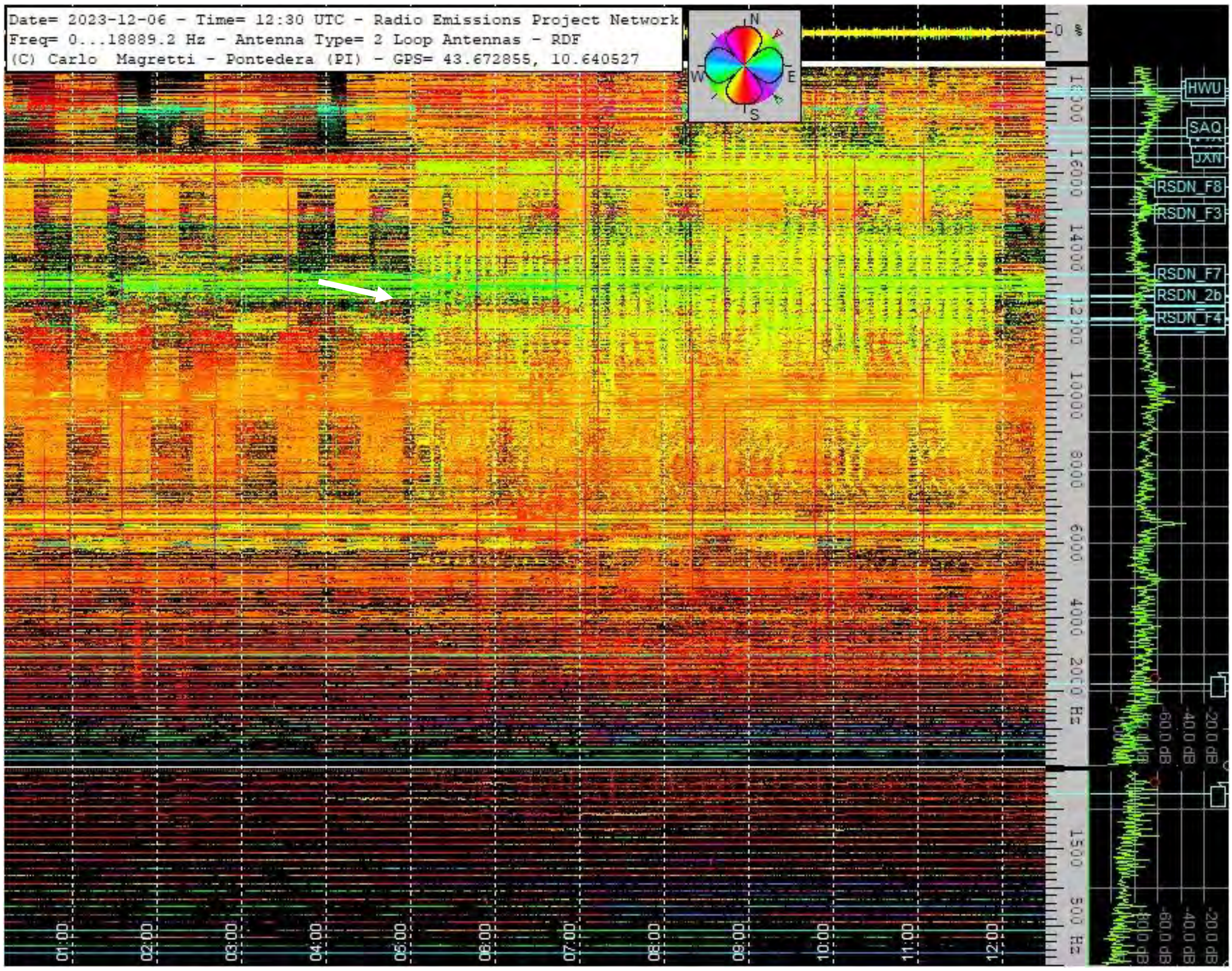

Date= 2023-12-06 - Time= 12:30 UTC - Radio Emissions Project Network
Freq= 0...18889.2 Hz - Antenna Type= 2 Loop Antennas - RDF
(C) Carlo Magretti - Pontedera (PI) - GPS= 43.672855, 10.640527

Fig. 4 – Dynamic Spectrogram recorded by the Pontedera PI RDF station, managed by Carlo Magretti, which highlights the presence of strong electromagnetic signals on the yellow azimuth, appearing at an average electromagnetic frequency of 13 kHz. Credits: Radio Emissions Project; Carlo Magretti.

The measured solar activity showed clear variations in the period between December 29, 2023, and January 1, 2024. Observing Fig. 14, which displays the WINDMI (Wind Direction and Magnitude Index), a metric used in meteorology to measure space weather activity, there was a noticeable increase in nT (nanoTesla):

GOES (Geostationary Operational Environmental Satellites). The term "Primary X-Ray Flux" in relation to GOES satellites refers to their ability to measure the flux of X-rays emitted by the Sun.

The indices used are:

- WINDMI (Wind Direction and Magnitude Index).
- AL (nT): The AL index (Auroral Electrojet Index Low) measures the electromagnetic activity in the aurora, or the polar regions of the Earth. It is measured in nanotesla (nT) and is an indicator of the intensity of electric currents in the upper atmosphere, particularly those associated with the aurora borealis.
- Dst (nT): The Dst index (Disturbance Storm Time) is another geomagnetic indicator, also measured in nanotesla (nT). It reflects global variations in the Earth's geomagnetic field caused by the interaction between the solar wind and the Earth's magnetosphere.

It is evident how solar activity had led to a geomagnetic increase on our Planet several days before the Japanese earthquake. Geomagnetic and solar activities have been at the center of numerous scientific studies for years, demonstrating a direct correlation with terrestrial seismic activity. [18] [19] [20] [21] Another important data related to space weather comes from GOES data (Primary X-Ray Flux). The GOES satellites (Geostationary Operational Environmental Satellites) measure the Primary X-Ray Flux emitted by the Sun.

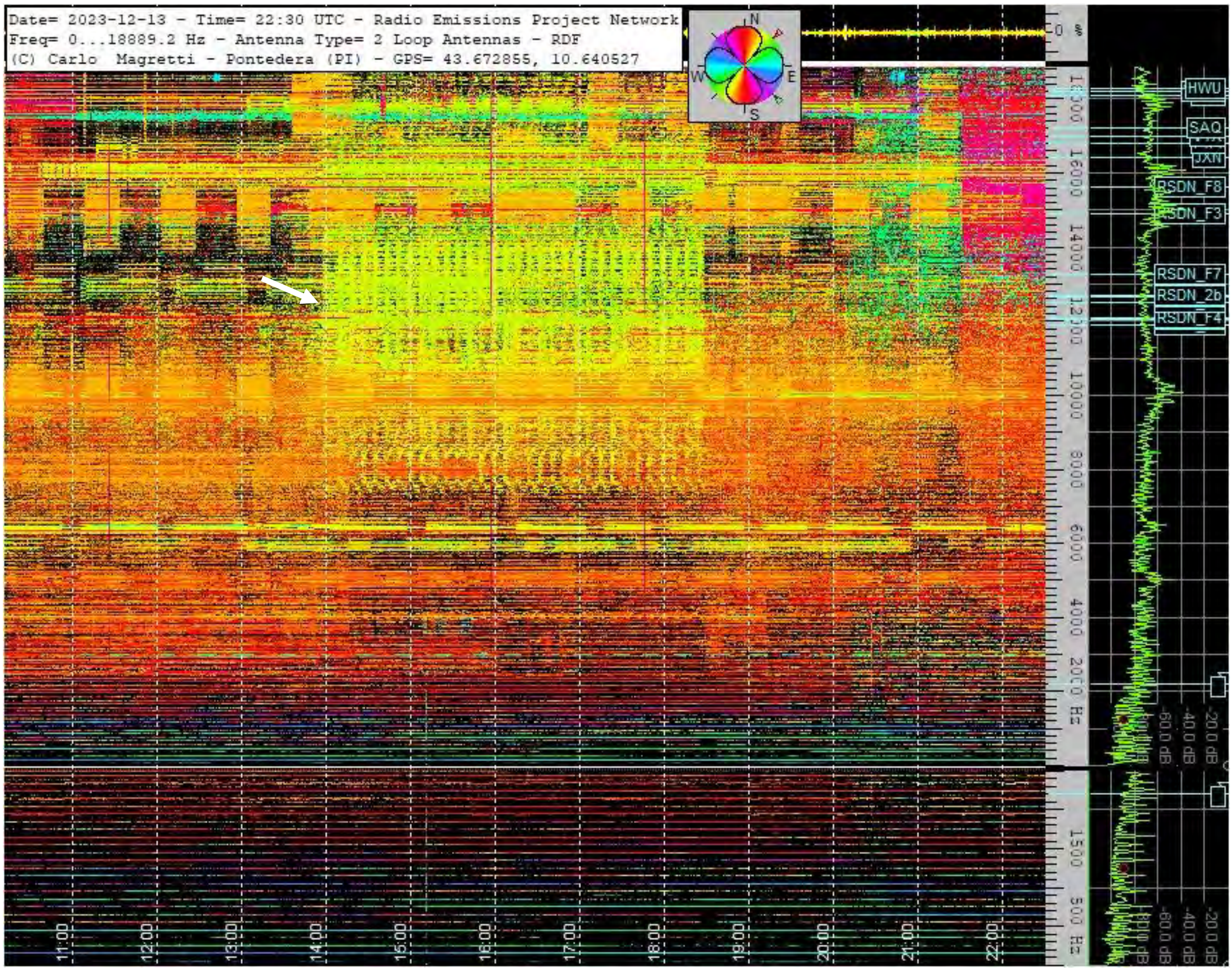

Fig. 5 – Dynamic Spectrogram recorded by the Pontedera PI RDF station, managed by Carlo Magretti, which highlights the presence of strong electromagnetic signals on the yellow azimuth, appearing at an average electromagnetic frequency of 13 kHz. Credits: Radio Emissions Project; Carlo Magretti.

X-rays from the Sun are an important indicator of solar activity, particularly of solar flares and other energetic events that occur on the Sun's surface. Fig. 15 clearly shows the significant connection between the activity of the Sun and the Japanese earthquake, which followed an intense increase in 'X' emissions starting from December 31, 2023, at 11:40 UTC.

On this date, the preparatory phase of the earthquake was still underway. Another notable data point is the speed of the solar wind, recorded by the ACE satellite. The ACE satellite (Advanced Composition Explorer), launched in 1997, is primarily focused on the study of space weather and energetic particles coming from the Sun and interplanetary space.

The recording from the ACE satellite highlights a sudden increase in the speed of the solar wind, just a few hours before the earthquake (Fig. 16).

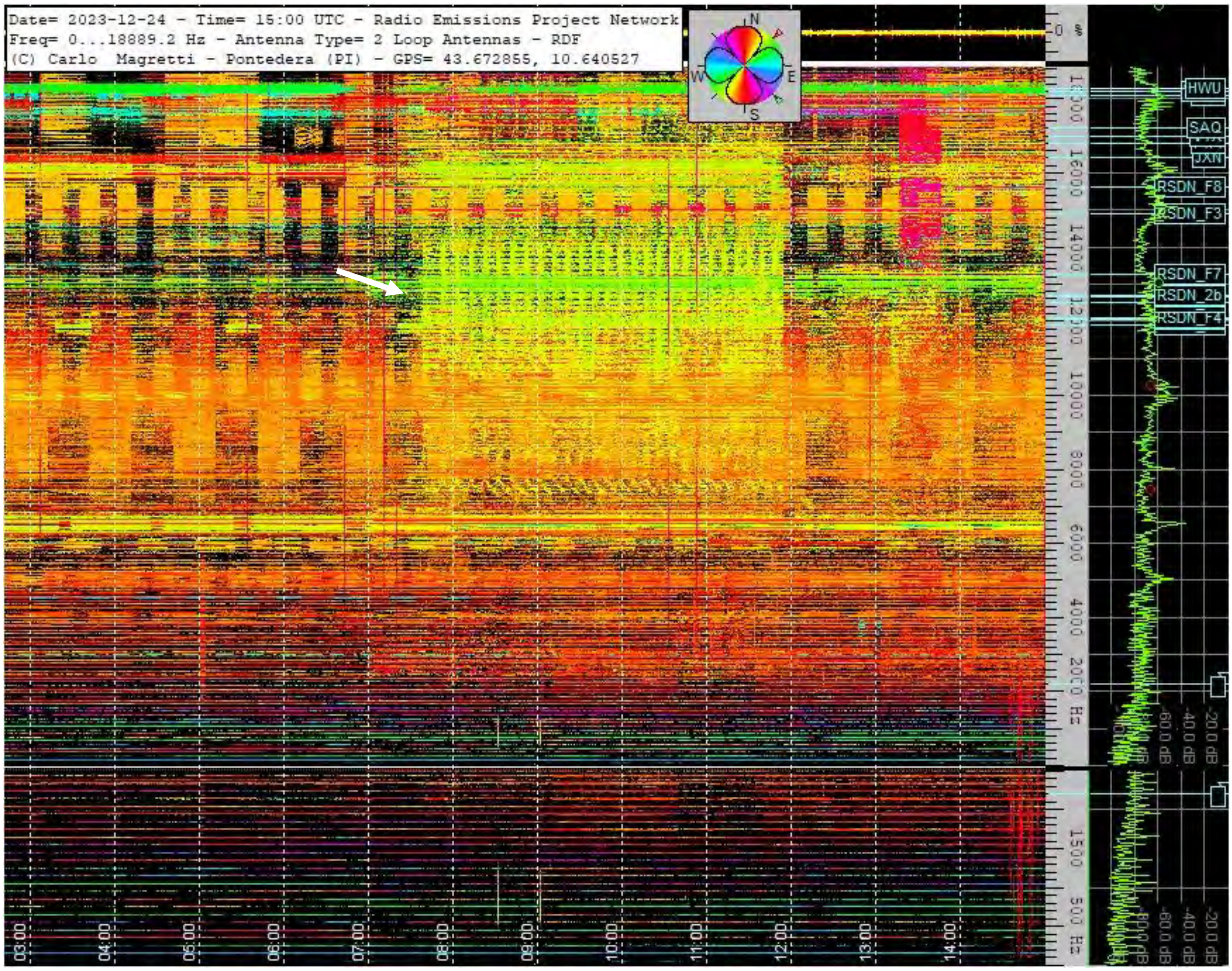

Fig. 6 – Dynamic Spectrogram recorded by the Pontedera PI RDF station, managed by Carlo Magretti, which highlights the presence of strong electromagnetic signals on the yellow azimuth, appearing at an average electromagnetic frequency of 13 kHz. Credits: Radio Emissions Project; Carlo Magretti.

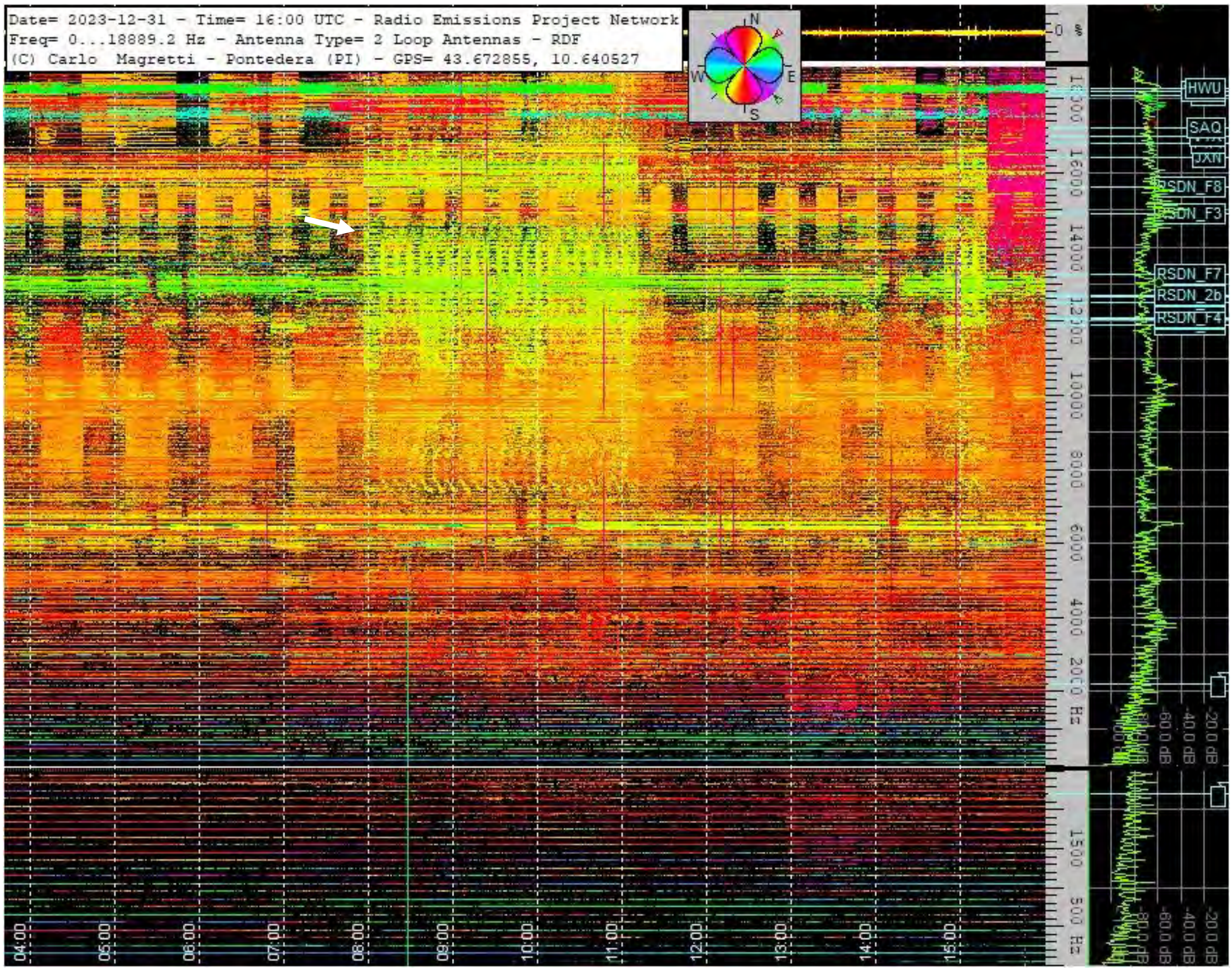

Fig. 7 – Dynamic Spectrogram recorded by the Pontedera PI RDF station, managed by Carlo Magretti, which highlights the presence of strong electromagnetic signals on the yellow azimuth, appearing at an average electromagnetic frequency of 13 kHz. Credits: Radio Emissions Project; Carlo Magretti.

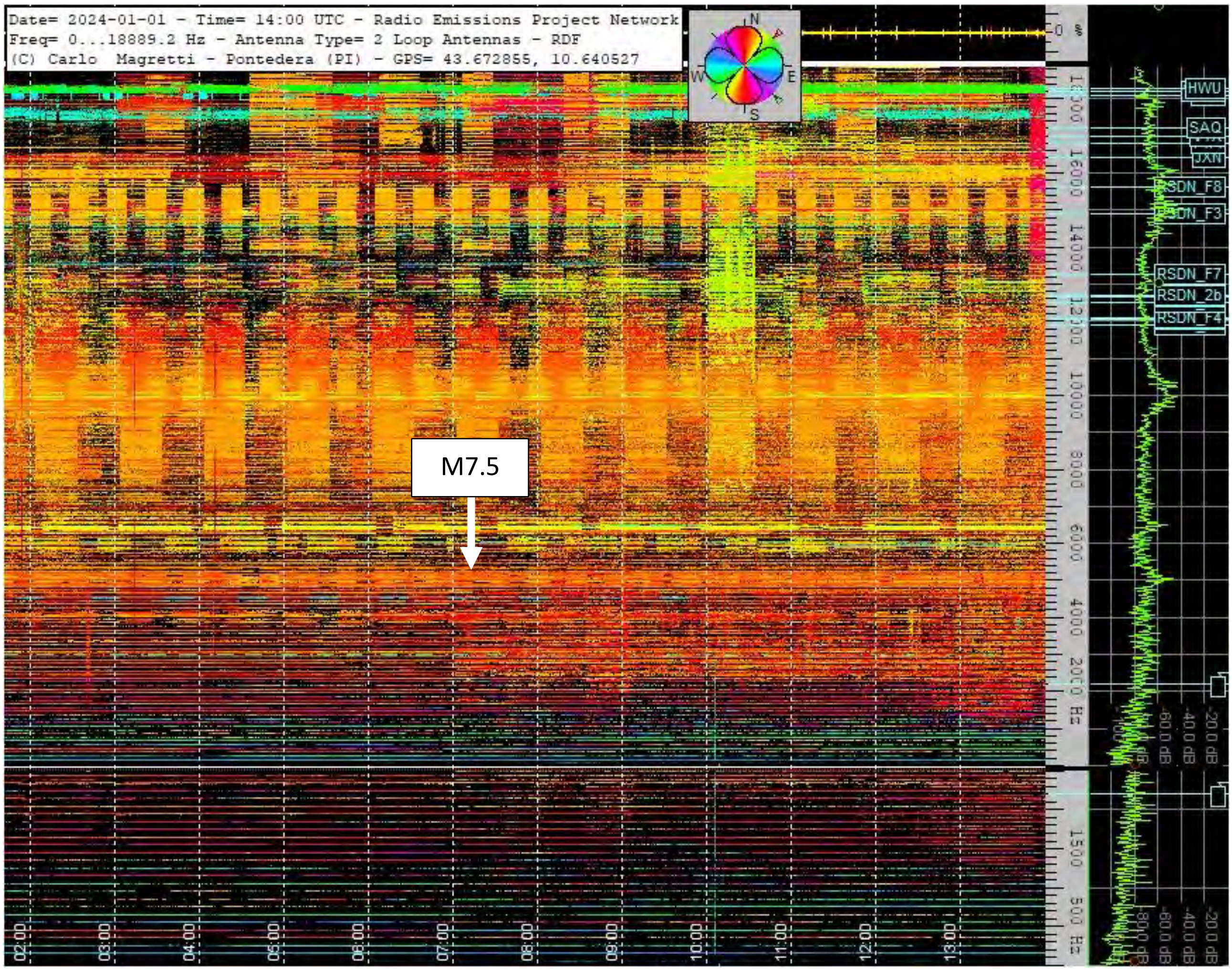

Fig. 8 – Dynamic Spectrogram recorded by the Pontedera PI RDF station, managed by Carlo Magretti, which highlights the presence of strong electromagnetic signals on the yellow azimuth, appearing at an average electromagnetic frequency of 13 kHz, as well as the temporal position of the earthquake. Credits: Radio Emissions Project; Carlo Magretti.

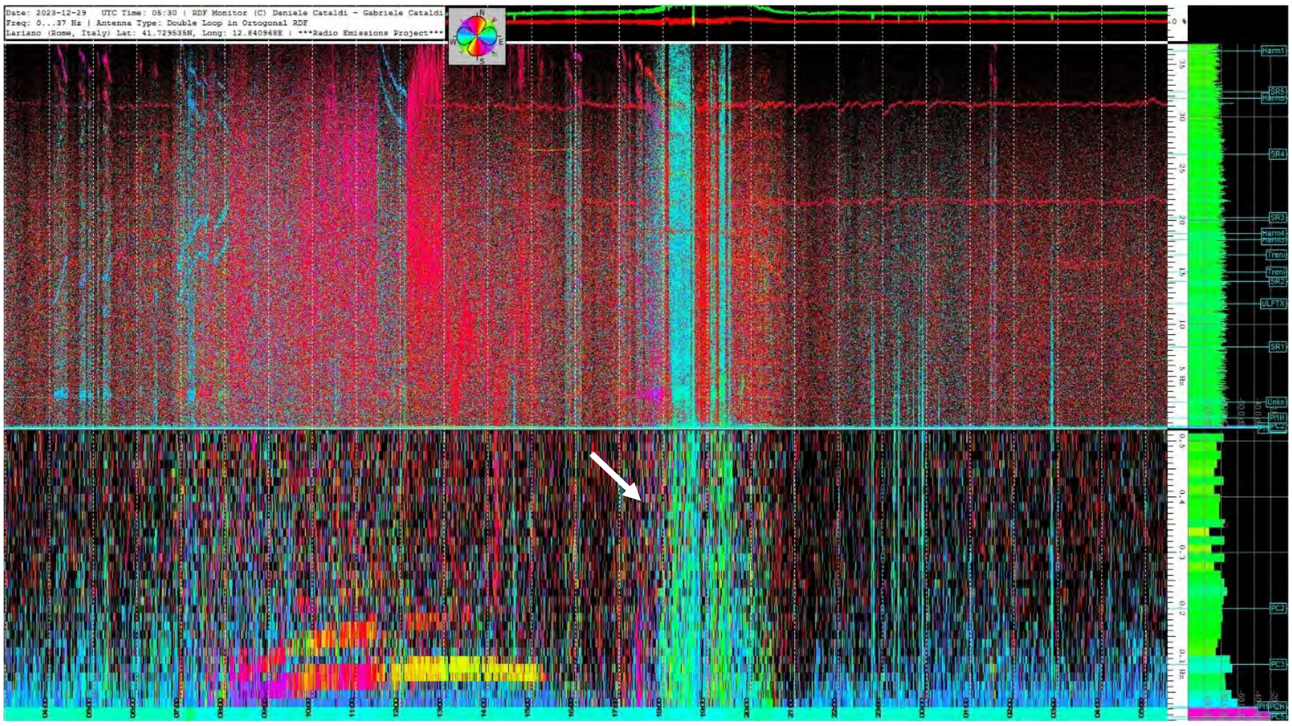

Fig. 9 – Dynamic Spectrogram recorded by the Lariano RM RDF station, showing the electromagnetic emission with a green azimuth. Credits: Radio Emissions Project, Daniele Cataldi.

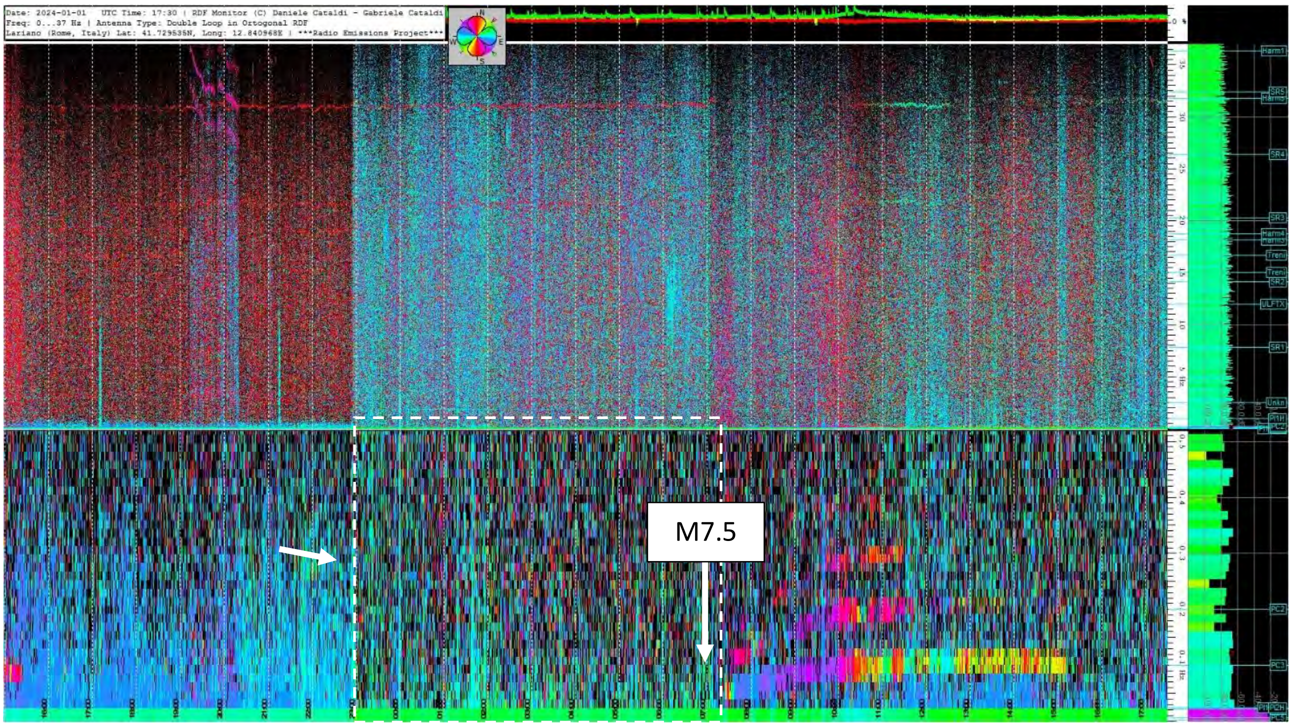

Fig. 10 – Dynamic Spectrogram recorded by the Lariano RM RDF station, showing the electromagnetic emission with a green azimuth and the presence of the earthquake's time. Credits: Radio Emissions Project, Daniele Cataldi.

3 - Temporal Scanning of Signals

The initial electromagnetic recordings made by the Italian RDF network, related to the precursor signals of the Japanese earthquake, were registered starting from November 1, 2023, around 11:00 UTC (Fig. 2) by the Pontedera PI RDF station. These signals appeared suddenly for the first time in a period when there had been no evidence of such radio emissions. They were extremely evident compared to the normal natural electromagnetic background, lasting about 2.4 hours.

The emissions reappeared around 17:30 UTC on November 1, 2023 (Fig. 3), this time lasting approximately 3.3 hours. The electromagnetic signals continued to appear for days and weeks until December 6, 2023 (Fig. 4), when an extensive electromagnetic emission was observed, also emanating from the yellow azimuth relative to the Pontedera PI station, starting at 06:00 UTC until about 12:00 UTC, lasting a full 6 uninterrupted hours. This signal was again centered around 13 kHz. From this date, electromagnetic signals with the yellow azimuth became increasingly frequent. On December 14, 2023 (Fig. 5), the signals remained extremely interesting, with a signal appearing on the yellow azimuth from the Pontedera PI station at 14:00 UTC, 18:35 UTC, lasting 4.5 continuous hours. This signal was preceded and followed by other intense electromagnetic emissions with different azimuths. The signals continued for several more days, indicating an ongoing accumulation of crustal energy in an area located on the yellow azimuth. Ten days later, precisely on December 24, 2023 (Fig. 6), a new extensive electromagnetic emission was recorded, lasting 4.1 hours, starting at 07:40 UTC, ending around 12:00 UTC.

On December 31, 2023 (Fig. 7), the electromagnetic signals recorded by the Pontedera PI RDF station reappeared at 08:00 UTC, ending around 11:10 UTC, with a total duration of the emissions of 3.1 hours. In this case, too, this radio signal was important in a predictive context, preceded by other electromagnetic appearances at the same frequency (13 kHz).

On January 1, 2024 (Fig. 8) at 07:10:09 (UTC), a strong earthquake hit Japan, with a magnitude of Mw 7.5, very intense, causing deaths and the collapse of some homes. This event caused significant problems to Japanese infrastructure.

In the recorded spectrogram, a faint reddish emission is visible at the moment the strong earthquake occurred, but there were no other electromagnetic emissions indicating the yellow azimuth.

Only subsequently (a few hours later) were there other electromagnetic signals with the same azimuth, probably produced by the Earth's crust near the seismic hypocenter, under significant energetic increase (tectonic stress).

The Lariano RM RDF station also recorded an intense emission, not preceded and not followed by other similar emissions detected previously (Fig. 9).

On December 29, 2023 (Fig. 9), the Lariano RM RDF station highlighted the presence of a strong electromagnetic emission, appearing around 18:00 UTC and lasting until about 20:35 UTC, with an electromagnetic frequency ranging from 0.0 Hz to 1 Hz, and repeated resonance harmonics up to 4 Hz.

On January 1, 2024 (Fig. 10), the Lariano RM RDF station again showed the appearance of electromagnetic signals on the green azimuth, this time, as visible in Fig. 10, around 23:00 UTC on December 31, 2023, the natural geomagnetic background shifted in color on the greenish azimuth, and around 07:05 UTC the earthquake occurred, which remained within the temporal range where the azimuth variation indicated the color green, relative to the Lariano RM station.

Regarding the activity of space weather, namely the space phenomena generated by solar activity present during the period in which this earthquake occurred, it can certainly be considered that the Earth had just entered a stream of solar wind faster than usual, as visible in Fig. 13.

The measured solar activity showed clear variations in the period between December 29, 2023, and January 1, 2024. Observing Fig. 14, which displays the WINDMI (Wind Direction and Magnitude Index), a metric used in meteorology to measure space weather activity, there was a noticeable increase in nT (nanoTesla).

It is evident how solar activity had led to a geomagnetic increase on our Planet several days before the Japanese earthquake. Geomagnetic and solar activities have been at the center of numerous scientific studies for years, demonstrating a direct correlation with terrestrial seismic activity. [18] [19] [20] [21]

Solar X-rays are an important indicator of solar activity, particularly of solar flares and other energetic events that occur on the Sun's surface. Fig. 15 clearly shows the significant connection between the activity of the Sun and the Japanese earthquake, which followed an intense increase in 'X' emissions starting from December 31, 2023, at 11:40 UTC.

On this date, the preparatory phase of the earthquake was still underway. Another notable data point is the speed of the solar wind, recorded by the ACE satellite. The ACE satellite (Advanced Composition Explorer), launched in 1997, is primarily focused on the study of space weather and energetic particles coming from the Sun and interplanetary space.

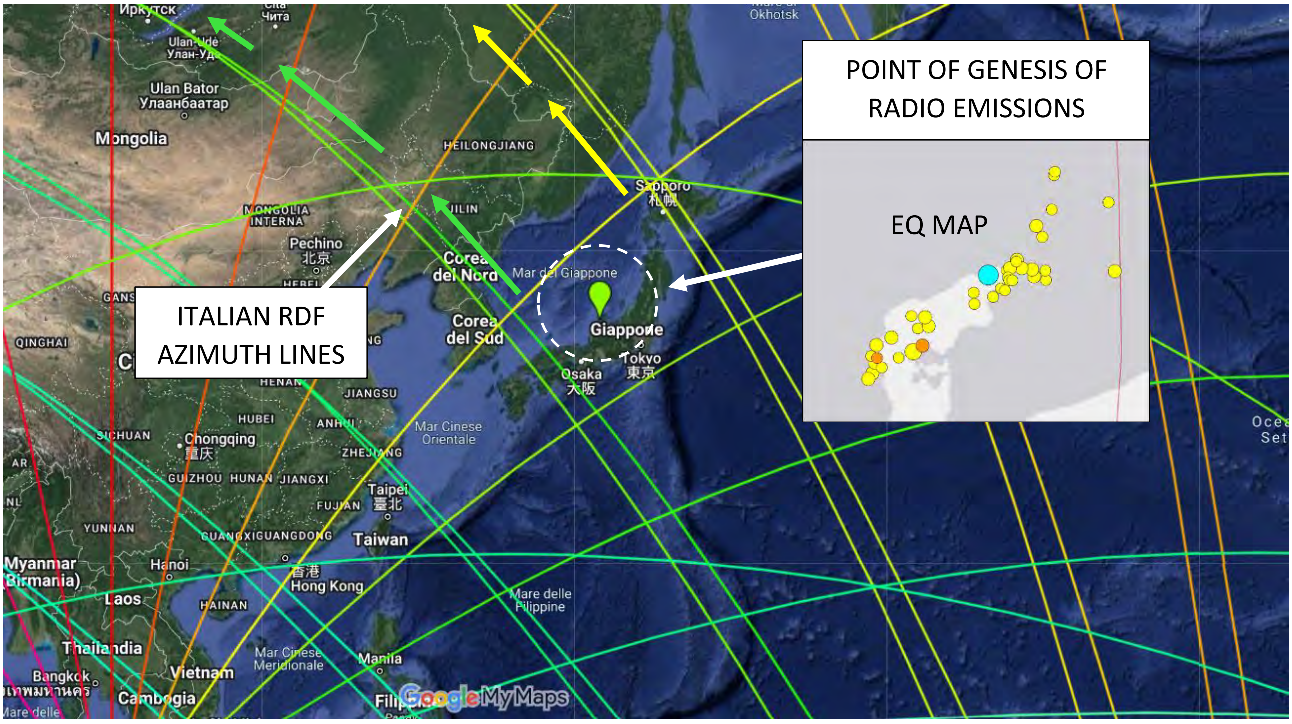

Fig. 11 – Colorimetric map developed by the Radio Emissions Project, highlighting the geographical area of the earthquake (Japan) and its epicenter. The colored lines represent the azimuths relative to the various RDF stations located globally, including those in Italy. It is evident how the signals (azimuths) green and yellow delineate the geographical area of Japan, where the earthquake subsequently occurred. Credits: Daniele Cataldi; Radio Emissions Project; USGS.

The recording from the ACE satellite highlights a sudden increase in the speed of the solar wind, just a few hours before the earthquake (Fig. 16).

Electromagnetic recordings show that there were electromagnetic emissions coming from the area of the strong Japanese earthquake, weeks and days before it occurred.

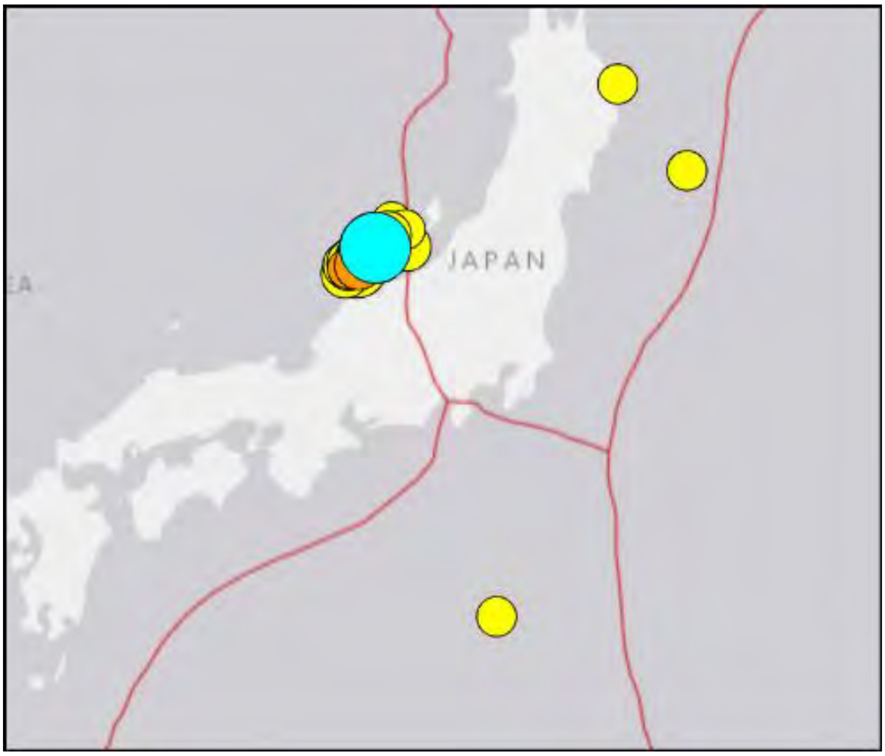

Fig. 12 – Mapping of the earthquakes that occurred in Japan with the Main Shock of Mw7.5 and subsequent seismic events that characterized the Japanese area from January 1, 2024, to January 6, 2024 (M4.5+). Credits: USGS

The RDF network map (Fig. 11) shows the Japanese zone with the respective azimuths of signal origin, delimited by the yellow and green azimuths, the same colors that the RDF system highlighted in relation to the appeared signals, indicating, without a doubt, the Japanese area.

It is evident that the area within which the Japanese earthquake occurred emitted electromagnetic emissions detectable from a distance, in this case around 9,500 km.

An emission of this kind must have had a power of thousands of Watts to reach Italy and be detected, justifying the fact that such electromagnetic signals were emitted by an extremely extensive and wide fault, where a lot of energy accumulates (tectonic stress). Indeed, if we observe the Japanese area, it shows numerous subsequent earthquakes to the main shock of magnitude Mw7.5 that occurred between January 1, 2024, and January 6, 2024 (M4.5+), as visible in Fig. 12.

Japan is located in a highly seismic region, where several tectonic plates meet, including the Pacific Plate, the Philippine Plate, the North American Plate, and the Eurasian Plate. This positioning leads to high seismic and volcanic activity. The faults in Japan are numerous and complex, with some of the most notable including the Nankai Fault and the Sagami Fault. These faults have the capability to generate very powerful and destructive earthquakes.

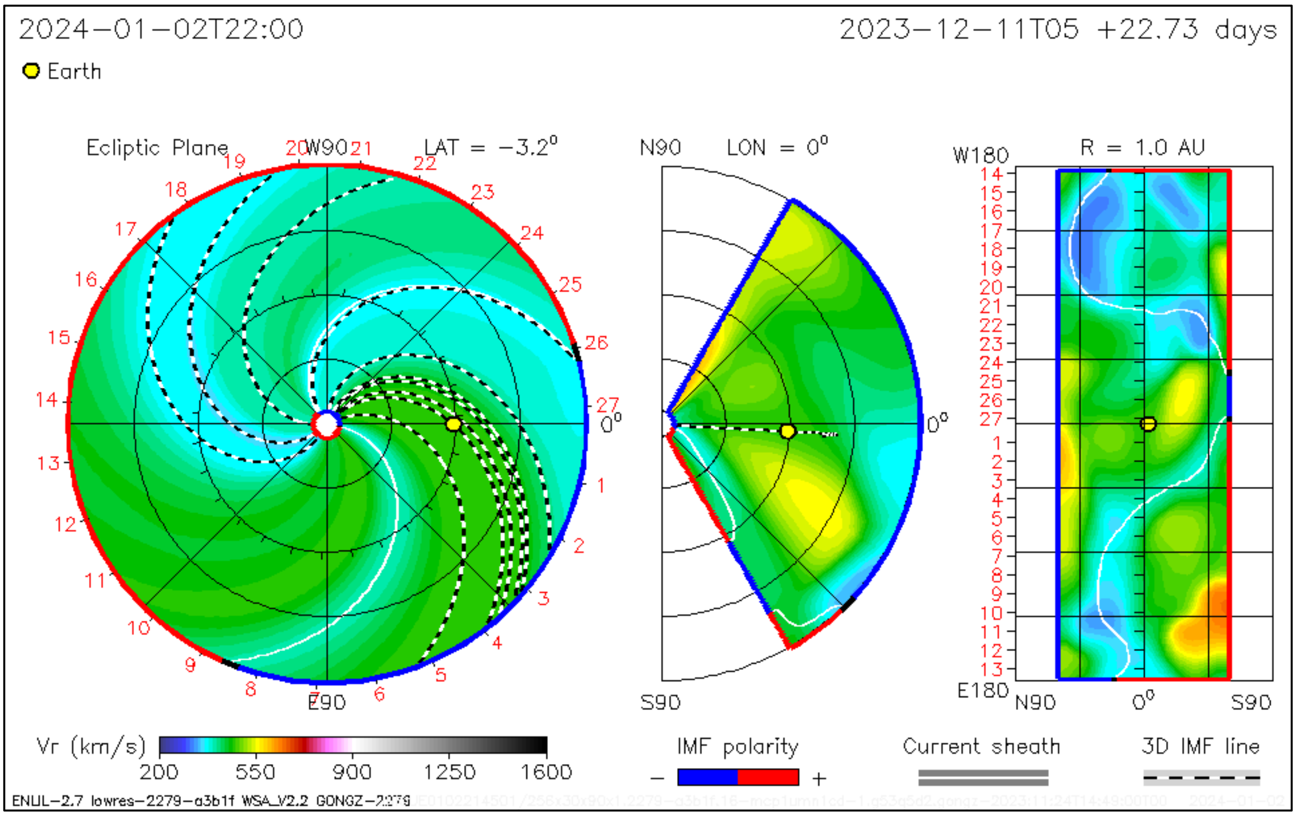

Fig. 13 – Solar Wind Speed measured at Earth's orbit. It is evident that around January 1, 2024, the Earth had entered a stream of solar wind with a higher velocity. Credits: iSWA.

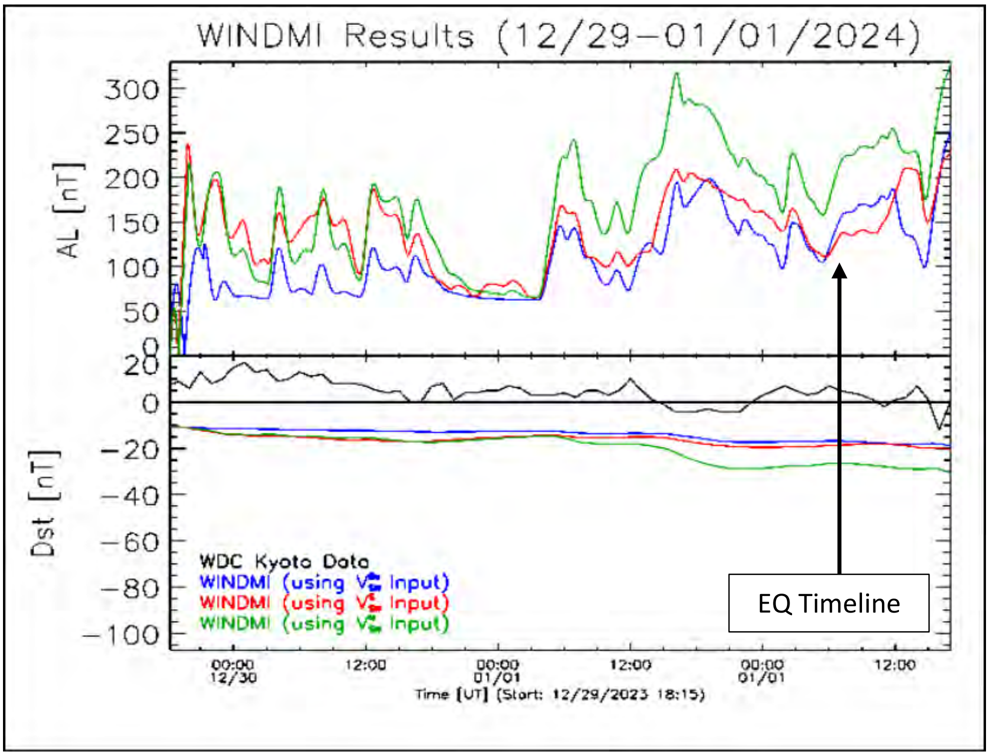

Fig. 14 – The WINDMI chart shows the presence of interesting geomagnetic variations in the period from December 29, 2023, to January 1, 2024. Credits: iSWA.

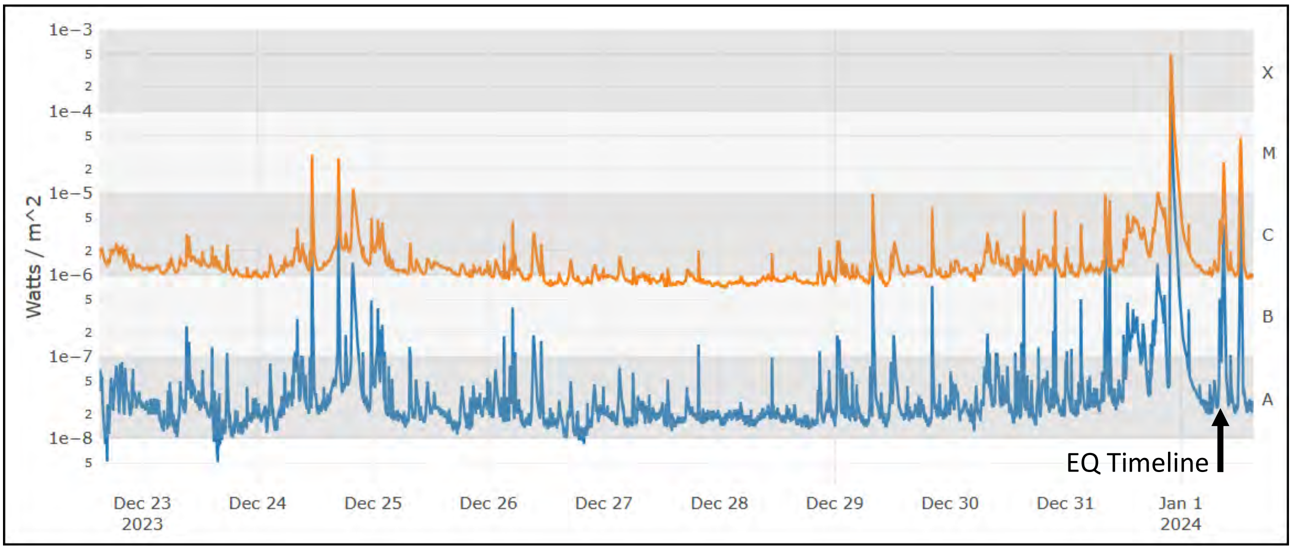

Fig. 15 – Chart showing the solar 'X' radiation (X-Rays) recorded by GOES satellites, 10 days prior to the earthquake that occurred in Japan, highlighting the Time-Line of the earthquake that followed a series of increases. Credis: iSWA.

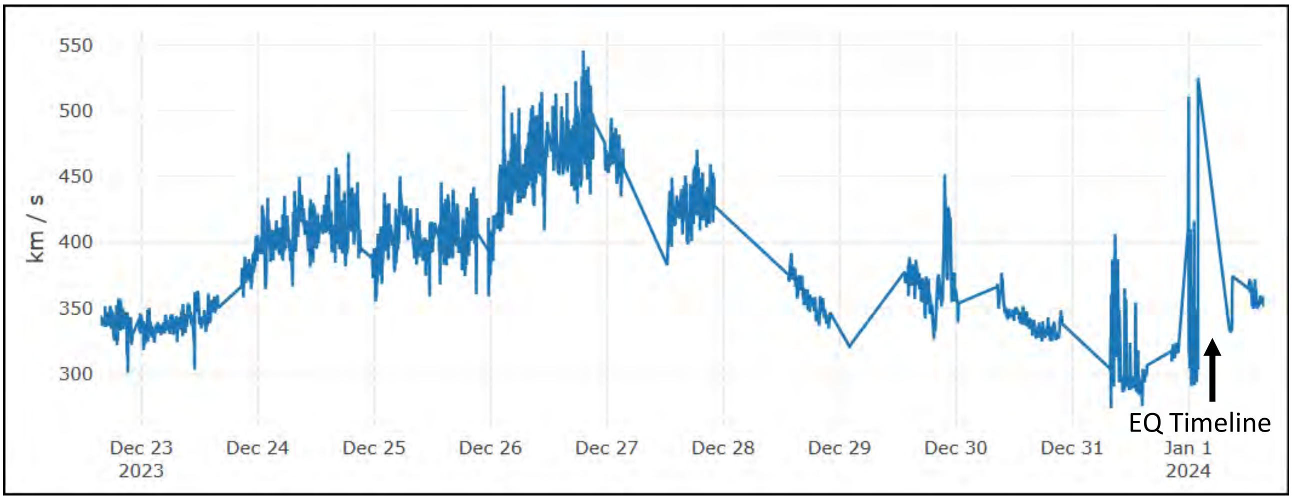

Fig. 16 – Chart of the solar wind speed, recorded by the ACE satellite, showing an intense increase in speed just a few hours before the Japanese earthquake. Credits: iSWA.

4 - Conclusion

This study has gathered enough information to conclude that the Japanese earthquake, which occurred on January 1, 2024, with a magnitude of Mw7.5, was preceded by electromagnetic signals generated many days before the violent earthquake.

In this phase, energy accumulates before being released, mechanical stress produces high pressure on rocks which, due to the pressure, produce free ions (moving electrical charges) [13], resulting in the phenomenon of piezoelectricity, through which they can emit radiofrequency [11][12][14], especially over a very extensive fault surface, like the Japanese one.

Such signals emitted from the 'local' lithosphere can be received and recorded by one or more radio receiving stations at a distance. Multiple radio stations can also triangulate the signal, understanding the exact position where such a natural emitter is located.

The two Italian RDF stations (separated by a distance of 300 km) provided data on the angle of arrival of the radio signals (Angular or Directional Triangulation), relative to their GPS position, and therefore it was possible to understand where such signals were coming from.

In this case, the signals preceded the strong and destructive earthquake by 61 days.

Another important data emerged from this study is that of solar activity, which is directly correlatable to the preparatory phase of the earthquake in question:

- Increase in the speed of the solar wind a few hours before the earthquake occurred.
- Increase in Earth's geomagnetic activity, beginning several days before the earthquake.
- Increase in X-ray activity from the Sun several hours before the earthquake occurred.

In light of these results, it is evident that solar activity seems to be again associated with terrestrial seismic activity and in this case with the strong Japanese earthquake.

References

[1] G. Cataldi, D. Cataldi. (2013). Reception of Natural Radio Emissions in the ELF Band. The INSPIRE Journal, Volume 20, Spring/Summer 2013. pp12-16.

[2] G. Cataldi, D. Cataldi, V. Straser. (2014). Solar wind proton density variations that preceded the M6+ earthquakes occurring on a global scale between 17 and 20 April 2014. European Geosciences Union (EGU) General Assembly 2015, Natural Hazard Section (NH5.1), Sea & Ocean Hazard - Tsunami, Geophysical Research Abstract, Vol. 17, Vienna, Austria. Harvard-Smithsonian Center for Astrophysics, High Energy Astrophysics Division, SAO/NASA Astrophysics Data System.

[3] G. Cataldi, D. Cataldi, V. Straser. (2015). Solar wind proton density variations that preceded the M6,1 earthquake occurred in New Caledonia on November 10, 2014. European Geosciences Union (EGU) General Assembly 2015, Natural Hazard Section (NH5.1), Sea & Ocean Hazard - Tsunami, Geophysical Research Abstract, Vol. 17, Vienna, Austria. Harvard-Smithsonian Center for Astrophysics, High Energy Astrophysics Division, SAO/NASA Astrophysics Data System.

[4] G. Cataldi, D.Cataldi, V. Straser. (2015). Solar wind ion density variations that preceded the M6+ earthquakes occurring on a global scale between 3 and 15 September 2013. European Geosciences Union (EGU) General Assembly 2015, Natural Hazard Section (NH5.1), Sea & Ocean Hazard - Tsunami, Geophysical Research Abstract, Vol. 17, Vienna, Austria. Harvard-Smithsonian Center for Astrophysics, High Energy Astrophysics Division, SAO/NASA Astrophysics Data System.

[5] G. Cataldi, V. Straser. (2015). Solar wind ionic variation associated with earthquakes greater than magnitude 6,0. New Concept in Global Tectonics Journal, V. 3, No. 2, June 2015.

[6] V. Straser, G. Cataldi, D. Cataldi. (2015). Solar wind ionic and geomagnetic variations preceding the Md8.3 Chile earthquake. New Concept in Global Tectonics Journal, V. 3, No 3, September 2015.

[7] V. Straser, D. Cataldi, G. Cataldi. Radio Direction Finding System, a new perspective for global crust diagnosis - New Concepts in Global Tectonics Journal, v. 6, no. 2, June 2017.

[8] D. Cataldi, G. Cataldi, V. Straser. Radio Direction Finding (RDF) - Pre-seismic signals recorded before the earthquake in central Italy on 1/1/2019 west of Collelongo (AQ) - Geophysical Research Abstracts Vol. 21, EGU2019-3124, 2019 EGU General Assembly 2019.

[9] V. Straser, D. Cataldi, G. Cataldi. Radio Direction Finding (RDF) - Geomagnetic Monitoring Study of the Himalaya Area in Search of Pre-Seismic Electromagnetic Signals - Asian Review of Environmental and Earth Sciences - Vol. 6, No. 1, 16-27, 2019 - ISSN(E) 2313-8173/ ISSN(P) 2518-0134 - DOI: 10.20448/journal.506.2019.61.16.27 - © 2019 by the authors; licensee Asian Online Journal Publishing Group.

[10] V. Straser, D. Cataldi, G. Cataldi. Registration of Pre-Seismic Signals Related to the Mediterranean Area with the RDF System Developed by the Radio Emissions Project –International Journal of Engineering Science Invention (IJESI) - ISSN (Online): 2319 – 6734, ISSN (Print): 2319 – 6726 - www.ijesi.org ||Volume 8 Issue 03 Series. II || March 2019 || PP 26-35.

[11] M. Caperton Morton. Ionospheric charge could forewarn of earthquakes - American Geosciences Institute. 2014 - Earth - The Cience Behind the Headlines. https://www.earthmagazine.org/article/ionospheric-charge-could-forewarn-earthquakes.

[12] D.-S. Park, M. Hadad, L. M. Riemer, R. Ignatans, D. Spirito, V. Esposito, V. Tileli, N. Gauquelin, D. Chezganov, D. Jannis, J. Verbeeck, S. Gorfman, N. Pryds, P. Muralt, D. Damjanovic. Induced giant piezoelectricity in centrosymmetric oxides. Science, 2022; 375 (6581): 653 DOI: 10.1126/science.abm7497.

[13] Friedemann T. Freund. Rocks That Crackle and Sparkle and Glow: Strange Pre-Earthquake Phenomena - Department of Physics, San Jose State University, NASA Ames Research Center, Moffett Field, CA 94035-1000 Journal of Scientic Exploration, Vol. 17, No. 1, pp. 37–71, 2003 0892-3310/03.

[14] M. Parrot. Electromagnetic Disturbances Associated With Earthquakes: An Analysis of Ground-Based and Satellite Data - Laboratoire de Physique et Chimie de I'Environnement, 45071 Orleans Cedex 02, France. Journal of Scientific Exploration. Vol. 4, No. 2, pp. 203-2 1 1, 1990 - 0892-3310190 - Pergamon Press pic. Printed in the USA - 01991 Society for Scientific Exploration.

[15] G. Cataldi, D. Cataldi, V. Straser. Space weather and geomagnetic activity related to M6+ earthquakes recorded between 7 and 20 November 2017 - Page 137 New Concepts in Global Tectonics Journal Volume 9, Number 3, September 2021.

[16] G. Cataldi, D. Cataldi, V. Straser. Space weather and geomagnetic activity related to M6+ earthquakes recorded between 12 and 15 April 2012 - Page 145 New Concepts in Global Tectonics Journal Volume 9, Number 3, September 2021.

[17] G. Cataldi, D. Cataldi, V. Straser. Space weather and geomagnetic activity related to M6+ earthquakes recorded between 13 and 16 April, 2016 - Page 158 New Concepts in Global Tectonics Journal Volume 9, Number 3, September 2021.

[18] G. Cataldi, D. Cataldi, V. Straser. Space weather and geomagnetic activity related to M6+ earthquakes recorded between 17 and 19 July 2017 - Page 164 New Concepts in Global Tectonics Journal Volume 9, Number 3, September 2021.

[19] G. Cataldi, V. Straser, D. Cataldi - Space weather related to M6.0 Tonga earthquake recorded on March 17, 2020 - New Concepts in Global Tectonics Journal Volume 9, No 4, December 2021 - Pag 206-214.

[20] V. Straser, G. Cataldi, D. Cataldi - Space weather related to M6+ potentially desctructive seismic events recorded on a global scalebetween 13 and 16 March 2022 - New Concepts in Global Tectonics Journal - Volume 10, Number 1, March 2022. pp 3-10.

[21] V. Straser, G. Cataldi, D. Cataldi - Space weather related to M6+ potentially destructive seismic events recorded on a global scale between 2012 and 2021 - New Concepts in Global Tectonics Journal - Volume 10, Number 1, March 2022. pp 11-21.

Correlation Study: Triggering and Magnitude of Earthquakes in Italy (=M4.3) in Relation to the Positions and Gravitational Forces of the Sun, Moon, and Planets Relative to Earth

Stefano Calandra: CEO, EqForecast, an innovative start-up in the field
of seismic forecasting, Venice, Italy;info@earthquakesforecast.com

Daniele Teti: Physicist, Senior IT, and Researcher, EqForecast,
L'Aquila, Italy;info@earthquakesforecast.com

Corresponding author: Stefano Calandra

Editor's note: Highlighted text identifies various data links

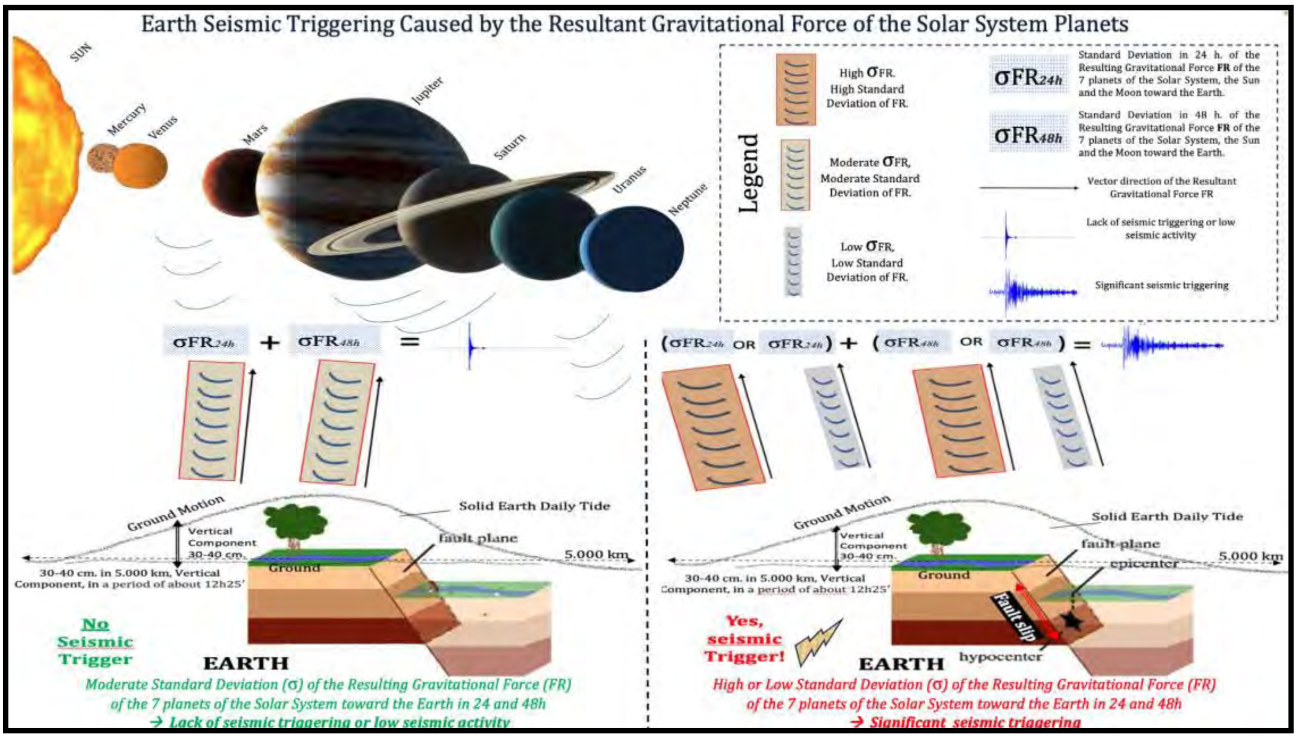

Abstract

When earthquakes occur, researchers explore potential correlations between specific gravitational forces and the positions of Solar System planets related to seismic activity. Studies from various times and places have investigated these correlations, including the effects of Solar and Lunar tides, occasionally yielding controversial results. Recent research underscores how Lunar-Solar tides affect the Earth's crust, creating multidimensional oscillations, establishing a link with seismic activity. This study, based on a sample of 200 Italian earthquakes M>4.3 from 1600 to 2022, reveals statistical correlations between the positions of celestial bodies in the Solar System and earthquake magnitudes at the time of earthquake triggering (Hypothesis 1). Additionally, a recurring pattern emerges in the gravitational forces exerted by these celestial bodies during earthquake triggers (Hypothesis 2). These findings suggest that the Lunar-Solar system is not the sole external gravitational factor influencing earthquakes: instead, the "7 Planet System" shows a more significant causal relationship in this context. We utilize an indirect calculation method that involves vector physics and considers the angles formed between pairs of planets and the Earth. The utilization of this data has the potential to contribute to a plausible predictive earthquake model.

Keywords: Earthquake forecasting and prediction; planetary masses; celestial bodies; non-random statistical correlation; gravitational forces; seismic triggers; vertical tidal forces; astro-seismology; early warning systems

1 Introduction

1.1 . A new approach

In this preliminary study, we propose a new approach to investigating the relationship between celestial bodies and earthquakes. We focus on two key aspects: whether the masses of seven Solar System planets, the Moon, and the Sun influence earthquake triggering and magnitude. This study extends the methodology of prior earthquake prediction research, which focused on planetary positions and masses to elucidate earthquake causation (see *infra*, Section 1.3). Nevertheless, these earlier studies did not compute gravitational forces during seismic events to establish direct correlations.

In general, the term *"earthquake prediction"* has been used cautiously and mainly associated with basic research, rather than applied fields. There is only one case [1] in China, where the official support of earthquake prediction research is mentioned, with China intending to study correlations between celestial body positions in the Solar System and earthquakes during the late 1960s and 1970s.

1.2. Non-planetary precursors of strong earthquakes

Researchers have explored *various non-planetary precursors of strong earthquakes*, including electromagnetic fields [2] [3] sonic and neutron emissions [4] solar activity [5], [6] and more recently, an Italian study [7], geographical and abnormal oscillations in latitude and longitude values of precursor earthquakes [8], radon [9] [10] and the Global Positioning System GPS [11] [12].

1.3. Planetary action capable of triggering earthquakes

This study analyzes the potential link between celestial bodies and earthquakes, focusing on the planets, the Moon and the Sun and *basically following the first line of research* (see *infra*, section 1.3.1). Historical research also examines correlations between the positions of celestial bodies and earthquakes and the tidal effects of the Sun and Moon. A study in particular of the second line of research (see *infra*, section 1.3.2) will be taken as the basis of this research.

1.3.1. First line of research

The first line of studies, though less prominent, examines the statistical correlation between the positions of the Sun, Moon phases, planets of the Solar System, and earthquakes. It discusses this connection in relation to directly measuring planet positions. One reason for its relatively lesser attention, particularly among Western researchers, is the scarcity of measurement instruments in the field (see *supra*, Section 1.2).

Dating back to Plinius Secundus (Italy, 23-79 A.D.), the oldest citation in this context associates earthquakes with alignments and quadratures of the Sun with Mars, Jupiter, and Saturn. Plinius states: *"Babyloniorum placita et motus terrae hiatusque, qua cetera omnia, siderum vi existimant* *fieri, sed illorum trium, quibus fulmina adsignant, fieri autem meantium cum sole aut congruentium et maxime circa quadrata mundi"*. "The Babylonian scientific traditions maintain that even the motions and fractures of the Earth, like all other things, occur due to the force of the planets, in particular those three, to which they assign lightning, but they occur in particular when they revolve with the Sun or are in conjunction and especially around quadratures (90°)" [13].

More recently, earthquakes show a heightened occurrence during phases such as Full and New Moons [4], [14], [15], [16] and even Last Quarter and New Moons [17]. Recent work [18], directly connects earthquake-triggering to gravitational forces arising from the interactions between planets, the Sun, Moon, and Earth's tectonic plates.

An emerging trend in India also examines the Sun, Moon, and planets in relation to Earth. This involves categorizing planets into groups to measure their angles during seismic events [19] or calculating angular vectors of gravitational forces from planetary masses to identify earthquake triggers [20].

1.3.2. Second line of study and its significance

Research from the late 1800s explores [21], [22], whether solid tidal forces from the Sun and Moon trigger earthquakes. Correlations between tidal action and earthquakes are supported by evidence and are well-accepted. Recent findings [23], [24] highlight the impact of tides on the solid Earth and crust, or causing multidimensional oscillations during lunar and solar passages [25], [26], [22], [23], [24], [27]. These deformations, combined with plate motion and Earth tide components, link tides to seismic activity.

2. Materials and methods

This study examines 200 earthquakes with a magnitude greater than M4.3 from the ASMI-INGV database [28]. Fifty-five earthquakes were handpicked, while 145 were randomly selected from Italy's 1,590 M4.3+ earthquakes spanning from the 1600s to 2022 (see *infra*, Section 2.10, Table 4).

The Italian study (Zaccagnino et al. 2020) belonging to the second line of research emphasizes the impact of tides on the solid Earth and crust, contributing to seismic activity. Gravitational forces, including the vertical component of tides, can trigger seismicity over time. The vertical component of lunar-solar tides, solid and liquid, can trigger seismicity after decades or centuries, when horizontal energy accumulates.

Following this hypothesis, but due to the lack of instruments on the ground to measure gravitational variations, this study employs indirect computational methods involving vector physics and the angles formed by pairs of planets with Earth (see *infra*, Section 2.8).

Building on the vector approach of the Indian article (Jeganathan, C. et al. 2015) belonging to the first line of research, this study seeks to provide new evidence to support the hypothesis that the forces responsible for triggering earthquakes adhere to Newton's law of universal gravitation.

Historically, links have been established between planetary positions and earthquakes, *but a systematic analysis is missing.* Fortunately, modern computational tools, accessible to individual researchers, have made such studies independent of complex ground surveying technology. State-of-the-art software, relying on Kepler's astronomical laws from 1627, calculates planetary positions, streamlining our calculations. The next section delves into the calculation methods used to input planetary positions related to earthquakes.

2.1. Altazimuth coordinate system

To capture these rapid angular changes of the planets, instead of using one of the other two systems - the equatorial coordinates [20], [22] and the ecliptic coordinates [19] - generally used in the other studies*, we employed altazimuth coordinates*—a reference system tied to the Observer's position shifting with Earth's rotation and Planets' motion. We also extend the use of altazimuth coordinates to showcase the Hypothesis 2 underscoring *the novelty of this astronomical coordinate model in earthquake research.*

This dynamic approach, adjusting with Earth's rotation and planetary movements, enhances sensitivity in calculating planet/earthquake angular correlations. We also extend the use of altazimuth coordinates to showcase the Hypothesis 2 underscoring *the novelty of this astronomical coordinate model in earthquake research.*

2.2. Geographical reference quadrant

A significant challenge was determining how to calculate planetary angles from an Earth observation point. We employed azimuth and elevation coordinates from the Astronomical Tables of VSOP87 [29] to derive the relevant angles for each planet pair. Our Earth observation point aligns with Lat. 42.7°/42.8° and Long. 13.23°, roughly corresponding to Accumoli (RI), Central Italy. The quadrant's bounds are set by the 200 earthquakes analyzed, spanning Lat. 47.18°, Long. 06.80° to Lat. 36.66°, Long. 18.68° including part of the Balkan Peninsula.

2.3. Angular distance of celestial bodies

Accurately determining the angular position of a planet pair relative to Earth involves accounting for *delta elevation* and *delta azimuth*. Representing a three-star system— O =Earth, B=Planet 1, and D=Planet 2—on a Cartesian plane establishes an angular reference system. The angular *value BD serves as the "angular distance",* summarizing the delta between the azimuths and elevations of the 2 planets B and D relative to the Earth observer (figure. 1)

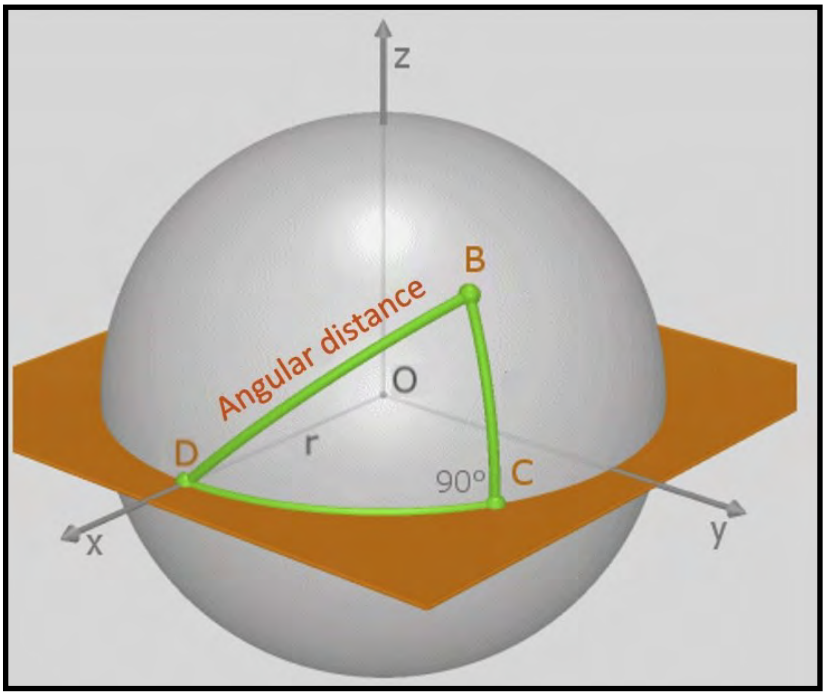

Figure 1. Determination of angular distance in a spherical plane. The angular *value BD serves as the "angular distance",* summarizing the delta between the azimuths DC and the delta between the elevations BC of the 2 planets B and D relative to the Earth O observer. The equation DB^2 = DC^2 + BC^2 applicable to the Cartesian plane is adaptable to spherical planes, which are utilized when calculating sidereal distances. However, points B, C, and D lie *on different spherical planes* due to their construction, necessitating simplification if placed on a single spherical plane. The spherical right triangle Pythagorean Theorem converges to the Cartesian plane's classical Pythagorean Theorem when the sphere's radius r → ∞, we use the Taylor polynomial 1-x2/2. *This allows us to simplify the "angular distance" from the spherical plane to the Cartesian plane for calculations.*

2.4. Spherical and Cartesian planes

Considering distances between point O in space and points B, C, D (i.e., the sphere's radius r - Figure 1), which can be millions of kilometers apart (e.g., Earth-Jupiter distance ≈ 7.858×10^{8} km), we can approximate the equation $\cos(DB/r) = \cos(DC/r)\cos(CB/r)$ as if we were in the neighborhood of $\cos(x/r) = 0$, with $r \to 8$, using *the Taylor polynomial* $1-x^2/2$.

Subtracting 1 and multiplying by $-2R^2$: $DB^2 \approx BC^2 + DC^2 - DC^2 BC^2/(2r^2)$. As r tends to infinity, the term $DC^2 BC^2/(2r^2)$ tends to zero, making the approximation tend to the exact equality: $\boldsymbol{DB^2 = DC^2 + BC^2}$.

2.5. Hypothesis 1

The Hypothesis 1 follows the first line of research (see *supra*, Section 1.3.1) and posits that earthquakes with magnitudes =M4.3 are connected to the conjunctions and oppositions of the seven planets of the Solar System, along with the Moon and the Sun in relation to Earth. To substantiate this, we aim to illustrate that *specific angular distances DB* of these celestial bodies, as observed from the earthquake's epicenter, correlate with earthquake magnitudes within short observation periods: usually hours instead of weeks or months.

Within 48 hours of an earthquake, we consistently monitored the positions of the seven Solar System planets, the Moon, and the Sun relative to the observer on Earth. We found that a meaningful statistical correlation emerges when the number of precise planet pair conjunctions or oppositions with Earth increases, resulting in higher average earthquake magnitudes (see *infra*, Section Results, 3.1).

2.6. Developing the Hypothesis 1 method

Empirical evidence indicates that when we examine the angular distance BD (Fig. 2) between the seven planets of the Solar System (excluding Pluto), the Moon, and the Sun in pairs, relative to an observer on Earth within the earthquake's epicenter's geographic area, *values approaching 0°, within a fixed BD tolerance of 0° -/+12°, become significant indicators of earthquake magnitudes.*

This value corresponds to $n(n-1)/2 = 36$ unique combinations of angle pairs formed by the 9 celestial bodies relative to Earth. The analysis proceeds graphically with software deriving values from astronomical tables, particularly the "angular distance" between celestial bodies observed from Earth. See Table 1 for software configuration. Data processing is facilitated by dedicated software named VS0P87 - Celestial Sphere - Delta. The software utilizes astronomical data and processes it according to the described method, providing the necessary values.

Table 1 DOI10.5281/zenodo.7746082, VSOP87 - Celestial Sphere - Delta Mask and Software, for Section 2.6

Aggregate results are presented in Results (see *infra*, Section 3.1).

2.7. Hypothesis 2

We discuss the role of *resultant gravitational forces (henceforth "FR")* as a vertical tidal force (see *supra*, Section 2 and *infra*, Discussion, 4.4) component affecting seismic activity.

The Hypothesis 2 suggests that the primary factor influencing seismic triggering isn't the absolute magnitude of FR from the lunar-solar system and Solar System planets. Instead, it's the *stability/ unstability fluctuations of FR within 24-48 hours of an earthquake that matter most.* We assess these fluctuations through change values or *standard deviations of FR (henceforth "*σFR*)*, introducing a *novel aspect to existing researches.*

Experimental evidence shows a stronger link between seismic activity and the Solar System's seven planets σFR, surpassing the Luni-Solar system's influence (see *infra*, Section 3.1.1). Testing the hypothesis indirectly measures FR by observing the angles (see *supra*, Section 2.3) formed by planets concerning an earthquake's epicenter. These findings are relevant *over hours* rather than extended astronomical observations.

2.8. Developing the Hypothesis 2 method

To examine the Hypothesis 2, we turn to vector physics. This involves creating vectors for all the FR generated by the planets to Earth and measuring their values. *The FR expressed in Newton's results from the sum of the product of the two force vectors, each multiplied by the cosine of the adjacent angles.* This theory is grounded in Newton's Law of Universal Gravitation [30].

Also this data processing is facilitated by dedicated software named VS0P87 - Celestial Sphere - Delta. The software utilizes astronomical data and processes it according to the described method, providing the necessary values. By appropriately entering the date and other data, see the URL of the data setting mask that enables the calculation of the resultant gravitational force FR, in Table 2.

Table 2 DOI10.5281/zenodo.7734562, VSOP87 - Celestial Sphere - Delta Mask and Software, for Section 2.8.

In the context of this study, where the number of FR to be measured at each time "t" exceeds two vectors, it is more convenient *to represent these vectors in coordinates* and then simply add them component by component. Practically speaking, for each of the n=9 celestial bodies – Sun, Moon,

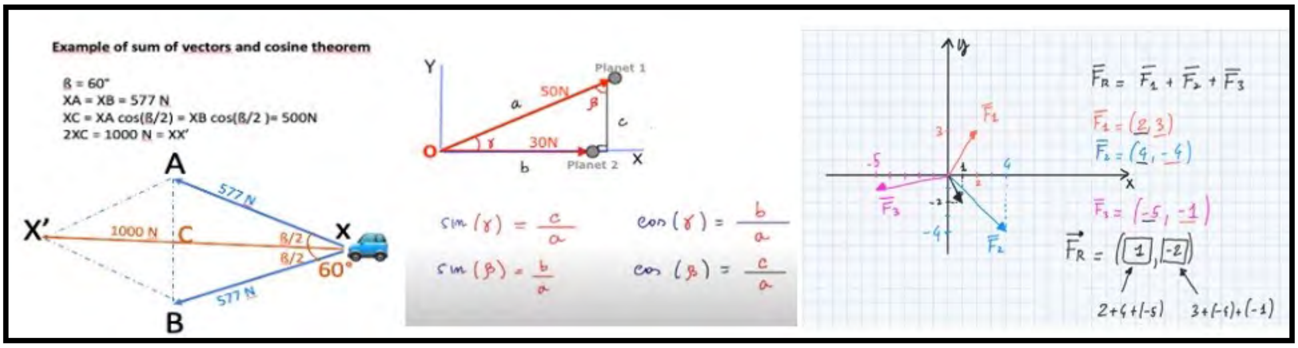

Figure 2. **Vector calculation of the resultant gravitational force FR.** a) Example of the sum of 2 vectors exerting equal force; b) Vector Newton forces of 2 planets and the Earth; c) Example of the sum of 3 vectors and their resultant force. We calculate the total of these vectors at any time by

summing the FR (the resultant gravitational forces) of two celestial bodies, each multiplied by the cosine of the adjacent half-angle, *according to Carnot's theorem* (Figure 2,a). After placing on the abscissae the FR vector $\vec{b}$ (expressed in Newtons, henceforth “N”) N(0) of Earth/Sun, with coordinates (b,0), the other vectors (n), with n ∈ (2,9), have Cartesian coordinates $\vec{a}$ (n) cos γ, a(n) sin γ, with n ∈ (2,9) and constitute the N(n) force of one of the 9 planet/Earth combinations (figure 2,b). In the case of at least three forces, *the resultant gravitational force FR would be to be calculated according to the scheme in Figure 2,c.*

Mercury, Venus, Mars, Jupiter, Saturn, Uranus, Neptune – we calculate the resulting gravitational force vector exerted during the Astro/Earth interaction at every instant to Earth.

Consequently, the total N FR acting on the Earth at the Observation point O is: Ntot =￼ expressed in Newtons. Moreover, we can establish a connection between the angle γ in Figure 2,b and the angular distance value proposed in the Hypothesis 1 of this study (see *supra*, Section 2.4, Figure 1).

If we consider the sum of all abscissa values as "A," and the sum of all ordinate values as "B," the total FR N then: **FR (t) (N tot) = ^{2}v (A^2+B^2).**

The resulting gravitational force FR(t) (N tot) [hereinafter referred to as **FR**] provides us with the absolute magnitude or intensity of the gravitational forces exerted by the 9 planets on the observation point O, positioned on the Earth's surface at time t. *By knowing this value at any given moment, we gain insight into the changing FR acting on or around the observation point over time.*

2.9. Three index values

Three index values are used to find correlations between FR and seismic triggering for all 200 experiments.

2.9.1. Variation in FR values (σFR) within two consecutive 24-hour blocks near the earthquake.

The first index, as standard deviation (σFR) of the average FR value of *two consecutive* 24-hour (henceforth “σ***48h***FR”, or parameter “A”) FR blocks is calculated. From 28 to 31 values in a month (1 value every 24h, depending on the length of the month), 14-15 *cumulative index values* are derived, representing a 62-hour time slot around the earthquake. When we mention *"cumulative,"* it means that if, let's say, the index value 3 identifies the earthquake time, it implies the accumulation of time corresponding to index 1 + index 2 + index 3.

These index values are sorted such that index 1 corresponds to the highest or lowest σ***48h***FR value of the month, index 2 to the second highest or lowest, and so forth up to index 14, for a total of 28 to 31 values per month. This graph is structured with hourly FR values over a reference month, positioning the earthquake's point at *the start of the fourth week*. This approach facilitates the analysis of FR behavior in the 3 weeks preceding and 1 week following the earthquake.

These values are shown in Line 29 of the data: see Table 3 and 4.

Table 3 DOI.5281/zenodo.7779003, Study of FR gravitational forces exerted by the angular distances of all 9 S.S. celestial bodies toward Earth: L'Aquila Earthquake, 06.04.2009, Italy, M6.1, for Section 2.9.

For the 2009 L'Aquila (Central Italy) earthquake, the pink band around Index 5 in Figure 3 indicates the time of the earthquake. In this example, the σ***48h***FR value with Index 5 is 4.5607E-11. See the value in: Cell SG31 of the data in Table 3; Earthquake n. 85, Point 2, of the list in Table 4 (see *infra*, Section 2.10).

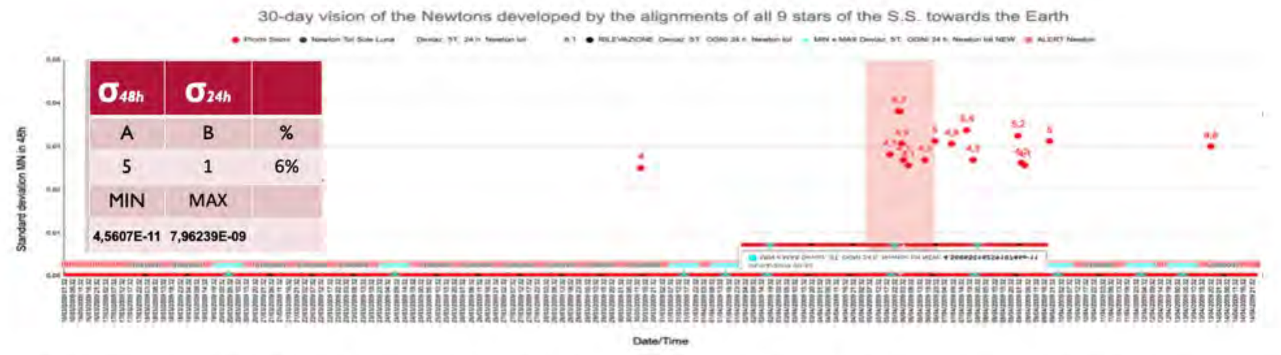

Fig 18 *Parameters A, B and the astronomical seismic alert time in 1 month identified by the two parameters used jointly, l'Aquila 6.04.2009, M6.1.*

Figure 3. The cumulative percentile of Alert Time of the earthquake l'Aquila (Central Italy), 6.04.2009, M6.1. The value of parameter A (σ48hFR) with Index 5 is 4.5607E-11. The value of parameter B (σ24hFR) with Index 1 is 7,96239E-09. The percentile of the Alert Time in 1 month is 6%.

2.9.2. Variations in FR values (σFR) across 24 one-hour intervals near the earthquake

The second index, as standard deviation of the average FR values of each 24-hour (henceforth "σ***24h***FR", or parameter "B") block is calculated. A month is divided into 28/30 periods of 24 hours each, yielding 696 hourly σ***24h***FR values calculated over 24-hour periods. These values are ordered into *cumulative* (see *supra*, Section 2.9.1) 347 index values, such that index 1 corresponds to the maximum or minimum σ***24h***FR value of the month, index 2 to the second maximum or minimum, and so on up to index 347. The 696 values σ***48h***FR are in line 35 of the drive (see *supra*, Section 2.9.1, table 3 and 4).

For the 2009 L'Aquila earthquake, Index 1 corresponds to the pink band around the earthquake time in Figure 2. In this example, the value of σ***48h***FR with Index 1 is 7,96239E-09. See the value in: Cell RZ35 of the drive in Table 3, Earthquake n. 85, Point 2, of the list in Table 4 (see *infra*, Section 2.10).

2.9.3. Percentile of Alert Time affected by σFR

The third index, as a percentile of the cumulative Alert Time within one month influenced by the combined σFR indices of the parameters σ***48h***FR and σ***24h***FR for each earthquake, is calculated. It serves as a measure of the quality of the values of the first two σFRs given above. As explained, when we mention *"cumulative,"* it means that if, let's say, the index value 3 identifies an Alert Time, it implies the accumulation of time corresponding to index 1 + index 2 + index 3.

The percentile values of the Alert Time for all 200 earthquakes are listed in Table 8 (see *infra*, Section Results, 3.2.4).

The percentile of the Alert Time of 2009 L'Aquila earthquake is shown in Figure 2: in this example the Alert Time occupies the sixth percentile (6%) within a month.

2.9.4. Three lines of experimental analysis

We conducted a total of 600 gravitational force measurements around the earthquakes, with 200 measurements for each of the three following lines of analysis:

1. The gravitational forces exerted individually by the seven planets of the Solar System, the Sun, and the Moon toward Earth.

2. The gravitational force from the Luni-Solar System alone, excluding the seven planets of the Solar System directed toward Earth.

3. *The gravitational forces developed individually by the seven planets of the Solar System excluding the Sun and the Moon, toward Earth.*

Further details on the variations in data across these three Analysis Lines are discussed below (see *infra*, Section 4.2) and illustrate that the most dependable measurement, for purposes of identifying seismic triggering times and testing the hypothesis, lies within the analysis of Line 3.

2.10. Structure of the sample of 200 earthquakes

The structure of the sample of 200 earthquakes is outlined, considering a minimum magnitude of M4.3, from a total of 1,620 Italian earthquakes (ASMI-INGV Catalog) spanning from 1600 until 2022. See the earthquake list in Table 4).

Table 4 DOI10.5281/zenodo.8171569, APPENDIX – List of earthquakes, for Section 2.9.

Among these 200 earthquakes:

- *Eighty-five were randomly selected* using the Bernoulli sampling method from the 560 earthquakes =M4.3 in the 1600–1899 catalog.

- *Sixty were randomly selected* using the Bernoulli sampling method from the 1,060 earthquakes =M4.3 in the 1900–2022 catalog.

- *Fifty-five were purposefully* chosen from the 1,060 earthquakes =M4.3 in the 1900–2022 catalog.

2.10.1. Reliability of the sample

The consideration of 200 earthquakes with a minimum magnitude of M4.3, out of a total of 1,060 earthquakes in Italy from 1900 until 2022, constitutes a sample size of about 19% of the total. The sample selection includes the following.

1. One hundred and forty-five were chosen through Bernoulli sampling, representing 72.5% of the total, using a simple random sampling method. Each of these 145 units in the earthquake population had an equal probability of being included in the sample.

2. Fifty-five additional earthquakes were discretely chosen for study interest due to their occurrence within the last 120 years, making them earthquakes =M4.3.

A short video (see Table 6) demonstrates an example of the random sample extraction method used for selecting the 145 earthquakes.

Table 5 DOI.5281/zenodo.8083305, Random sample extraction of 145 earthquakes, for Section 2.10.1.

Note: During random sampling, earthquakes were substituted under certain conditions:

1. For foreign earthquakes (e.g., Slovenia), the model does not consider earthquakes outside Italy.

2. For earthquakes at sea (e.g., Tyrrhenian Sea), the model does not consider seaquakes.

3. For aftershocks occurring within one Moon phase of a mainshock, the parameters of Hypothesis 2 did not accurately detect the earthquake, possibly due to astronomical parameters not significantly influencing subsequent earthquakes following a strong mainshock.

4. Earthquakes were also replaced due to repetitions of already drawn numbers.

3. Results

3.1. Hypothesis 1

Analyzing 200 Italian earthquakes spanning from 1600 until 2022, a correlation between planetary positions and earthquake magnitudes emerged.

3.1.1. A Statistical correlation between planetary positions and earthquake magnitudes

Hypothesis 1 is substantiated: a statistical correlation exists between the positions of the planets, the Moon, and the Sun and earthquake magnitude. A recurring correlation between *angular measurements* of conjunctions and oppositions of the 36 pairwise combinations of the seven planets of the Solar System, the Moon, and the Sun and the magnitude intervals (Richter) of 200 Italian earthquakes =M4.3 (using ASMI-INGV data spanning from 1600 until 2022) is evident for both the 200 earthquakes since 1600 and the 63 earthquakes that occurred after 1988, which are also part of the 200-earthquake dataset analyzed. *This serves to assess the reliability of the earthquake catalog utilized for this study,* as will be discussed later (see *infra*, Section 4.6).

A trend toward higher average earthquake magnitudes corresponds to *more numerous and accurate alignments* of planet pairs: *more alignments are directly related to higher earthquake magnitudes.*

There is an *inverse correlation* between the magnitude of earthquakes *and the average angular distance* of planets from Earth and a *direct correlation* between the magnitude of earthquakes and the *number of planets in line* with Earth.

Besides, *the Moon's angular position does not substantially alter earthquake magnitude trends.* Although slight differences emerge when considering alignments of 36 planet pairs with the Sun and Moon or when excluding the Moon considering only 28 alignments, the trends remain consistent. (see Figure 4 and 5).

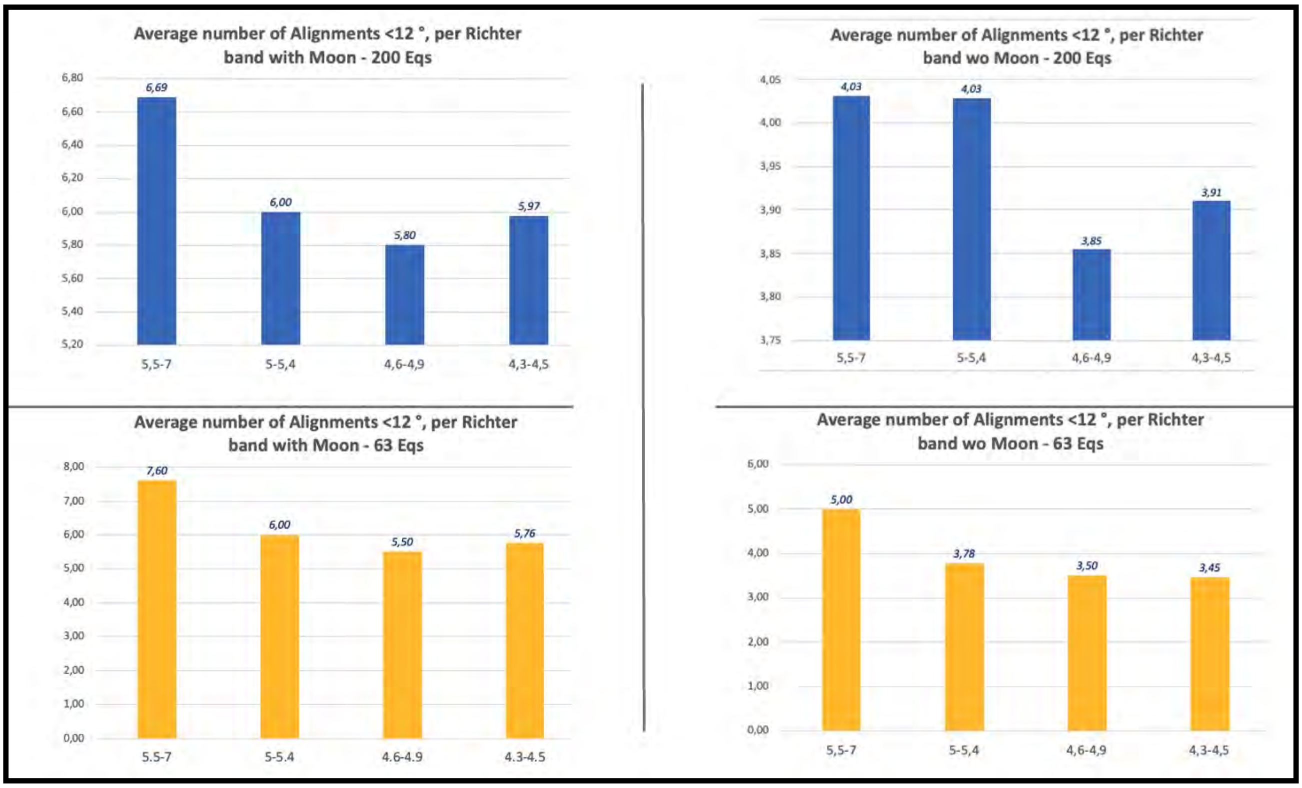

Figure 4. Distribution of average number of alignments <12° by magnitude range of earthquakes occurring after 1988. Average number of alignments <12° for each magnitude range (Richter), with the Moon (left graph) and without (right graph) at the triggering time of both the 200 earthquakes since 1600 and the 63 earthquakes that occurred after 1988. *The average number of alignments rises as the magnitude increases.*

Figure 4. Distribution of average number of alignments <12° by magnitude range of earthquakes occurring after 1988. Average number of alignments <12° for each magnitude range (Richter), with the Moon (left graph) and without (right graph) at the triggering time of both the 200 earthquakes since 1600 and the 63 earthquakes that occurred after 1988. *The average number of alignments rises as the magnitude increases.*

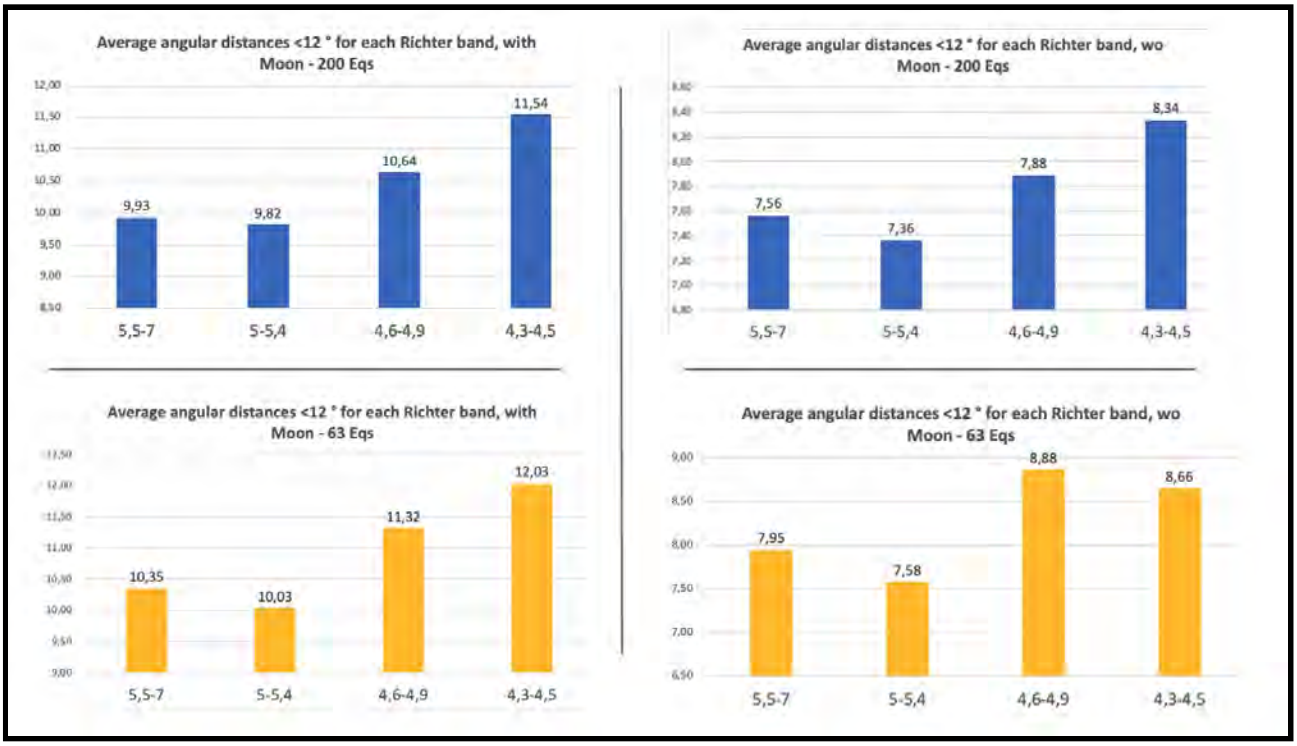

Figure 5. Distribution of average angular distance <12° by magnitude range of the 200 earthquakes. Average angular distance <12° for each magnitude range (Richter), with the Moon (left) and without (right graph) at the triggering time of both the 200 earthquakes since 1600 and the 63 earthquakes that occurred after 1988. *The average angular distance of alignments decreases as the magnitude increases.*

The observation that an increase in the magnitude of earthquakes corresponds to both an increase in the number of pairs of planets with close angular distance and a decrease in angular distance from Earth is *in line with Newton's Law of Universal Gravitation* (Newton 1687).

3.1.2. The distribution of the 200 average angular distances is normal

The distributions of average angular distance values (of Solar System bodies relative to the Observer on Earth) at the time of seismic triggering, for both the sample of 200 earthquakes since 1600 and the 63 earthquakes that occurred after 1988, *are normal.* The normality of the distributions was validated with a 95% confidence interval using the Shapiro-Wilks and *P-value tests (see Figure 6), with a p-value >0,05.* Thus, this is a *normal distribution* of the data suggesting that the distribution of these values *is not random.*

Table 6 presents the Excel file containing analytical and comparative outcomes between the two calculations: with the Sun and Moon and without the Moon, for both the sample of 200 earthquakes since 1600 and the 63 earthquakes that occurred after 1988.

Table 6 DOI10.5281/zenodo.10058522, Summary Excel tables of results of the first hypothesis, for both the sample of 200 earthquakes since 1600 and the 63 earthquakes that occurred after 1988, for Section 3.1.

Results

Parameter	Value
P-value	0.1531

Shapiro-Wilk test, using normal distribution (right-tailed)

Since n>50 we used the normal approximation to calculate the p-value.

1. H_0 hypothesis

Since p-value > α, we accept the H_0.

It is assumed that the data is normally distributed.

In other words, the difference between the data sample and the normal distribution is not big enough to be statistically significant. A non-significance result can not prove that H_0 is correct, only that the null assumption can not be rejected.

2. P-value

The p-value equals 0.1531, (P(x≤1.0231) = 0.8469). It means that the chance of type I error, rejecting a correct H_0, is too high: 0.1531 (15.31%). The larger the p-value the more it supports H_0.

Results

Parameter	Value
P-value	0.0675

Shapiro-Wilk test, using normal distribution (right-tailed)

Since n>50 we used the normal approximation to calculate the p-value.

1. H_0 hypothesis

Since p-value > α, we accept the H_0.

It is assumed that the data is normally distributed.

In other words, the difference between the data sample and the normal distribution is not big enough to be statistically significant. A non-significance result can not prove that H_0 is correct, only that the null assumption can not be rejected.

2. P-value

The p-value equals 0.0675, (P(x≤1.4947) = 0.9325). It means that the chance of type I error, rejecting a correct H_0, is too high: 0.0675 (6.75%). The larger the p-value the more it supports H_0.

Figure 6. **Normal distribution of average angular distances <12° at the trigger time of the 200 earthquakes.** The distribution of the 200 average angular distances <12° at the time of seismic triggering (with the Sun and the Moon on the left, without the Moon on the right) is validated with a 95% confidence interval using the *Shapiro-Wilks and P-value tests*, *with a p-value of 0.1531 (left graph).* Interestingly, the average angular distances calculated including the Moon along with the seven planets and the Sun showed a better fit to a normal distribution compared to the same calculations excluding the Moon, that shows *a p-value of 0,0675 (right graph)*. The p-value for the distribution of average angular values including the Sun and Moon of the sample of 63 earthquakes that occurred after 1988 is 0.0506. While the p-value excluding the Moon from the calculation is 0.1542 (see Table 6). *The normality of all distributions in this section was then validated with a p-value >0.05.*

3.2. Hypothesis 2

In Sections 3.2.1 to 3.2.4 we will show the results of FR indices (see *supra*, Section 2.9). Whereas in Section 3.2.5 we will show the results of FR values, from which the indices originate.

Overview and details of the 200 analyzed earthquakes, including the values and indices for the σFR parameters A, B and the percentile of the alert time in the three lines of analysis, are provided in Table 9 and 10 (see *infra*, Section 3.2.6).

3.2.1. The σFR indices distributions

The initial outcome deduced from assessing the Hypothesis 2 is the presence of two non-random distributions in the range of the three σFR indices (parameters A, B and % Alert Time) of the 200 earthquakes.

Results were well approximated using logarithmic functions Y=ln(x) for σFR values and *polynomial functions* of the form a+bx+cx²+dx³+…dxn, where n ∈ (1.8) for σFR indices and for the percentile of the Alert Time.

The regression R² values (as shown in the example in Figure 7) *result close to 1*, indicating *a strong fit between theoretical and real distributions* of the three σFR indices (parameters A, B and % Alert Time) for all the 200 earthquakes.

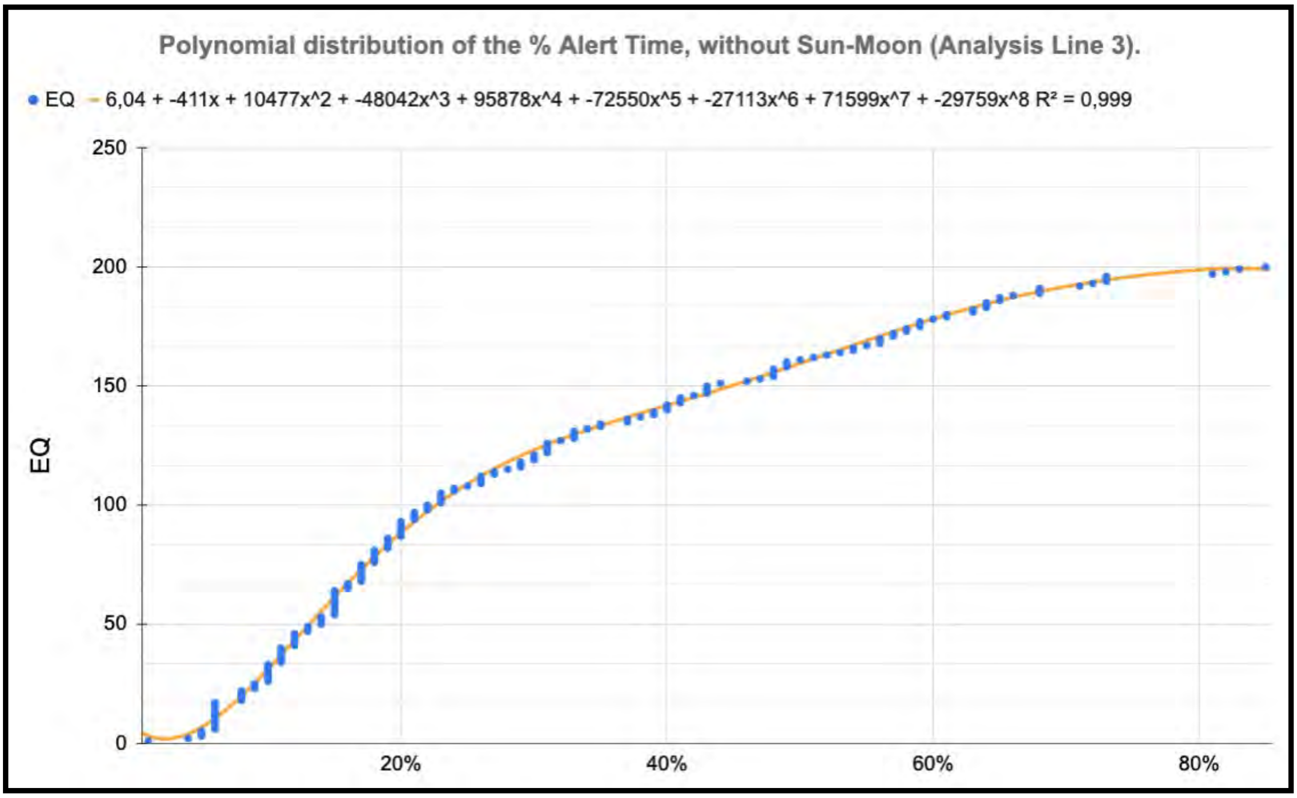

Figure 7. Polynomial distribution of the % Alert Time, without Sun-Moon (Analysis Line 3). Notably, the most reliable distribution for identifying seismic trigger Alert Times for all 200 earthquakes is *the formula describing the distribution of percentile Alert Time* influenced by σFR during triggering within 1 month, *found in Analysis Line 3*: $Y = 6.04-411x+10477x^2-48042x^3+95878x^4-72550x^5-27113x^6+71599x^7-29759x^8$ (See Table 8 for details). This particular polynomial distribution boasts an *impressive regression coefficient R² of 0.999, the closest value to 1 in the entire study.* This result holds true when compared to the R^2 values of the other two Analysis Lines (see *infra*, Figure 8).

It follows that new data regarding a 201st earthquake (σFR indices, values and percentiles of the Alert Time of an nth earthquake) could likely be placed on the distribution curve with minimal error.

Excluding the Sun and Moon from the angle calculations resulted in R² being closer to a value of 1 than the calculation including them. So, *Analysis Line n.3 was identified as the most promising due to its regression index R² closest to 1* ("all planets, without Moon and Sun", see *supra,* Section 2.9.4).

The summarized regression R² coefficients are presented in Figure 8.

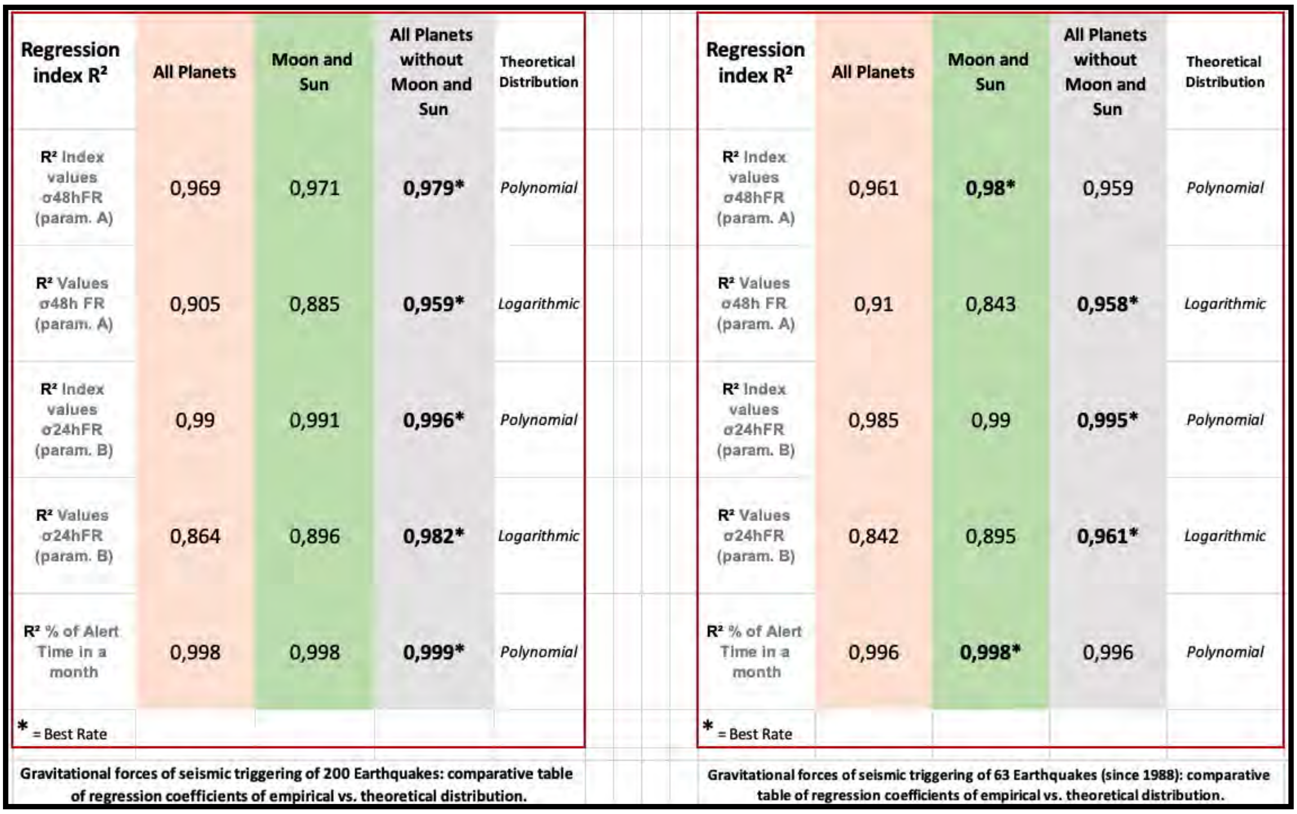

Regression index R^2	All Planets	Moon and Sun	All Planets without Moon and Sun	Theoretical Distribution
R^2 Index values σ48hFR (param. A)	0,969	0,971	**0,979***	*Polynomial*
R^2 Values σ48h FR (param. A)	0,905	0,885	**0,959***	*Logarithmic*
R^2 Index values σ24hFR (param. B)	0,99	0,991	**0,996***	*Polynomial*
R^2 Values σ24hFR (param. B)	0,864	0,896	**0,982***	*Logarithmic*
R^2 % of Alert Time in a month	0,998	0,998	**0,999***	*Polynomial*
* = Best Rate				

Gravitational forces of seismic triggering of 200 Earthquakes: comparative table of regression coefficients of empirical vs. theoretical distribution.

Regression index R^2	All Planets	Moon and Sun	All Planets without Moon and Sun	Theoretical Distribution
R^2 Index values σ48hFR (param. A)	0,961	**0,98***	0,959	*Polynomial*
R^2 Values σ48h FR (param. A)	0,91	0,843	**0,958***	*Logarithmic*
R^2 Index values σ24hFR (param. B)	0,985	0,99	**0,995***	*Polynomial*
R^2 Values σ24hFR (param. B)	0,842	0,895	**0,961***	*Logarithmic*
R^2 % of Alert Time in a month	0,996	**0,998***	0,996	*Polynomial*
* = Best Rate				

Gravitational forces of seismic triggering of 63 Earthquakes (since 1988): comparative table of regression coefficients of empirical vs. theoretical distribution.

Figure 8. Summary/comparative table of the R^2 regression coefficients of the 3 parameters identifying σFR. This table presents a summary and comparison of the regression R^2 coefficients for the three σFR indices (parameters A, B, and % Alert Time) for both the 200 earthquakes (on the left) and the 63 earthquakes occurring after 1988 (on the right) across the three lines of analysis. Notably, the regression coefficient R^2 of 0.999 in Analysis Line No. 3 (on the left) is the closest value to 1 in the entire case study. Similarly, the right graph, representing the R^2 regression coefficients for the 63 earthquakes occurring after 1988, yields results very similar to those on the left, indicating once again that *Analysis Line No. 3 exhibits values closest to 1*, than the other two, even for the most recent sample of earthquakes.

The comprehensive examination of the R^2 regression coefficients of the 200 earthquakes being studied, including Parameters A and B, as well as the percentiles of Alert Time within a one-month period across the three Analysis Lines, is illustrated in Table 7.

Additionally, Table 7 presents identical analysis for the *63 earthquakes occurring after 1988,* which are also part of the 200-earthquake dataset analyzed. *This serves to assess the reliability of the earthquake catalog utilized for this study,* as will be discussed later (see *infra*, Section 4.6).

Table 7: DOI 10.5281/zenodo.10058668, **Summary graphs of the data distributions of the** Hypothesis 2**, with the R^2 regression values** of the three σFR values and indices (parameters A, B and % Alert Time) of both the 200 earthquakes and the 63 earthquakes after 1988, for Section 3.2.

3.2.2. The σFR concentration of data at lower values

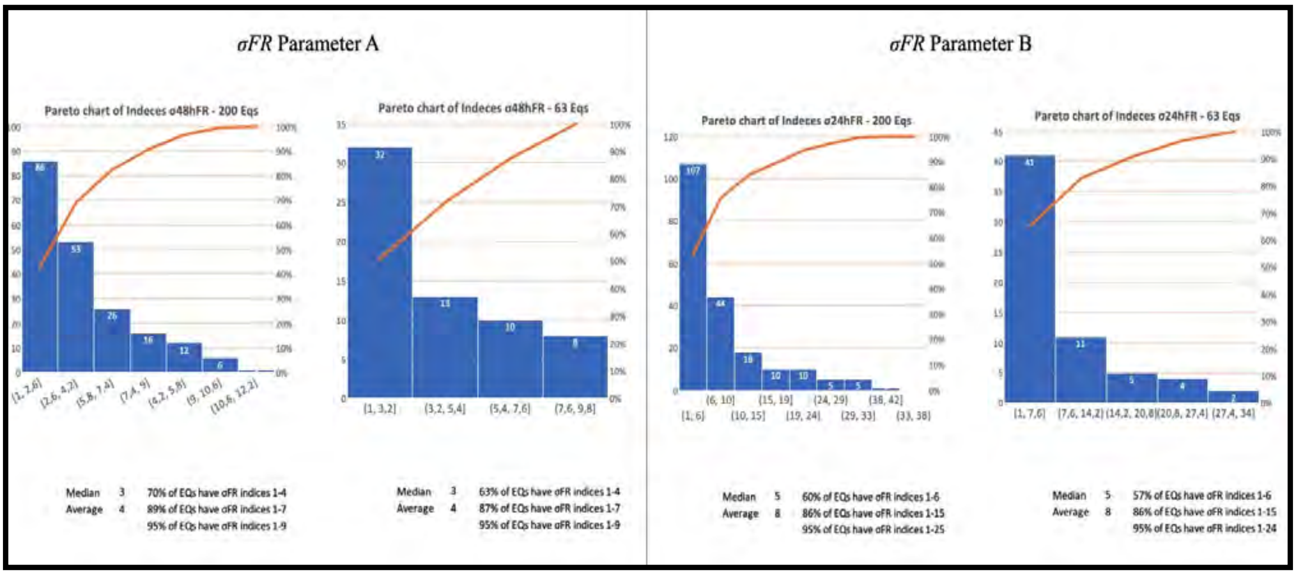

Figure 9. Distribution of σFR indices of parameter A (left graph) and of parameter B (right graph). This figure presents a summary of the distribution and a comparison of σFR indices between the sample of 200 earthquakes and the sample of 63 earthquakes within the reference month for both parameter A (Left) and parameter B (Right). Following the line of analysis No. 2 graphs show that both distributions have a *median value (parameter A) of 3* and 95% of the earthquakes are concentrated within a low σFR index value of 9 (the maximum possible σFR index value is 14, see *supra*, Section 2.9.1); For the other σFR index (parameter B), however, both distributions have *a median value of 5*, and 95% of the earthquakes are concentrated within a consistently low σFR index value of 24-25 (the maximum possible σFR index value is 347, see *supra*, Section 2.9.2). As explained, index 1 corresponds to the highest or lowest σFR value of the month, index 2 to the second highest or lowest value, and so on. For the remaining lines of analysis, specifically No. 1 and 3, *the data concentration shows a striking similarity for both the 200 earthquakes since 1600 and the 63 earthquakes that occurred after 1988*. Refer to Table 8 for details.

A second result comes from the analysis of the *σFR indices obtained: they are concentrated around very low values.*

The concentration of σFR indices at such low values for both parameters A and B gives us a useful indication: *earthquakes are triggered by high or low σFR values, while moderate σFR values do not trigger earthquakes* (See *supra*, Graphical Abstract).

Table 8 summarizes the values of the three σFR indices (parameters A, B, and % Alert Time) for:

- both the 200 earthquakes from 1600 to 2022 and the sample of 63 earthquakes after 1988;
- for the three lines of Analysis (see *supra*, Section 2.9.4).

Additionally, Table 8 presents identical analysis for the 63 earthquakes occurring after 1988, which are also part of the 200-earthquake dataset analyzed. *This serves to assess the reliability of the earthquake catalog utilized for this study,* as will be discussed later (see *infra*, Section 4.6).

Table 8 DOI_10.5281/zenodo.10058786, **Summary distribution and probability** of the three σFR indices (parameters A, B and % Alert Time) **of the** Hypothesis 2 for both the 200 earthquakes and the sample of 63 earthquakes after 1988, for the three lines of Analysis.

3.2.3. The probability distribution of σFR

A third outcome results from the probability analysis by which we obtained the values of the three σFR indices (parameters A, B and % Alert Time) of the 200 earthquakes.

The statistical probability that the three observed σFR indices (parameters A, B, and % Alert Time) had those low values for the three lines of analysis is also significantly reduced for the 200 earthquakes, with a probability of less than $3.18x10^{-34}$. While for the 63 earthquakes the probability is less than $2.81x10^{-11}$.

The calculation of the statistical probability of the three σFR indices (parameters A, B and % Alert Time) of both the 200 earthquakes and the sample of 63 earthquakes after 1988, at the time of seismic triggering for the three lines of analysis, is presented in Table 8.

3.2.4. The distribution of percentile Alert Time

In Table 8 (see *supra*, Section 3.2.2) we examined the histogram and Pareto plot of the σFR indices and percentiles *of the Alert Times* affected within one month of both the sample of 200 earthquakes and the sample of 63 earthquakes after 1988. All three lines of analysis of both samples show a *clear concentration of results in a narrow range of values.*

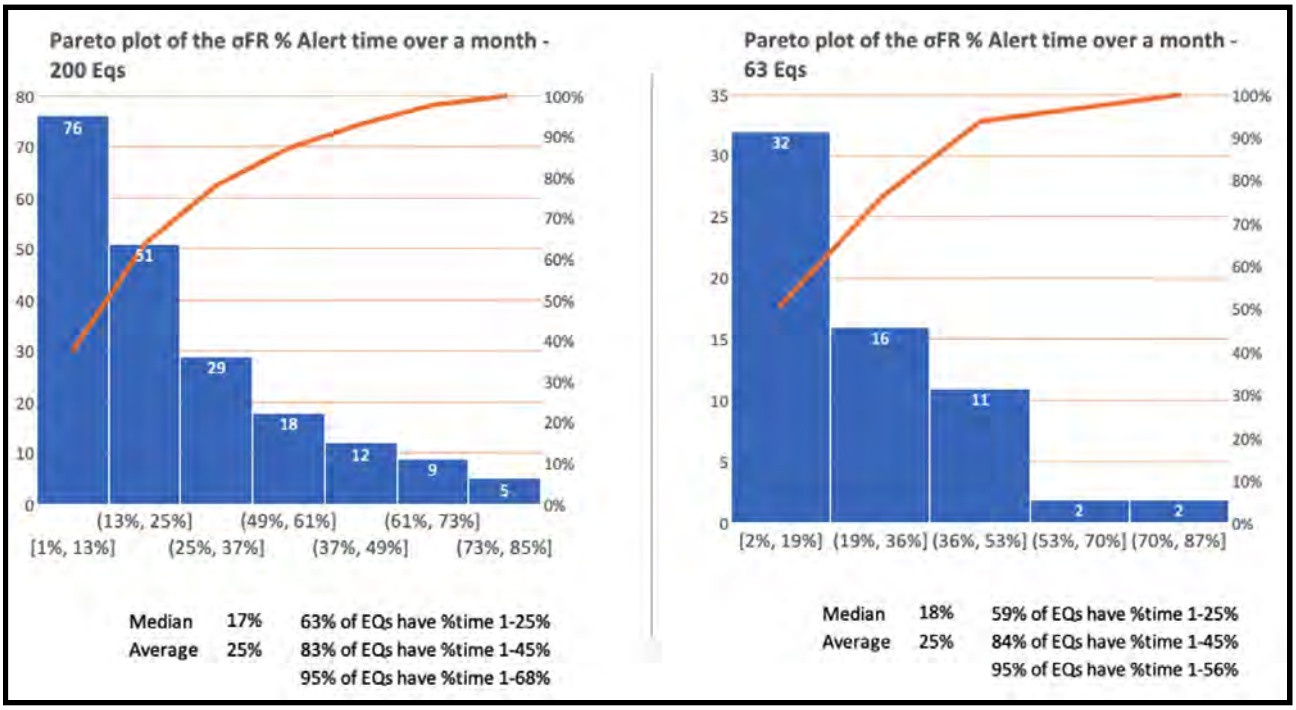

Figure 10. Pareto plot of the percentile Alert time over a month. This figure presents a summary and comparison of the σFR % Alert Time for both the 200 earthquakes (on the left) and the 63 earthquakes occurring after 1988 (on the right) for the reference month. Following the line of analysis No. 1 graphs show that both distributions have a median % Alert Time value of 17-18%. Besides, *95% of the earthquakes are concentrated within a narrow % Alert Time of 56-68%.* For the remaining lines of analysis, specifically No. 2 and 3, *the data distribution (Pareto plots and histograms) also shows a striking similarity* for both the 200 earthquakes since 1600 and the 63 earthquakes that occurred after 1988: refer to Table 8 for details.

By correctly applying the two parameters of σFR A and B, it is possible, for example, for Analysis Line 1 to observe that not less than 64 percent of both the 200 earthquakes and the 63 earthquakes occurring after 1988 fall within just 25 percent of the Alert Time for the reference month (see Figure 10).

By integrating the findings from the Pareto chart with the previously discussed R^2 regression indices (see *supra*, Section 3.2.1), it becomes highly probable that a newly assigned percentile Alert Time value (X) for a specific n^{th} earthquake (Y), influenced by the same σFR during seismic triggering, *can be situated on the same theoretical curve with minimal error*.

The concentration of 95 percent of earthquakes in a reduced % Alert Time frame in all three Analysis Lines, indicating measurable and *probably non-random behavior,* allows these data to be used to contribute to a *plausible earthquake prediction model*.

Overview and details of the 200 analyzed earthquakes, including the % Alert Time in the three lines of analysis, are provided in Table 9 and 10 (see *infra*, Section 3.2.6).

3.2.5. The range of σFR values for seismic triggering

Now let's talk about σFR values. The summarized σFR values are presented in Table 8 (see *supra*, Section 3.2.2).

Based on the 200 experiments, it is also possible to establish the range of σFR values for both Parameters A and B that can confidently indicate *that earthquakes =M4.3 will not occur beyond these values.* This confidence arises because the values align along a theoretical logarithmic-type curve with a regression index R^2 very close to 1.

For example, Table 8 (see *supra*, Section 3.2.2) shows for Analysis Line 3 the identification σFR Parameter A values ranging from a minimum of 2.32×10^{-28} (6.29×10^{-26} for the 63 earthquakes since 1988) to a maximum of 4.90×10^{-16} (8.56×10^{-17}), and σFR Parameter B values ranging from a minimum of 3.36×10^{-32} (7.00×10^{-30}) to a maximum of 5.88×10^{-18} (8.20×10^{-17}) within the values of the theoretical polynomial curve mentioned earlier (see *supra*, Section 3.2.1).

The orders of magnitude of the maximum and minimum values of σFR *appear congruent,* for both the 200 earthquakes since 1600 and for the 63 earthquakes that occurred after 1988.

Overview and details of the 200 analyzed earthquakes encompassing values for σFR Parameters A and B are provided in Table 9 and 10 (see *infra*, Section 3.2.6).

3.2.6. Overview and details of the 200 analyzed earthquakes

Overview of the 200 earthquakes analyzed including the values and indices for the parameters σFR A, B and the percentile of the Alert Time in the three Lines of Analysis is given in Table 9.

Table 9 DOI_10.5281/zenodo.10061252, **Overview of the 200 analyzed earthquakes encompassing values and indices for σFR Parameters A, B, and the percentile of Alert Time across the three Analysis Lines.**

Details of the 200 earthquakes analyzed including the values and indices for the parameters σFR A, B and the percentile of the alert time in the three lines of analysis are given in Table 10. This table encompasses the 200 Excel calculation files, with 3 tabs for each, because of the three Analysis Lines.

In each of the 600 Excel sheet tabs (200 tabs for each of the 3 Lines of Analysis) the main values are:

- Index σFR Parameters A: cell A36
- Index σFR Parameters B: cell A26
- Value σFR Parameters A: cell A25
- σFR Parameters B value: cell A23, if minimum value
- σFR Parameters B value: cell A24, if maximum value
- Percentile of alert time in the month: cell A34

Table 10 DOI_10.5281/zenodo.8163189, **Overview and details of the 200 analyzed earthquakes encompassing values and indices for σFR Parameters A, B, and the percentile of Alert Time across the three Analysis Lines.**

The earthquakes list in Table 4 is also relevant here (see *supra*, Section 2.10).

4. Discussion

In this chapter, the author of this paper highlights key aspects for discussing the two hypotheses put forth in this study: whether the gravitational influences of the seven planets of the Solar System, along with the Moon and the Sun, can truly impact earthquake triggering (Hypothesis 2) and their magnitudes (Hypothesis 1).

Additionally, considerations are made regarding the different values of FR and tidal force exerted by celestial bodies in the Solar System on Earth.

I also address a portion of the literature that failed to find a causal relationship between tides and seismic triggering, using the results of this study to demonstrate that these theories do not contradict our findings.

4.1. Comparison with previous studies

The results of this study are not congruent with previous studies that have addressed correlations between earthquakes and planetary positions. Chinese and Indian schools, as well as smaller Italian investigations, have mainly focused on demonstrating the co-occurrence of conjunctions or oppositions of celestial bodies for specific earthquakes and have not provided in-depth statistical results (see *supra*, Section 1.3).

4.3. Gravitational and tidal forces in the Solar System

Considering the tidal accelerations exerted by planets on Earth, tides stem from the difference between gravitational acceleration within Earth and at its center. Moon and sun is causative agent in the formation of tides. Tidal is a natural phenomenon caused by the gravitational force of attraction between moon and sun [31]. Tidal forces decrease inversely with the cube of distance. Notably, gravitational forces diminish inversely with the square of the distance between objects.

The following table highlights the comparative orders of magnitude for maximum tidal forces from the seven planets versus the Moon's impact on Earth (Figure 10). Intriguingly, the *Sun's gravitational attraction FR on Earth exceeds the Moon's by over 166 times at perigee and perihelion, while the Sun's tidal force is only 41% of that of the Moon's.*

4.4. Gravitational force as a component of vertical tidal force

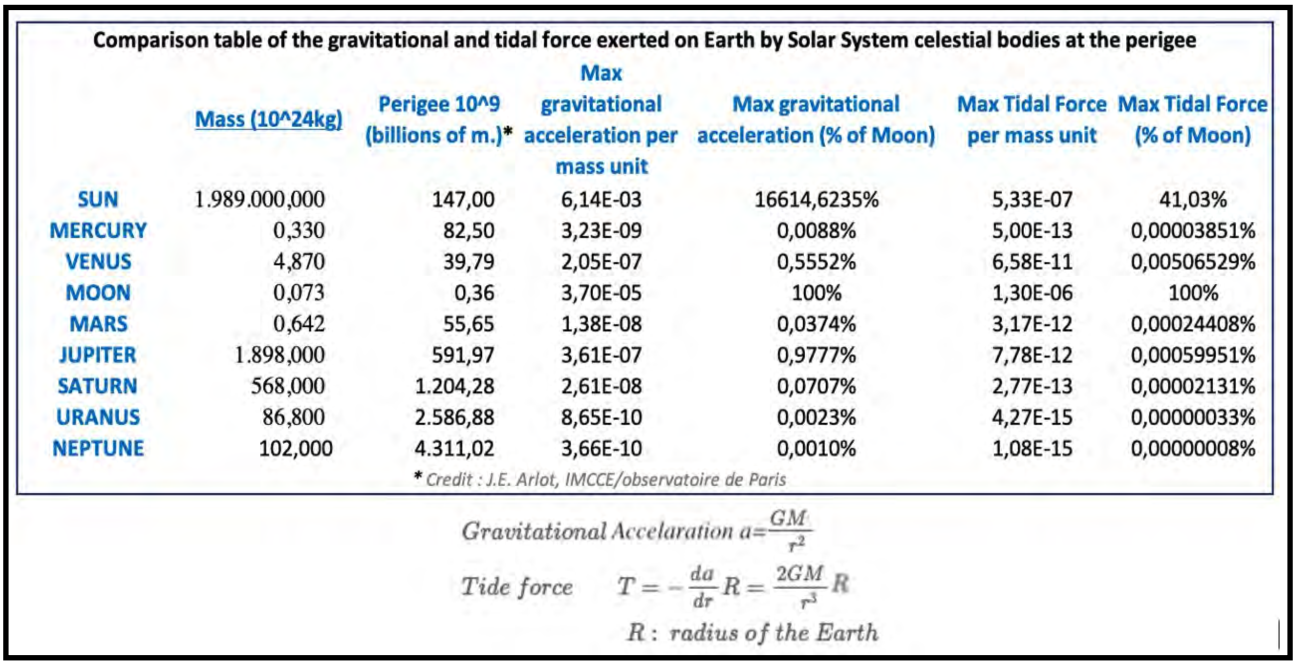

Comparison table of the gravitational and tidal force exerted on Earth by Solar System celestial bodies at the perigee

	Mass (10^24kg)	Perigee 10^9 (billions of m.)*	Max gravitational acceleration per mass unit	Max gravitational acceleration (% of Moon)	Max Tidal Force per mass unit	Max Tidal Force (% of Moon)
SUN	1.989.000,000	147,00	6,14E-03	16614,6235%	5,33E-07	41,03%
MERCURY	0,330	82,50	3,23E-09	0,0088%	5,00E-13	0,00003851%
VENUS	4,870	39,79	2,05E-07	0,5552%	6,58E-11	0,00506529%
MOON	0,073	0,36	3,70E-05	100%	1,30E-06	100%
MARS	0,642	55,65	1,38E-08	0,0374%	3,17E-12	0,00024408%
JUPITER	1.898,000	591,97	3,61E-07	0,9777%	7,78E-12	0,00059951%
SATURN	568,000	1.204,28	2,61E-08	0,0707%	2,77E-13	0,00002131%
URANUS	86,800	2.586,88	8,65E-10	0,0023%	4,27E-15	0,00000033%
NEPTUNE	102,000	4.311,02	3,66E-10	0,0010%	1,08E-15	0,00000008%

* *Credit : J.E. Arlot, IMCCE/observatoire de Paris*

$$Gravitational\ Accelaration\ a = \frac{GM}{r^2}$$

$$Tide\ force \quad T = -\frac{da}{dr}R = \frac{2GM}{r^3}R$$

$$R:\ radius\ of\ the\ Earth$$

Figure 11. **Chart of the gravitational and tidal force per mass Earth unit at the perigee.** This is a comparative table of the tidal and gravitational forces exerted by celestial bodies in the Solar System at perigee. These insights emphasize the significant differences in gravitational and tidal components between celestial bodies in the Solar System.

The answer to this question lies in the experimental findings of this study, specifically in the behavior of the resulting gravitational forces (σFR) from the Sun, Moon, and the seven planets of the Solar System. Given that earthquakes occur when the fault reaches a critical energy threshold and the vertical tide's component can contribute to the trigger (see *supra*, Section 2) it is suggested that *σFR is a contributor to the vertical tidal force that influences seismic activity.*

This hypothesis emerges considering the experimental trends and behaviors, although it *does not establish a direct cause-and-effect mechanism between gravitational forces and vertical tides*. Yet, the observed bidirectional relationship between the positions of celestial bodies, gravitational forces, and earthquakes *supports the idea that the σFR play a role in the vertical tidal force.*

4.5. Gravitational force and gravity acceleration

The gravitational force between masses m and M is described by Newton's law of gravity (with G as the gravitational constant): $Fg = GmM / r^2$, where r is the distance. Gravitational acceleration (force per unit mass) of body M due to body m can be defined as $a = Fg / m = GM / r^2$, as per Newton's second law.

In this study, we could have used acceleration of gravity, but since Earth's mass is constant and the focus is on the change in force (σFR) during earthquakes, not the force magnitude (see *supra,* Section 2.12), Earth's mass does not affect the outcome. *Whether Earth's mass is included or excluded, the index values of σFR remain the same.*

The gravitational force (FR) is a component of the tidal force. Tides stem from the difference in gravitational attraction between different parts of a celestial body. Newton's law of gravity ($Fg = GmM / r^2$) describes the force between masses m and M. The variation of attraction between two objects located at distances r and r+dr is obtained by deriving the expression of gravitation relative to r: $dF / dr = -GMm/r^3$, revealing the *tidal effect to be inversely proportional to the cube of distance.* For the Earth–Sun system, the tidal force is about half that of the Earth–Moon system due to the $r^3 = r \times r^2$ relationship.

While tidal force could be used in calculations, it does not change the outcome of σFR, similar to gravity. Adding or removing *1/r* in calculations would yield *identical σFR index values.*

4.6. The reliability of the ASMI-INGV catalogs

The scientific significance of the manuscript can be also questioned. For this study, the quality of the seismicity catalog is essential. It can be argued that the catalog is complete (covers all earthquakes above the magnitude threshold) for the entire period analyzed (1600-2023). The accuracy of the time of occurrence of historical earthquakes can be questioned. Therefore, this point needs careful verification.

Regarding the catalog's quality, it's essential to understand that conducting a scientific study relies on using the data from this source. It's worth noting that this is the sole official catalog in Italy, managed by INGV, and represents the most authoritative data source available. The Italian Historical Macroseismic Archive ASMI [28] offers access to information on over 6500 Italian earthquakes spanning from 461 BC to 2020, extracted from more than 430 seismological investigations.

For each earthquake, various studies based on the ASMI catalog are accessible*, and the results, concerning dates and times for each earthquake*, are the most plausible among the multiple hypotheses presented in the referenced studies.

We compared the results of Hypothesis 1 and Hypothesis 2 by considering *63 earthquakes* out of the 200 M=4.3 in the entire list, all of which *occurred after 1988*. These earthquakes are more recent and thus were subject to further analysis.

For these 63 earthquakes we then considered the *National Seismic Network (RSN), Italy's permanent nationwide seismological network*, managed by the National Institute of Geophysics and Volcanology (INGV) with contributions from collaborating institutions and observatories [32]. Metadata have been *available online since 1988*, thus constituting an accurate time reference for each earthquake that has occurred.

In this study, we consistently compared the outcomes of the analysis involving all 200 earthquakes with those derived from the examination of the 63 most recent earthquakes M=4.3. The findings related to Hypothesis 1 and Hypothesis 2 for the smaller and more recent sample of 63 earthquakes *were consistent with those obtained from the larger and less recent sample of 200 earthquakes.*

5. Conclusion

This study's main conclusion is that seismic triggering for earthquakes M=4.3 is driven not by the absolute gravitational force from celestial bodies but *by extreme stability or instability of the standard deviation of FR (σFR) within a 24–48-hour window*.

The quantification of the tidal force range and resulting gravitational force (FR) values for seismic triggering had not been previously attempted, *nor had an approximate theoretical formula for identifying the stress point of a fault* and the need for energy release been formulated. In terms of the first calculation, this study computed the σFR resulting from celestial bodies in the Solar System on Earth.

A recurring range of σFR values (standard deviation of FR) was established around seismic trigger on the Earth: outside this σFR range, the occurrence of earthquakes =M4.3 was *highly unlikely.*

The cumulative gravitational/tidal force from these bodies acting on a specific Earth point determines the stability parameter for vertical tidal force and seismic triggering.

This approach of calculating the resultant gravitational force in terms of change value (σFR) instead of absolute value (FR) *marks a substantial departure from existing literature.* Additionally, earthquake magnitudes seem to correlate with planetary conjunctions/oppositions, with the Moon possibly playing a less significant role than commonly assumed.

5.1. Indirect data measurement

This study does not employ direct ground-based measurements via gravimeters for understanding Earth's seismic triggers due to external gravitational forces. Instead, it innovatively utilizes *computational methods relying on ephemerides (planet positions),* azimuth-elevation coordinates, and vector physics. This indirect method calculates FR for each instant at earthquake locations.

5.2. Broader influence of planets

Contrary to conventional beliefs, *the most reliable σFR* distribution for seismic triggers across 200 experiments omits the Moon and Sun from the computation (see *supra,* Figure 8 in Section 3.2.1). While their gravitational and tidal forces are less than those exerted by the Sun and Moon, the gravitational forces generated by the seven planets within the Solar System exhibit a meaningful correlation with Earth's tidal influences. In essence, *the somewhat modest impact of these planetary gravitational forces introduces a disruptive factor that fosters seismic triggers.*

5.3. Vertical tidal component on fault

FR values from the Sun, the Moon, and the seven planets create a vertical tidal component toward Earth's crust, where earthquake-triggering faults are situated. This influence extends beyond a single fault, affecting a larger region of Earth, roughly matching the locations of the examined earthquakes.

Earthquakes materialize when the fault reaches a critical threshold, wherein the vertical tide's component influences triggering. This can occur in diverse ways based on tectonic context—lithostatic loading encourages normal faults while hindering reverse faults (see *supra*, Section 2).

5.4. Applying study results for earthquake forecasting

These preliminary study findings suggest considering an exponential distribution model involving two components, A and B, of the standard deviation of FR (σFR) from the Solar System's seven planets, the Sun, and the Moon during earthquakes. *This model could potentially help reduce uncertainty in earthquake timing predictions.* Using these results, up to 35% of the time an earthquake warning is given in a person's lifetime can be eliminated for the 95th percentile of earthquakes =M4.3. This implies that 95% of earthquakes fall within a maximum of 65% of the potential earthquake warning time of a month, with a median of 17%, a pattern worth exploring for its possible *non-random nature.*

5.5. Frequency of astronomical phenomena

The analyzed period covers 422, during which Earth aligns with at least one planetary pair numerous times—roughly every 193for each planet. Calculations based on average synodic times for planet–Sun–Earth conjunctions/oppositions reveal that *Earth aligns with the Sun and another planet every approximately (193/8 planets) 24.*

Over these 422 years, around 1,590 earthquakes =M4.3 have occurred, translating to an average of about one every 97.

Utilizing VS0P87 processing, an average of at least one alignment =12° angular distance occurs every 1.5between the seven planets, the Sun, and the Moon relative to the Earth. This implies that the 422-year period experiences a *substantial frequency of angular alignments from the oppositions and conjunctions described in Hypothesis 1, and these alignments are not negligible.*

5.6. Importance of a comprehensive approach

While the current model demonstrates a non-random correlation between planetary angular positions and earthquakes, it lacks the precision necessary for "good predictions" in terms of time and space. *Combining this correlation model with a multidisciplinary approach and suitable ground-based instrumentation might yield more accurate forecasts*. Detecting seismic precursors (see also *supra*, Section 1.2) such as small earthquakes [8], magnetic phenomena [5], neutron emissions [4], radio waves [3], and radon [9] could aid in definitively identifying the epicentral zone. While future ephemerides and modeling could provide time "windows," ground-based instrumentation is essential for precise epicenter and magnitude determination.

Presently, seismographic prediction models, such as those utilizing ground-based instrumentation, can accurately predict earthquake magnitudes. However, establishing a widespread and dependable ground-based *instrumental network, especially in Italy, remains a significant financial challenge in the near term.*

5.7. Study limitations for effective earthquake forecasting

Given the nearly daily frequency of these alignments, it is challenging to establish a strong correlation between them and earthquake magnitudes, and it requires complex statistical verification—a subject for future studies. Consequently, *predictions based solely on the presented astronomical model are likely to yield numerous false alerts, rendering them impractical for effective earthquake forecasting.*

In the case of the 2009 L'Aquila (Central Italy) earthquake (see, *supra*, Section 2.9.3), we saw that the percentage of Alert Time found by analyzing the lowest FR indices was 6%. A very good percentage, which allowed in that case to eliminate 94 percent of the time in a month, identifying a very narrow time in which *theoretically the Civil Defense Authorities could have concentrated.*

The crucial point to note is that 95% of earthquakes with a magnitude of =M4.3 don't exhibit such a low percentile of Alert Time but instead occur within 65% of the Alert Time within one month, as shown above (see *supra*, Section 3.2.4). This finding while an important result of our study, *if used alone, however proves to be a significant practical obstacle to a "good seismic forecasting" at least for earthquakes =M4.3.*

References

[1] H. Yanben, L. Zhian, and H. Hui, “Interdisciplinary Studies of Astronomical Factors and Earthquakes in China,” in *Geodesy on the Move*, vol. 119, R. Forsberg, M. Feissel, and R. Dietrich, Eds., in International Association of Geodesy Symposia, vol. 119. , Berlin, Heidelberg: Springer Berlin Heidelberg, 1998, pp. 465–471. doi: 10.1007/978-3-642-72245-5_77.

[2] M. Kachakhidze, N. Kachakhidze-Murphy, B. Khvitia, and G. Ramishvili, “Large Earthquake Prediction Methods,” *OJER*, vol. 08, no. 04, pp. 239–254, 2019, doi: 10.4236/ojer.2019.84014.

[3] V. Straser, D. Cataldi, G. Cataldi, and G. G. Giuliani, “Pre-Seismic Signals Recorded By The Italian RDF Network Before The Occurrence Of Some Earthquakes In Northern Italy,” *International Journal of Software & Hardware Research in Engineering*, vol. 9, no. 1, Jan. 2021, doi: 10.26821/IJSHRE.9.1.2021.9123.

[4] A. Carpinteri and O. Borla, “Acoustic, electromagnetic, and neutron emissions as seismic precursors: The lunar periodicity of low-magnitude seismic swarms,” *Engineering Fracture Mechanics*, vol. 210, pp. 29–41, Apr. 2019, doi: 10.1016/j.engfracmech.2018.04.021.

[5] Rod. Wolf, “On the periodic return of the minimum of sun-sport; the agreement between those periods and the variations of magnetic declination,” *The London, Edinburgh, and Dublin Philosophical Magazine and Journal of Science*, vol. 5, no. 29, pp. 67–67, Jan. 1853, doi: 10.1080/14786445308646906.

[6] J. F. Simpson, “Solar activity as a triggering mechanism for earthquakes,” *Earth and Planetary Science Letters*, vol. 3, pp. 417–425, Jan. 1967, doi: 10.1016/0012-821X(67)90071-4.

[7] V. Marchitelli, P. Harabaglia, C. Troise, and G. De Natale, “On the correlation between solar activity and large earthquakes worldwide,” *Sci Rep*, vol. 10, no. 1, p. 11495, Jul. 2020, doi: 10.1038/s41598-020-67860-3.

[8] G. Riga and P. Balocchi, “Information and Predictive Oscillators of Energy Earthquakes,” *OJER*, vol. 08, no. 03, pp. 201–222, 2019, doi: 10.4236/ojer.2019.83012.

[9] C.-C. Fu *et al.*, “Gamma Ray and Radon Anomalies in Northern Taiwan as a Possible Preearthquake Indicator around the Plate Boundary,” *Geofluids*, vol. 2019, pp. 1–14, Sep. 2019, doi: 10.1155/2019/4734513.

[10] F. Di Stefano *et al.*, “Natural radioactivity and radiological hazard for humans: A simple introduction for newbies and students. New perspectives and innovative teaching methods,” *Atti Accad. Pelorit. Pericol. Cl. Sci. Fis. Mat. Nat.*, vol. 99, no. S1, pp. A40-1-A40-12, Sep. 2021, doi: 10.1478/AAPP.99S1A40.

[11] V. Gitis, A. Derendyaev, and K. Petrov, “Analyzing the Performance of GPS Data for Earthquake Prediction,” *Remote Sensing*, vol. 13, no. 9, p. 1842, May 2021, doi: 10.3390/rs13091842.

[12] Ö. Aydan, *Earthquake Science and Engineering*, 1st ed. London: CRC Press, 2022. doi: 10.1201/9781003164371.

[13] G. Plinius Secundus, *Storia naturale*, Rist., vol. II. Torino: Einaudi, 2005.

[14] C.-H. Lin, Y.-H. Yeh, Y.-I. Chen, J.-Y. Liu, and K.-J. Chen, “Earthquake Clustering Relative to Lunar Phases in Taiwan,” *Terr. Atmos. Ocean. Sci.*, vol. 14, no. 3, p. 289, 2003, doi: 10.3319/TAO.2003.14.3.289(T).

[15] S. Kilston and L. Knopoff, “Lunar–solar periodicities of large earthquakes in southern California,” *Nature*, vol. 304, no. 5921, pp. 21–25, Jul. 1983, doi: 10.1038/304021a0.

[16] M. Caputo and G. Sebastiani, “Time and space analysis of two earthquakes in the Appennines (Italy),” *NS*, vol. 03, no. 09, pp. 768–774, 2011, doi: 10.4236/ns.2011.39101.

[17] R. Z. Ren Zhenqiu, “河北大地震与朔望关系的剖析,” *Chin. Sci. Bull.*, vol. 27, no. 10, pp. 617–620, May 1982, doi: 10.1360/csb1982-27-10-617.

[18] S. MAHMUD, *UNIQUE REASON OF EARTHQUAKE*. S.l.: LAP LAMBERT ACADEMIC PUBL, 2020.

[19] Ketkar, R, Viladkar, M. N.;, and Agrawal, P. N., “Study of Co-seismic Planetary Conditions for Earthquake Prediction",” *International Conferences on Recent Advances in Geotechnical Earthquake Engineering and Soil Dynamics. 15.*, 1991, [Online]. Available: https://scholarsmine.mst.edu/icrageesd/02icrageesd/session12/15

[20] Jeganathan, C., Gnanasekaran, G., and Tanushree Sengupta, “Analysing the Spatio-Temporal link between Earthquake Occurrences and Orbital Perturbations induced by Planetary Configuration,” *International Journal of Advancements in Remote Sensing, GIS and Geography*, vol. 3, no. 2, pp. 123–146, 2015.

[21] A. Schuster, “On lunar and solar periodicities of earthquakes,” *Proc. R. Soc. Lond.*, vol. 61, no. 369–377, pp. 455–465, Dec. 1897, doi: 10.1098/rspl.1897.0060.

[22] H. Hui and L. Xiaoming, “Research on Correlation of Positions of Celestial Objects with Earthquakes,” *Natural Hazards*, vol. 23, no. 2/3, pp. 339–348, 2001, doi: 10.1023/A:1011115708096.

[23] L. Métivier, O. de Viron, C. P. Conrad, S. Renault, M. Diament, and G. Patau, “Evidence of earthquake triggering by the solid earth tides,” *Earth and Planetary Science Letters*, vol. 278, no. 3–4, pp. 370–375, Feb. 2009, doi: 10.1016/j.epsl.2008.12.024.

[24] S. Ide, S. Yabe, and Y. Tanaka, “Earthquake potential revealed by tidal influence on earthquake size–frequency statistics,” *Nature Geosci*, vol. 9, no. 11, pp. 834–837, Nov. 2016, doi: 10.1038/ngeo2796.

[25] T. H. Heaton, “Tidal Triggering of Earthquakes,” *Geophysical Journal International*, vol. 43, no. 2, pp. 307–326, Nov. 1975, doi: 10.1111/j.1365-246X.1975.tb00637.x.

[26] Z.-Y. Ding, J.-K. Jia, and R. Wang, “Seismic triggering effect of tidal stress,” *Tectonophysics*, vol. 93, no. 3–4, pp. 319–335, Apr. 1983, doi: 10.1016/0040-1951(83)90289-5.

[27] D. Zaccagnino, F. Vespe, and C. Doglioni, “Tidal modulation of plate motions,” *Earth-Science Reviews*, vol. 205, p. 103179, Jun. 2020, doi: 10.1016/j.earscirev.2020.103179.

[28] A. Rovida, M. Locati, A. Antonucci, and R. Camassi, “Archivio Storico Macrosismico Italiano (ASMI),” p. 6000 earthquakes, 670 data sources, 30000 macroseismic intensity data points, Jun. 2017, doi: 10.13127/ASMI.

[29] P. Bretagnon and G. Francou, "VizieR Online Data Catalog: Planetary Solutions VSOP87 (Bretagnon+, 1988)," *VizieR Online Data Catalog*, p. VI/81, May 1995.

[30] I. Newton, *Philosophiæ naturalis principia mathematica*. in Early English Books Online / EEBO. Jussu Societatis Regiae ac Typis Josephi Streater. Prostat Venales apud Sam. Smith ad insigna Principis Walliae in Coemiterio D. Pauli, aliosq, nonnullos Bibliopolas, 1687. [Online]. Available: https://books.google.it/books?id=-3RXspUecy4C

[31] N. S. Mohamad and K. Chellappan, "The relationship between total electron content (TEC), tides phenomena and the position of moon and sun during the full moon and new moon in Selangor," in *2015 International Conference on Space Science and Communication (IconSpace)*, Langkawi, Malaysia: IEEE, Aug. 2015, pp. 277–282. doi: 10.1109/IconSpace.2015.7283766.

[32] Istituto Nazionale di Geofisica e Vulcanologia (INGV), "Rete Sismica Nazionale (RSN)," p. approx. 27 GB per day of new waveform data, approx. 415 active seismic stations, the archive totals to more than 600 distinct seismic stations, Dec. 2005, doi: 10.13127/SD/X0FXNH7QFY.

Declarations

Ethics approval and consent to participate

Not applicable

Consent for publication

Not applicable

List of abbreviations

FR → Resulting Gravitational Force exerted by the planet of the Solar System, the Moon and the Sun.

σFR → Standard Deviation of the Resulting Gravitational Force

Availability of data and materials

You can find data and materials in the Zenodo repository

Competing interests

The authors declare that they have no competing interests.

Funding

This study was not financially supported by any institution.

Authors' contributions

All authors read and approved the final manuscript.

Acknowledgements

We thank for the support to this Research, provided with numerous suggestions, especially: Carlo Doglioni (INGV President, Italy), Paolo Gasperini (Department of Physics, Geophysics Sector, University of Bologna), Luigi Cavaleri (ISMAR - CNR, Venice, Italy), Francesco Celani, (INFN, Frascati, Italy), Daniele Cataldi, LTPA Observer Project group.

We thank for meticulous checking of the text Roberto Pigro (MD, PhD Università degli Studi di Udine, Cipro).

Finally, we thank for supporting my public interventions the mathematician Claudio Pace (Terni, Italy).

About Hydrogen Deposits

V.V. Gordienko[1] , I.V. Gordienko[1], Ya.A. Goncharova[2], V.N. Tarasov[1]

(1) S.I. Subbotin Institute of Geophysics of the National Academy of Sciences of Ukraine
(2) V.K.Gusak Institute of Emergency and Reconstructive Surgery. National Academy of Medical Sciences of Ukraine.

Abstract

A review of data on sources and sinks of hydrogen of various origins in the atmosphere and in the near-surface part of the earth's crust is given (in some cases we are talking about the crust as a whole). Based on the results of the consideration of this information, it was concluded that the influence of underground non-biogenic ("geological, (white)") hydrogen on the content and balance of gas in the atmosphere, up to the stratosphere, is insignificant. The complexity of the experimental determination of the flow of geological hydrogen, free of biogenic and anthropogenic interference, the influence of the testable excavation, etc. is obvious. Probable sources of deep hydrogen are considered: the remains of magmatic gases (outside the areas of volcanism), metamorphic reactions, and radiolysis of water. The possibility of significant H2 export is evident only in currently activated fault zones.

The data on the most powerful suppliers of geological hydrogen - modern active volcanoes and thermal fields - are given. The gas circulation scheme of the Avacha volcano is built, based on the thermal model. The latter is controlled by data from geothermometers, the results of direct temperature measurements in deep wells, and a velocity model. The possibility of fumaroles carrying unchanged hydrogen from the magma chamber has been shown.

The prospects for the formation of hydrogen deposits are assessed as uncertain. Magmatic and metamorphogenic gas in some areas is formed enough to accumulate a significant deposit over several tens of thousands of years. But the possibility of its preservation during this period or longer raises doubts. Hydrocarbon deposits without material input from great depths can lose reserves in much less time. Higher rocks‘ permeability to hydrogen contributes to much greater gas leaks.

Keywords: hydrogen sources and sinks, geological (white) hydrogen, prospects for deposit formation.

Introduction

The article is primarily a compilation review of a data set, parts of which are used in two sections of Earth Sciences: 1. atmospheric physics and chemistry and 2. geological phenomena involving molecular hydrogen (H_2). When considering publications on the first topic, one gets the impression that the information they provide is useful for the second. This applies not only to hydrogen, but in this case, the authors limit themselves to this gas, which in recent years has attracted the attention of specialists working in both of these sections [Polevanov et al., 2020, Ehhalt et al., 2009, etc.].

Atmospheric researchers (at least some of them) pay attention to the existence of the most powerful “geological” H_2 generators [Ehhalt et al., 2009, Lin et al., 2005, etc.], but do not include them in gas balance schemes, since they produce gas less than the calculated errors for sources and sinks of anthropogenic, biogenic and atmospheric (chemical and photochemical) nature. Authors of publications about “geological (white)” hydrogen (WH) often consider its influence on objects below and above the Earth’s surface, without taking into account the presence in these environments of significant quantities of H_2 of another origin. Exceptions are quite rare [Bogdanov et al., 2000, Lin et al., 2005, Zgonnik, 2020, etc.]. Therefore, it is logical to start the review with atmospheric (we use this term for brevity) hydrogen - AH.

Atmospheric hydrogen

Parts of the AH balance are presented in Table 1 as elements of the global tropospheric cycle [Ehhalt et al., 2009, Pieterse, 2012, Pieterse et al., 2011, etc.] (mutually agreed upon for a particular year) and do not contain estimates of errors inherent in individual calculations of the components. The errors (uncertainties) are quite significant - 5-25%, especially when determining the absorption of hydrogen by soil.

Table 1. Components of the atmospheric hydrogen balance in Tg/year (Tg is 10^{12}g).

Supply		Absorption	
Burning fossil fuels	17	Oxidation of OH	22.1
Biomass combustion	15	Soil uptake	55.8
Bacterial fixation N_2	8	Total	77.9
Photochemical processes	37.3		
Total	77.3		
Total H_2 content in the troposphere		155±10*	
Update time		About 2 years	

* According to [Novelli et al., 1999].

Some characteristics of hydrogen generation and absorption are shown in Fig. 1, mainly data from [Ehhalt et al., 2009] were used.

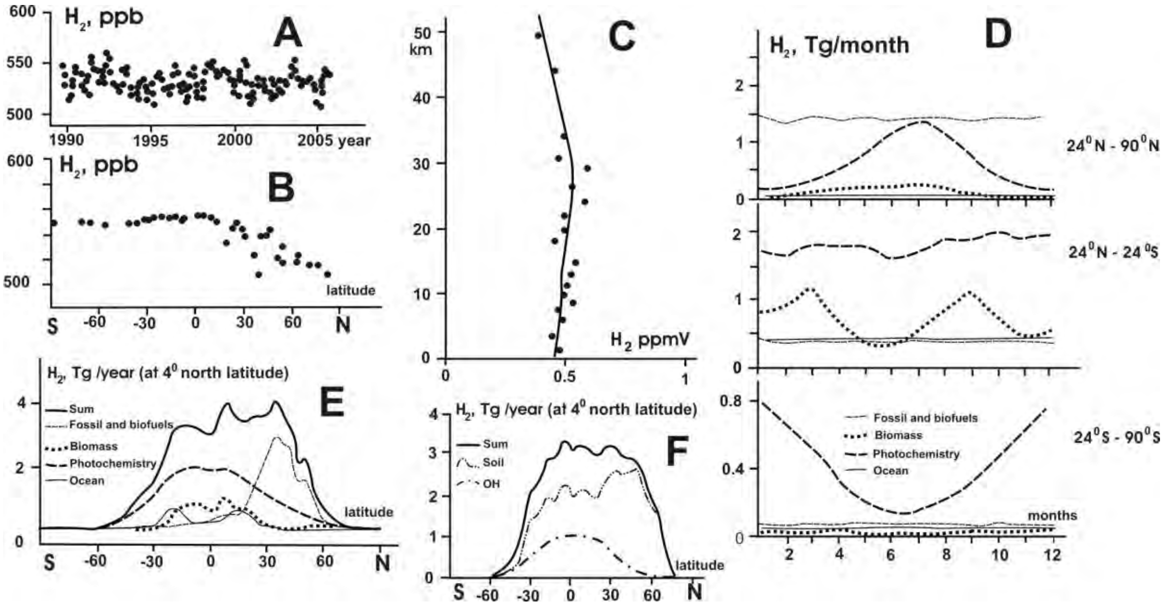

Fig. 1. Geographical confinement of the parameters of the global circulation of atmospheric (including biogenic) hydrogen. A - change in the average terrestrial concentration of H_2 over time, B, C - change in the average annual concentration: B - by latitude, C - by height, D – the intensity of hydrogen generation in different latitudinal zones during the year, E, F - latitudinal changes in the intensity of different: E - AH sources, F – AH absorbers.

Options with an outflow into the stratosphere of the order of 2 Tg/year [Xiao et al., 2007, etc.] and inflow from the stratosphere in smaller quantities are realistic. The dependences of the listed processes on temperature (T), insolation and environmental composition make it obvious that variations in the components by orders of magnitude are inevitable, which is confirmed experimentally on the Earth's scale. From Fig. 1A, we can conclude that the global average hydrogen content in the atmosphere (including the stratosphere – 1C) is stable for a long time, at least over the studied time interval. The low density probably ensures this gas, unlike others, penetration the tropopause not only in the tropics. On the other hand, horizontal flows turn out to be insufficient to eliminate the decrease in concentration at middle and high northern latitudes (Fig. 1B). Despite the production of much more hydrogen from fuel combustion here (Fig. 1E) than at the same latitudes in the southern hemisphere, soil absorption creates the observed imbalance (Fig. 1F) Obviously, the effect is related to the concentration of land in the northern hemisphere. Such differences are also clearly revealed in seasonal variations in H_2 generation in the tropics and mid-high latitudes (Fig. 1D).

The planetary balance of hydrogen in generalizations, where WH plays a significant role as a gas generator [Voitov, 1986, Zgonnik, 2020, etc.], practically repeats the atmospheric part (for the time corresponding to the publication). Data on the production of H_2 during geological processes differ sharply from each other. Their validity is questionable. In each case, when a significant contribution of WH to the overall balance is postulated, the source of hydrogen turns out to be, most likely, biogenic or a description of the results of modeling rather than experiment. The models overestimate the parameters (the thickness of basaltic lavas in oceanic basins, the serpentinized lower layer of oceanic crust, the productivity of MOR volcanism, the area of simultaneously existing thermal fields of the MOR, etc.) [Holland, 2002, Holloway et al., 2000, Lilley et al. , 1982, Sleep et al., 2007, Welham et al., 1979, Worman et al., 2016, etc.]. In the case of the work of [Gilat et al., 2012], it is an untested hypothesis of the development of the Earth as a whole. The energy effect of its proposed mechanism of planetary development (which supposedly suffices for all conceivable processes) is less than the background heat flow through the surface [Gordienko, 2017, etc.].
Turning to the array of described publications on WH, one can find arguments for any point of view, including opposing ones, from the same authors. For example, if we transfer the release of hydrogen into the atmosphere from the territory of Krivoy Rog to the area of the continental crust [Voitov, 1971], we obtain a figure comparable to all AH sources. Then on the shield, this value decreases by 3 orders of magnitude [Voitov, 1975], in generalization [Voitov, 1986] the productivity of the continental crust is even less and does not play a noticeable role in the Earth’s balance.

Hydrogen near the Earth’s surface

When using real experimental data, WH generation by all source options turns out to be at the level of 0.5 Tg/year (see below), i.e. tens of times lower than the absorption of hydrogen by soil, for example, in the middle latitudes of the northern hemisphere. In this regard, assessments of the situation at a shallow depth below the surface are interesting.
Direct studies of hydrogen [Lin et al., 2005, Onstott et al., 1998, etc.] of various origins at shallow depths show that “...biogenic H_2 still dominates abiotically produced H2 in shallow aquifer ecosystems... In deep subsurface environments,.. where there is little organic carbon, ... and H_2 concentrations are much higher than the threshold of enzymatic reactions, ... the biogenic contribution is small” [Lin et al., 2005, p. 13]. Hydrogen produced radiolytically even deeper is sufficient to support the life of microorganisms without another source. For the Earth as a whole, its flux (a conditional estimate for the entire surface area of the planet) is insignificant - about 0.01 Tg/year (i.e., an order of magnitude less than the estimate in [Voitov, 1975, 1986]), but the calculation of the hydrogen flux looks like this case, looks normal at the level of setting the problem (at least an attempt has been made to substantiate it) [Lin et al., 2005]. The formulas take into account real parameters: $D(d^2C/dz^2)=R$ and $J=-\gamma\cdot D(dC/dz)$, where: J ($\mu M/m^2\cdot year$) is the H_2 flow, R ($\mu M/year$) is the rate of H_2 production limited by the radiolysis procedure and bacterial consumption, D ($m^2/year$) is diffusion coefficient determined experimentally [Jaehne et al., 1987 and others], dC/dz ($\mu M/m$) is experimental concentration gradient, γ is effective rock porosity (~1%). Unfortunately, the method for determining the last parameter is not described. Significant variations are possible here [Nivin, 2013, etc.]. However data from other publications on the region indicate the reality of the value used.

The experimental values of hydrogen concentration in [Lin et al., 2005], established in the depth range of about 2.5 km, differ by an order of magnitude or more. The possibility of determining the vertical gradient is associated with detailed consideration of differences in the conditions of hydrogen diffusion, biogenic contributions, geological and hydrogeological situations (location in the

Witwatersrand formation, where absolute dating of successively formed layers was carried out [Lippmann et al., 2003]), acceptance of the idea of radiolysis genesis of gases. In general, it is difficult to consider the obtained result completely reliable.
In other estimates of the H_2 flux through the surface given in the literature, the calculation is not described at all. Direct measurements of flow, for example, from the walls of fresh mine workings, may contain significant errors [Nivin, 2013, etc.].
For comparison with AH absorption by soil at mid-latitudes of the northern hemisphere, the differences in the results of calculating the background WH flux are not significant: the absorption is greater than these values (Fig. 1F).

At depths in the subsoil where hydrogen concentrations are often measured, gas may also be present, coming from below and generated by biological processes without the participation of the atmosphere. For example, H_2 flux ~50 μM/m^2•year was calculated for a shallow aquifer in Lake City, South Carolina, based on acetate and formate fluxes [McMahon et al., 1991 and others]. The reaction supported by the generated heat is justified:
$C_6H_{12}O_6$ (glucose) + $4H_2O$ = CH_3COOH (acetic acid) + CH_2O_2 (formic acid) + $6H_2$ +$2CO_2$.
For comparison with the above values, let us estimate the result of a conditional recalculation of the flux to the surface of the entire Earth - 0.05 Tg/year. The value is small, but quite noticeable against the background of other sources that determine the observed subsurface gas concentrations and can affect the destruction of the soil layer.
The given examples indicate the real difficulty in detecting the WH fluxes (primarily evidence of their abiogenicity) and the need to create an experimental methodology that takes into account probable sources of interference. The latter are not limited to those listed.

Geological hydrogen

Oceans. When considering information about hydrogen entering the atmosphere from the bottom of the oceans, we also encounter the problem of diagnosing an abiogenic gas. The point of view about the deep (often mantle) origin of H_2 of thermal fields of mid-ocean ridges (MOR) is widespread and is based primarily on the complete or predominant absence of sediments on the MOR axes [Krayushkin et al., 2018, etc.]. The implication is that hydrothermal processing of accumulated organics is impossible without them. However, geochemists dealing with the problem more specifically (including the results of microbial activity) are far from drawing clear conclusions. The current state of knowledge of the fluid-gas complex can be summarized with the following quote. “There appears to be a consensus on mixed origins (both sources and processes), consistent with the ambiguous nature of the isotopic data. But the question remains: in what proportions? More systematic experiments as well as comprehensive geochemical approaches are needed to decipher hydrothermal geochemistry. This understanding is of paramount importance given the role of hydrothermal H_2, CH_4, and organic compounds in overall ocean balance, global cycles, and the origin of life.” [Konn et al., 2015, p.381].

The sources of the MOR thermal fields are beyond doubt: these are magmatic intrusions into the crust from shallow lenses of partially molten mantle rocks. There are about 500 of them, half have been studied to one degree or another, and the second is diagnosed by indirect signs. The average distance between them is estimated at 100 km. The source of WH (except for gas formed during melting and transported by magma) in the models under consideration is considered to be serpentinization or similar metamorphic processes involving hot fluids, which are dominated by sea water. The object of processing is basic and ultrabasic rocks of the lower part of the oceanic crust, previously metamorphosed under PT conditions, practically coinciding with those known for the lower layer of the continental crust [Gordienko, 2017, etc.]. The total amount of hydrogen produced by MOR is determined as 0.26-0.33 Tg/year [Cannat et al., 2010, Konn et al., 2015, etc.]. The H_2 flow per unit area of the thermal field can be estimated as 6 g/m^2·year. There are other estimates, but they either do not differ fundamentally from the one given or their validity seems insufficient to the authors.

The range of opinions about the nature of sources and sinks of hydrogen in the rest of the oceans is quite large. Not all of them can be classified as WH. Variations in the power of the sources are not very significant. If we exclude purely speculative models based on the canons of plate tectonics in their “pure form”, i.e. without involving specific geological facts (the author's negative attitude to this hypothesis is stated, in particular, in [Gordienko, 2017, 2019, etc.]), then the generation of hydrogen is associated with the same serpentinization (which is based on magmatic incursions into the crust, which themselves also carrying hydrogen) and by radiolysis of water. The amount of H_2 formed is about 0.1 Tg/year. Specific values depend on the pace of the process.

In contrast to the hydrogen flow over the MOR, it is not possible to directly control the flow over the basins. Therefore, we are not talking about the flow itself, but about the formation of H_2. Moreover, if the radiolysis procedure can be at least somehow controlled in terms of pace, then hydrolysis cannot. From the author's point of view, the value should not differ significantly from that available on continents in zones of recent activation (RA) and, accordingly, serpentinization of the lower crust. The zones occupy approximately half the territory of the ancient platforms and are somewhat larger than the rest of the land. The activation of basins has not yet been sufficiently studied, but to a first approximation, it can be considered comparable in relative prevalence to the continental one. Indeed, available estimates indicate similar values of hydrogen removal on continents and oceanic basins [Sherwood et al., 2014, etc.] – at the level of 0.1-0.5 Tg/year. If we determine the maximum value of the H_2 flow from these data as 0.5 Tg/year for the Earth as a whole, then per unit area of recent activation zones there will be 0.002 $g/m^2 \cdot year$.

Continents: Such a value cannot be reconciled with that required for oil and gas basins in the RA zones. For the conditions of Ukraine, the average value (over the area not of the fields, but of the entire basin) of hydrocarbons (HC) is approximately 0.1 tons of standard fuel per m^2 (t $s.f./m^2$). According to the scheme of formation of the partial melting zone in the middle part of the RA crust, fluid heat, and mass transfer last at least 50 thousand years [Gordienko, 2017, etc.]. To form the pool under consideration, a hydrogen flow of 0.6 $g/m^2 \cdot year$ will be required. Thus, beneath the oil and gas basins, the hydrogen flux should be two orders of magnitude higher than the average in the RA zones. Data on MOR show that the required and significantly greater power of sources in relatively small areas can be provided by known processes. The question remains about the reasons for such different intensities of H_2 generation within the same zones of recent activation. The calculation methods in the cited works (a summary of them is, in particular, in [Sherwood et al., 2014]) are not free from arbitrary assumptions. The authors believe that the proposed approach for assessing hydrolytic hydrogen generation is preferable. If we include all known hydrocarbon reserves in the area of activation zones on land, we obtain a hydrogen flux of 0.08 $g/m^2 \cdot year$. The area of oil and gas basins within the RA zones throughout the land cannot now be determined. Therefore, the reconciliation of data with Ukrainian data can only be indirect. In Ukraine it is about 15%, which gives a comparable (there is no need to talk about accuracy) hydrogen flux in oil and gas basins on land (0.5 $g/m^2 \cdot year$). The agreement is quite good, but it is necessary to find another way to estimate the hydrogen flux in RA zones outside oil and gas basins.

Significant variations are also present in estimates of another generator of hydrogen by crustal rocks – radiolysis [Nivin, 2013, Parnell et al., 2017, Savary et al., 1997, etc.]. But still, the limits of the calculated concentrations of radiolysis gas fall within approximately the same order of magnitude. In the rocks of the Khibiny alkaline massif, there is a fairly clear relationship between the concentrations of hydrogen and methane and the dependence of the latter on alkalinity, the increase of which correlates with an increase in radioactivity (Fig. 2).

The gas arising in this way is largely conserved in crustal rocks, as is part of the metamorphogenic hydrogen. For the purposes of the article, it is sufficient to divide abiogenic WH into those sealed together with other gases in weakly permeable inclusions (vacuoles) in solid rock (occluded gas - OG) and those located outside them in cracks (freely released gas - FRG), capable of limited movement. The volume of the latter is much larger than that of the occluded one.

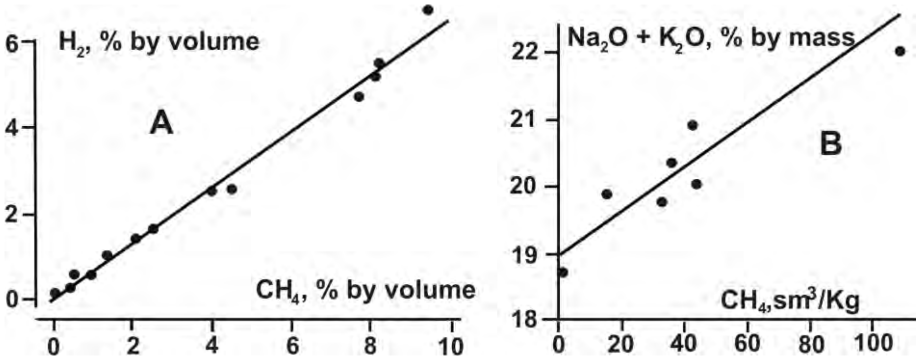

Fig. 2. Relationship between the concentrations of methane and hydrogen (A) and methane with the alkalinity of the rocks of the Khibiny massif (B) [Nivin, 2013].

The "intermediate" fraction contains diffusely scattered gases an order of magnitude less than OG [Nivin, 2013, etc.]. The connection between all gases is obvious, although for obvious reasons (different diffusion rates, chemical activity, etc.) there are no direct correlations between the components. For example, the radiolysis nature of part of the hydrogen in the OG is obvious. But "the most likely source of radiogenic oxygen gas appears to be radiolysis of water contained in rocks... The resulting equivalent amount of hydrogen is only a small part of its total concentration in gases." [Nivin, 2013, p. 191]. A significant volume of H_2 was formed during changes in rocks at shallow depths at low temperatures with the participation of meteoric waters.

In rocks with low permeability (igneous, metamorphic) at a sufficient depth, gas persists indefinitely, without participating in the creation of a flow through the surface. Wells and mine workings reveal reservoirs (fractured zones with associated void volumes) or small inclusions of FRG; extraction of OG is achieved only by crushing the rock and/or thermal stimulation of gas release. Many similar manifestations of hydrogen are described in the literature [Voitov, 1971, 1975, 1986, Ikorsky et al., 1992, Nivin, 2013, Essays..., 2018, Bjornstad et al., 1994, Coveney et al., 1987, Guélard et al., 2017, Lin et al., 2005, Parnell et al., 2017, Savary et al., 1997, Vovk, 1987, Zgonnik, 2020, etc.], which are provoked by the very procedure of invasion of the geological environment. In some cases, hydrogen appears to be partially man-made or associated with invasion-stimulated microbial generation. This expands the list of sources of interference in measurements. The observed releases of hydrogen in the described situations do not characterize its natural seepage from the depths to the surface. Tributaries often change rapidly over time (Fig. 3).

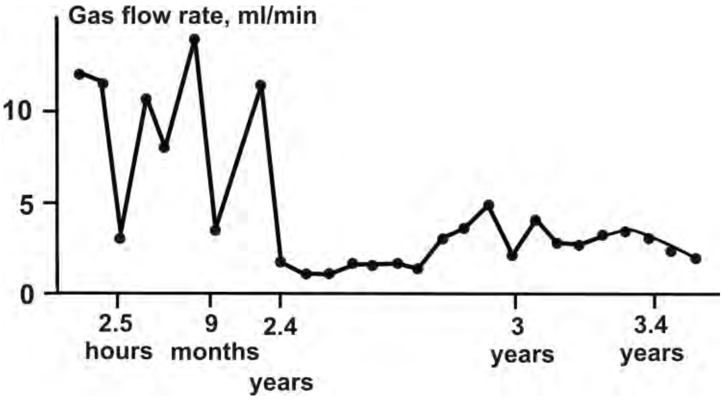

Fig. 3 Change in the intensity of hydrogen release into the blast hole [Nivin, 2013].

In zones of active (including geologically long-term) faults, hydrogen flows of varying intensity are often recorded. One example is the depth interval in which a well on the Nagolny Ridge intersects fractured zones that formed back in Cimmerian times [Murich et al., 1975] (Fig. 4).

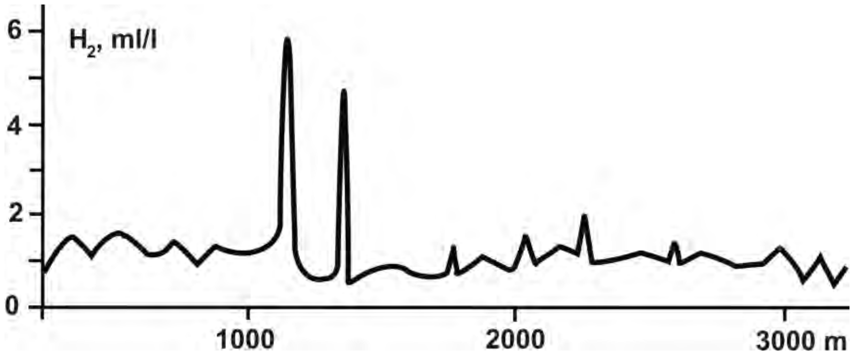

Fig. 4. Anomalies of hydrogen concentration near fractured zones intersected by a well.

The observed object can be considered a kind of hydrogen deposit. Naturally, we are not talking about a deposit of practical interest: the real power of the flow has not been studied. The very fact of its existence is interesting. There is no gas deposit formed here, which is opened by mining during prospecting. At the neighboring gold-sulfide deposit, there are no inclusions of hydrogen in the ore minerals [Tsilmak, 2016, Shumlyansky, 1994, etc.], they have been lost for approximately 180 million years since the formation of the deposit. The detected hydrogen flux is most likely associated with repeated (recent) activation.

According to available data [Romanova, 2023, etc.], hydrogen manifestations were discovered in similar geological settings in Lorraine and the western Pyrenees of France, in the fault areas of Oman, the USA, Mali, etc.

Such deposits should be widespread in areas of hydrothermal vents, especially in zones of recent activation of alpine geosynclines. Together with hydrogen, they carry methane, carbon dioxide, and helium to the surface and are often used for balneological purposes. You can dwell on the environmental aspect of such degassing and recent activation in general. In some publications [Gilat et al., 2012, Makarenko, 1997 etc.] these events are attributed to an extraordinary nature. Humanity should not assume that something normal is happening on the planet right now. It is necessary to actively search for places and phases of a possible catastrophic impulse of activity that can occur at any moment.

There are widespread ideas about the influence of gases extracted from the subsoil on the psyche of entire peoples in active regions and more local manifestations of neuropathy. An analysis of the available literature data suggests a low probability of such reactions to these gases. Only at very high concentrations, depleting the air of oxygen is hypoxia of brain cells possible with all the symptoms inherent in this disease. But such content is hardly achievable even in pools with thermal waters [Environmental…].

Using the hydrogen flows assumption discussed above that formed the hydrocarbon deposits of the Dnieper part of the Dnieper-Donets Basin (DDB) over approximately 50 thousand years, it is possible to estimate the removal of H_2 in zones of transverse activated faults [Verkhovtsev, 2006] and outside them during the named period (Fig. 5).

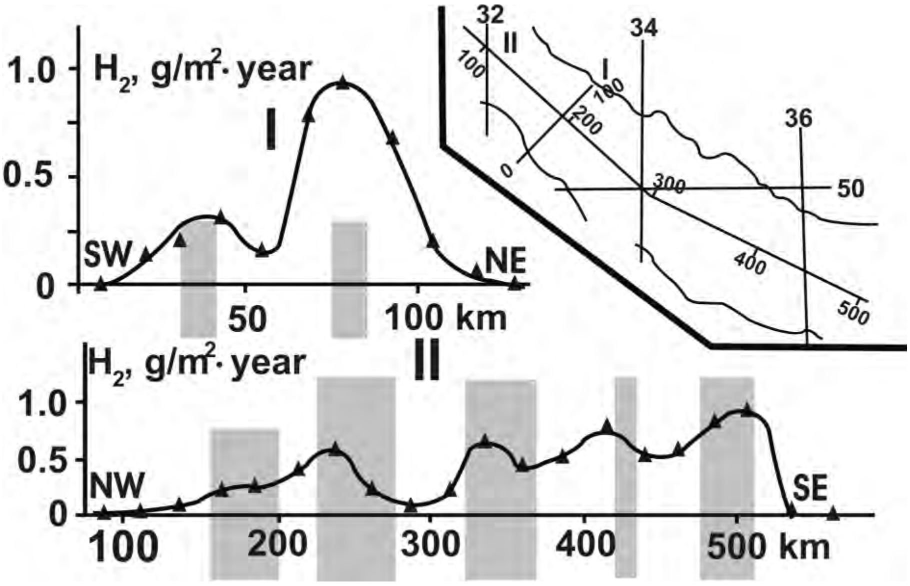

Fig. 5. Variations in the hydrogen flow that formed the DDB hydrocarbon deposits along and across the Dnieper basin [Gordienko, 2017, etc.]. Zones of activated faults are shown in gray. The inset shows the location of the profiles. Profile I shows the zones of marginal faults of the Riphean graben, the width of which is unknown.

Let us evaluate the energy potential of the "hydrogen pool" of the DDB. The heat of combustion of hydrogen (140 MJ/kg) and methane (50 MJ/kg) are correlated as 2.8:1. The mass of H in CH4 is 0.25 of the total mass of the gas. We get 70% of the energy from the oil and gas basin. Above deep faults, reserves will be about twice as large as between them.

In many regions of Ukraine, hydrogen concentrations in soil air, and water have been studied. The usual values are (including outside the zones of recent activation) $6\text{-}70\cdot10^{-5}$. But in the gases of several DDV hydrocarbon deposits, they reach 1-24%, which, according to the authors (Bagriy et al., 2019, Bagriy, 2020, etc.), is of industrial interest. Such a mixture of H_2 with methane (2-20%) is used in pipeline transportation of hydrogen to reduce its leakage. In the Donbass, hydrocarbon deposits of abiogenic nature are found only in the north, near the fault boundary of the region. Coalbed methane is common in the rest of its territory. There is no consumption of deep hydrogen to create methane, and its concentration in the gas near the fault intersected by the well reaches 60% [Murich et al., 1975].

However, it is widely believed that hydrogen in active fault zones is formed due to the grinding and crushing of rocks. In some publications, this explains even the flow of H_2 in volcanic areas [Encyclopedia..., 1999, etc.]. Changes in gas flow during periods of increased seismicity (Fig. 6A) may be partly related to this phenomenon. But seasonal variations most likely have a different nature, and the above-mentioned H_2 sources in the lower part of the crust of recent activation zones may well manifest themselves in flows through permeable faults. Hydrogen of this origin is not associated with rock crushing. Note that according to [Parnell et al., 2017], sedimentary clastic rocks from ancient crystalline formations of the basement contain more hydrogen than from young ones. I.e., it is not OG that is released during fracture.

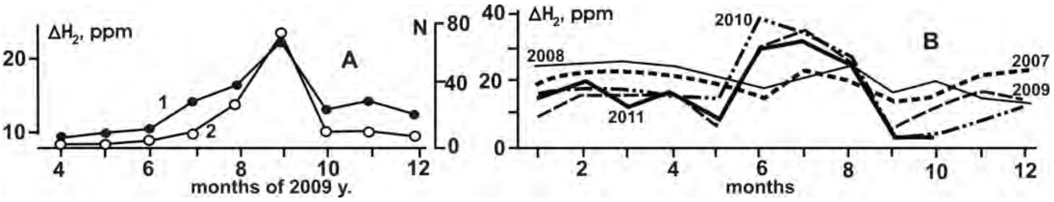

Fig. 6. Variation of hydrogen concentration: A - in excavation (1) and depending on the number of weak local earthquakes per month N (2); and B - average monthly concentrations in excavation in 2007-2011 [Nivin, 2013].

Despite the immense number of publications on the "hydrogen topic," there is very little specific information on the concentration of WH in continental crustal rocks. Most of the data cited consider the relative amounts of H_2 in reservoirs and underground gas flows, without regard to the proportion of space it occupies. The small selection below does not pretend to be any complete generalization of modern information but still gives an idea of the prevalence of hydrogen in crystalline rocks of felsic-medium and basic-ultrabasic (mainly alkaline) compositions [Vovk, 1982, Voitov, 1974, Ikorsky and al., 1992, Nivin, 2013, Petersilje et al., 1979, Parnell et al., 2017, Zgonnik, 2020, etc.]. Each of the two histograms is based on data from approximately 100-120 determinations, some of which are averages over several samples (Fig. 7).

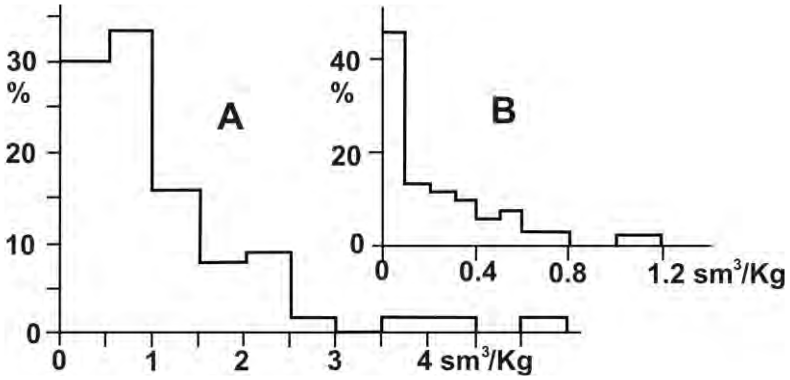

Fig.7. Hydrogen concentration in basic-ultrabasic (mainly alkaline) rocks (A) and acidic-intermediate crystalline and clastic rocks (B).

Using the example of the formations of an alkaline complex, which produces a lot of hydrogen and is well-studied, it is convenient to consider the origin of H_2. According to the authors [Gordienko, 2017 and others], fluids and gases in the mantle appear in noticeable quantities only in foci of partial melting, but the main source is crustal processes. The crustal origin of hydrocarbons is indicated, in particular, by the analysis of the contents of rare elements in hydrocarbon deposits [Rodkin et al., 2015]. The lack of evidence of heat and mass transfer from the lower mantle is argued in [Ivanov, 2010, etc.]. The results of long-term studies of the Kola alkaline rocks make it possible to trace the behavior of gases after the intrusion of magmas into the crust. "...in the fluid phase, in equilibrium with the crystallizing melt, the concentration of H_2 was higher than CH_4, but the main components of the fluid at magmatic temperatures were H_2O and CO_2." [Ikorsky et al, 1992, p. 28]. "It is assumed that the concentration of H_2 in the fluid phase, in equilibrium with the crystallizing melt, was higher. Moreover, judging by the isotopic composition of the noble gases, water could have been partially captured by the alkaline melt from the host rocks through the mechanism of transvaporization... Molecular hydrogen was also generated during the interaction of iron-containing minerals of aluminosilicate rocks with water, in particular, during the formation of minerals such as aegirine, magnetite, cancrinite, and zeolites" [Nivin, 2013, p. 212].

The difference between the two considered rock compositions (Fig. 7) is about an order of magnitude. Alkaline basites/ultrabasites are present on only 1% of the land area [Voitov, 1986, etc.], so the participation of such rocks in the generation of hydrogen in near-surface conditions is globally unnoticeable. But with increasing depth, their concentration in the section of the continental crust increases. On the Earth's surface, the difference in volumetric concentrations (lithosphere/atmosphere) reaches 2-3 orders of magnitude. In the AH balance described above, each of the compared components is studied separately; "forced pulling" of individual elements to match the effects of sources and sinks is used in a very limited manner and with special justification [Pieterse, 2012, etc.]. Therefore, we can conclude that the widespread flow of geological hydrogen into the atmosphere is not realized. It is local and tied to faults.

In the data shown in Figs. 4 and 5, it is quite possible to assume the almost complete absence of modern gas flow between faults (the influx of hydrogen into mine workings is most likely associated with their very appearance). Since hydrogen flows also correlate with longitudinal faults of the Dnieper basin (in particular, marginal faults of the Riphean and Hercynian grabens), the supply of H_2 and the formation of hydrocarbon deposits also occurred between transverse faults (Fig. 5).

An increase in hydrogen content with depth is likely only in connection with an increase in basicity (i.e., the emergence of new potential objects of serpentinization and bastitization), but only in zones of recent activation. Radiogenic heat generation decreases with depth, and metamorphic processes in the cold crust without intrusions of mantle magmas and the fluids they bring are inhibited. The widespread opinion about the increase of H_2 concentration with depth in the crust is, as a rule, poorly substantiated. To confirm this, examples are given of hydrogen contents of different origins, in different regions, at different depths, for which it is impossible to build a vertical distribution of the parameter [Zgonnik, 2020, etc.]. Information on hydrogen concentrations at different depths in the same area is very limited (Fig. 8) [Voitov, 1974, Ikorsky et al., 1999, Nivin, 2013, etc.], but still allows us to doubt the validity of this opinion.

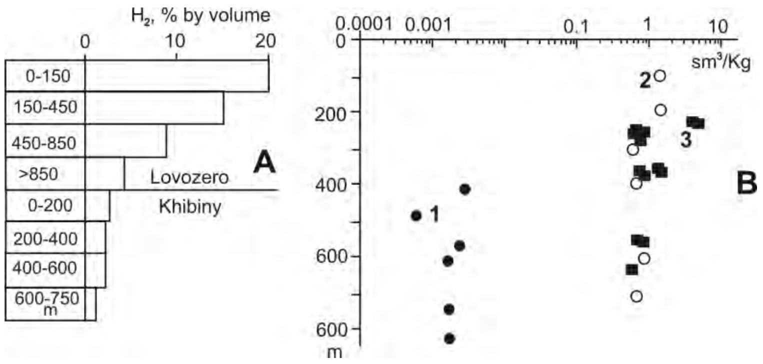

Fig. 8. Change in hydrogen concentration with depth.
Data for: 2, 3 – two districts of the Kola Peninsula (A) 1, 2, 3 – Krivoy Rog and two districts of the Kola Peninsula (B).

Figure 8A shows the relative changes in hydrogen volume with depth without indicating the absolute amount of gas at each depth. Such information does not, in principle, exclude an increase in H_2 concentration with immersion. However the data in Fig. 8B exclude such an interpretation. Thus, no other information can be found other than a rather conditioned vertical gradient in the Witwatersrand Formation (which is associated with an increase in the age of rocks with depth) [Lin et al., 2005]. At the achieved level of study, it can be assumed that significant discharge of WH occurs along faults. To assess the significance of the phenomenon, it makes sense to familiarize ourselves with the most striking example of such a process – volcanic hydrogen flows.

Volcanic hydrogen

To correctly interpret information about the flow of hydrogen from volcanoes, a thermal model of these objects, covering the crust and upper part of the mantle, is required. Lava outpourings and explosive ejections of material from the volcano occupy a relatively small part of its active period. The rest of the time, as a rule, it manifests itself over thousands of years as a field of fumaroles and hydrotherms. It is this state that the constructed thermal model corresponds to. Deviations from it are also noted (see below).

The problem was solved for a specific object - the Avacha volcano as part of the Eastern volcanic ridge in Kamchatka. It has been active since the late (possibly middle) Pleistocene. Attention to Avacha was attracted by the relatively recent eruption (1991) and the activation in 2001, which did not result in lava eruption, and the small distance from the cities of Petropavlovsk-Kamchatsky and Elizovo (about 30 km). The model basically repeats the one constructed in accordance with the theory in [Gontovaya et al. 2006], supplementing it with a crustal part (Fig. 9).

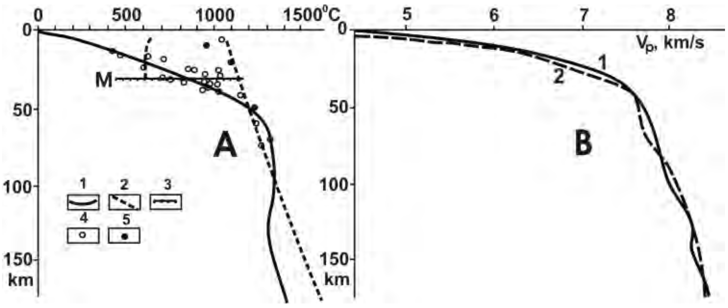

Fig. 9. Thermal (A) and velocity (B) models of the Avacha volcano area.
A: 1 – calculated temperature distribution, 2 – solidus temperatures of mantle and crustal (with amphibolite level of metamorphism) rocks, 3 – approximate position of the Moho section, 4, 5 – geothermometer data: 4 – in the Avacha area [Gontovaya et al., 2006 etc], 5 – in the area of basaltic volcanism of the Balkanids [Cvetković et al., 2012].
B: 1 – experimental velocity distribution [Nizkous et al., 2006, etc], 2 - calculated velocity model (by thermal model and process parameters according to the theory).

The data from geothermometers agree quite satisfactorily with the calculated T. The discrepancies average about 60^0C, which is comparable to the error of geothermometers. The maximum T values were excluded from the comparison (see below). The calculated velocities coincide with the experimental ones within ±0.065 km/s. This value is close to the experimental error [Gontovaya et al., 2006]. However, the constructed thermal model does not explain the maximum T values of geothermometers (supported by data on the Balkanides) and does not reflect the temperature distribution in the upper part of the section associated with fluid heat and mass transfer.

The constructed temperature distribution identifies layers of partial melting in the mantle in the depth interval of about 50-100 km and in the crust - at 20-30 km. Intrusions into the upper part of the crust of both mantle magmas and (mainly) contaminated by the influence of partly melted crustal rocks are inevitable. This is confirmed not only by volcanism itself but also by the detection of high T at shallow depths. They belong to samples of xenoliths carried out from crystallized magmas of previous eruptions from sources in the very bottom of the crust and/or the top of the mantle. The existence of deep channels under the fumarole field is confirmed by the results of studying microseisms (Fig. 10).

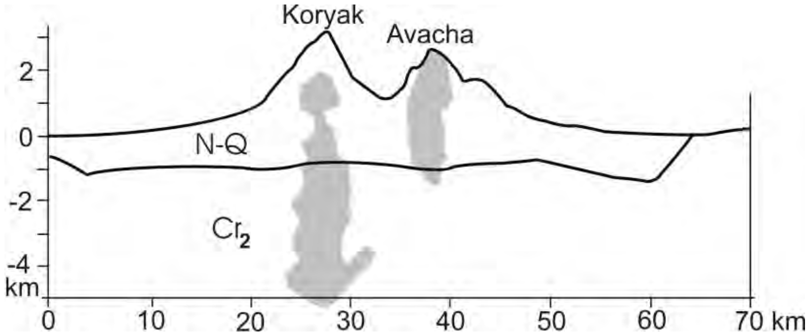

Fig. 10. Areas of hydrothermal circulation (according to the distribution of microearthquake hypocenters) beneath the Koryak and Avacha volcanoes [Kiryukhin et al., 2015].

Microseisms are presumably associated with fluctuations in magma caused by the periodicity of gas bubbles passing through it. On the Erebus volcano, pulsations of the lava lake surface and the gas content in the plume are recorded. [Moussallam et al., 2012]. Note, by the way, that according to the data obtained, there is no oxidation of hydrogen on the surface of the lake.
From the given data the depth of the lower boundary zone in the cell of hydrothermal circulation under Avacha and the fact of reaching the surface by fluids and gases follows. The thermal model of the cell was constructed [Gordienko, 2017, etc.]. Below about 4 km, the temperature distribution reflects convection in the magma chamber - an intrusion from the lower crustal layer. As we approach it, the calculated T agrees with the geothermometer data in Fig. 10. The ability to control the upper part of the model is created by the information on thermal fields in the volcanic regions of Japan

[Tamanyu et al., 2005, etc], where geothermometers and temperatures from wells to the entire depth of the fluid circulation were studied (Fig. 11).

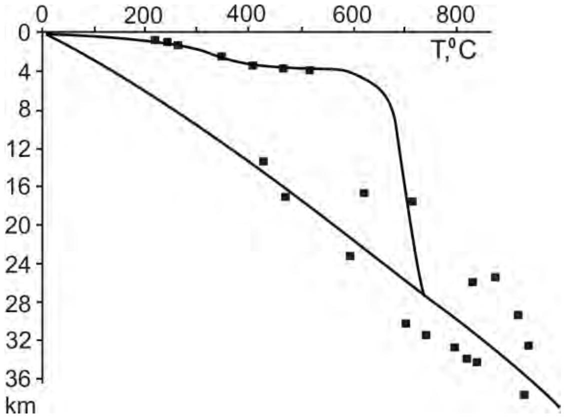

Fig. 11. Thermal model of the crust for the magma influx channel and the thermal water circulation zone under Avacha against the background of the model outside these elements (Fig. 9). Lines – calculated T, points – geothermometer data.

The possibility of feeding fluid-gas emissions in a wide temperature range is obvious, which is practically realized: the observed temperatures are 100-800^{0}C [Malik et al., 2017]. This is facilitated by the formation in 2001 (during the period of “limited explosive activity”) of a fault in a plug of solidified lava from a previous eruption. For some fumaroles, temperatures and the amount of hydrogen carried out were determined (Table 2).

Table 2. Temperatures (^{0}C) and hydrogen content (mmol/mol) in hydrotherms and fumaroles of Avacha [Malik et al., 2017]

T	H_2	T	H_2	T	H_2	T	H_2
98	0.033	390	0.39	500	0.38	595	1.73
100	0.12	400	0.21	500	0.72	602	2.34
100	0.22	401	0.24	570	2.40	605	1.92
101	0.03	416	0.11	584	1.6	608	202
102	0.027	420	0.23	584	1.47	610	1.47
335	0.32	473	0.50	590	1.62	626	1.66
381	0.21						

The data presented indicate a relationship between the molar concentration of H2 and the temperature of the ejected substance. On more representative material [Malik et al., 2017, Aiuppa et al., 2011 Encyclopedia..., 1999, Tassi et al., 2003, etc.] it is obvious (Fig. 12). Data for Avacha are presented here with four averages.

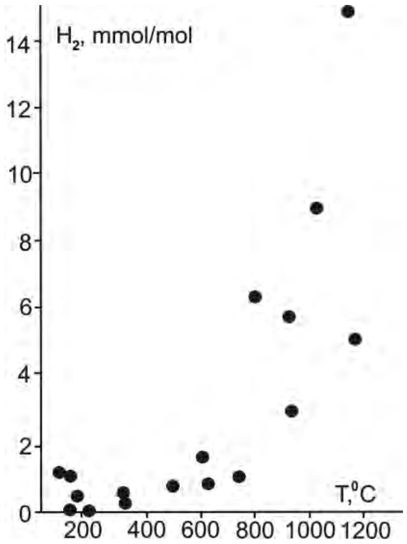

Fig. 12. Relationship between hydrogen concentration and gas outlet temperature.

The composition of gases separated from the magma can change as they rise to the surface. The main reaction (occurring between the main components of the mixture and the fastest), $SO_2 + 3H_2 \leftrightarrow H_2S + 2H_2O$, shifts to the right with increasing pressure and reduction in T. “Werner Giggenbach suggested that when hot gases separate from the magma and quickly rise to the surface, ... the process It does not work. However, at temperatures below approximately 350^{0}C... fumarolic gas is likely to escape from this high temperature state due to prolonged interaction... with the rocks surrounding the volcanic conduit. Many field observations correspond to Giggenbach’s predictions.” [Encyclodedia..., 1999, p. 805-806]. Subsequently, the estimated critical temperature was increased to approximately 550^{0}C [Aiuppa et al., 2011, etc.].

Thus, all the hydrogen produced by the magma chamber is fixed in high-temperature fumaroles. The weight concentration relative to all emission gases (including water vapor) is negligible. For example, in the case of Avacha, it is $1.8 \cdot 10^{-4}$, for the volcanoes of the Peruvian Andes it is $0.3 \cdot 10^{-4}$, for the Erebus volcano in Antarctica it is $1.05 \cdot 10^{-3}$.

The anhydrous part of hydrothermal gas flows essentially describes the same situation: the water vapor content is in the range of 50-98%, and the transition from volume to weight content reduces the mass values of H_2 concentration by an order of magnitude.

Table 3. Hydrogen content in dry hydrothermal gas [Encyclopedia..., 1999].

Country	H_2, vol. %	T, ^{0}C	Country	H_2, vol %	T, ^{0}C
Italy	2.1	240-250	Mexico	4.7	280-350
USA	19.9	240-250	New Zealand	0.8	240-260
USA	0.02	190-250	Honduras	0.06	170-220
Japan	19.4	430-880	Колумбия	3.09	350-430

France	0.16	70-140	Salvador	0.12	230-250
Mexico *	0-5.4	-			

* According to [Tassi et al., 2003].

Changes in molar concentrations of fumaroles' hydrogen with temperature in Fig. 12 show a trend, but hardly fully characterize the situation. There is still little material for analysis; volcanoes are located in zones with different endogenous regimes and receive magma of different compositions from different depths. It is clear only that in conditions of real operation of hydrotherms it is impossible to obtain gas with a high molar concentration of hydrogen. On average it is about 0.5-1.0 mmol/mol.

Information on the productivity of volcanic sources allows us to estimate the average value for a fumarole field or a system of volcanic craters at 1±0.6 tons of hydrogen per day [Malik et al., 2017, Aiuppa et al., 2011, Moussallam et al., 2012, 2017, etc.]. The number of volcanoes and thermal fields on land is estimated at about 500. This gives a total contribution to the earth's H_2 balance of about 0.15-0.20 Tg/year. The result does not differ noticeably from those obtained previously in [Warneck, 1988] – 0.2 Tg/year, in [Aiuppa et al., 2011] – 0.1 Tg/year, etc. Estimates are imprecise even for individual volcanoes. The Earth-wide result practically coincides with the contribution of MOR to the hydrogen balance of the atmosphere (see above).

Conclusions and implications

The considered manifestations and sources of hydrogen indicate the difficulty of studying its flows of geological origin. There is no method for identifying them outside of cases of fault concentration and, judging by the amount of interference, the prospects for its creation are vague. All available information indicates that the observed manifestations can be explained by the processes of radiolysis, metamorphic reactions, and melting effects in the upper mantle and crust. Fluxes for the Earth as a whole are small and do not play a noticeable role in the hydrogen balance of the atmosphere.

It is possible to estimate the probability of the formation of geological hydrogen deposits (except for the gas removal by hydrotherms discussed above).

V.A. Nivin admits the possibility of discovering areas with concentrations of hydrogen and methane in alkaline ultrabasite massifs that are of interest as deposits [Nivin, 2013]. Hydrogen production under these conditions will likely require technologies similar to those used in shale gas production. In crystalline rocks, this may be an excessively costly operation. Although it is possible that hydrogen export in such a case could be facilitated by active faulting, as occurred in a mine in the ophiolites of Albania (Truche et al., 2024)

Information on volcanoes and thermal fields shows that there are sources of H_2 capable of producing significant deposits. This is what happened during the formation of hydrocarbon deposits, but after hydrogen entered the composition of oil and gas.

The magmatic source of hydrogen and the fault transport path inevitably lead to high pressure in the storage reservoir. The calculation shows that at the usual level of abnormally high reservoir pressure (AHRP), hydrocarbon seepage through the screen can liquidate the field in the first thousands or hundreds of years. The second option is more likely since the calculations were carried out for permeability, which does not take into account the influence of local seismicity.

Thick layers of salt are considered to be the best screen for hydrocarbon deposits. In the Caspian basin, the thickness of such a screen (in the area where the calculations were carried out) was about a kilometer. Significant values of AHRP allowed fluids to seep through the salt strata with an intensity that changed the calculated heat flow by up to 20%. The experimental data are consistent with the calculated ones [Gordienko et al., 1986]. That is, even without increased permeability by seismicity in the RA zones, the existence of abiogenic hydrocarbon deposits is supported only by the supply of material from a deep source. The time of such recharge is limited by the crystallization of a shallow magma chamber - tens of thousands of years (of course, if there are no additional intrusions of magma).

However, the high permeability of real rocks to hydrogen will probably not allow its significant deposits to form. The experiment shows that when a core sample is exposed to hydrogen, the permeability increases by 2.4 times [Kravchenko et al., 2014]. In [Kravchenko et al., 2018], compacted core samples with very low air permeability (0.02–0.03 μm^2) were studied. None of the components of the model gas were filtered through the cores at a pressure drop of up to 2.5 MPa. When hydrogen is added to the mixture up to 5% by volume, only hydrogen is filtered, and with an increase in its concentration to 10 % by volume, other components begin to be filtered. Therefore, solving the problem of preserving hydrogen deposits is critically important for planning the search for its deposits.

Judging by the data on underground natural gas storage facilities, they are equipped only under screens with permeability in hundredths of millidarcies. However, “Calculations have shown that annual in-situ gas losses amount to about 1-1.5% of the active storage volume.” [Methodological..., 1996, p. 47]. For hydrogen with significantly higher permeability and lower viscosity, the depletion time of the deposit without constant replenishment will be tens of years. Let us also note that the storage facilities, naturally, do not have AHRP, which are inevitable during the formation of WH deposits of the nature considered.

In the USA, Great Britain, and Germany, salt mines are successfully used (i.e., without losses that make the enterprise unprofitable) for storing hydrogen; France has experience operating a storage facility in sedimentary rocks. It is planned to equip similar facilities of a larger size [Pfeiffer et al., 2017, Tarkowski, 2019, etc.]. In these cases, we are talking about shallow depths and time periods, but still, studying the filtration of gas from storage facilities will provide the basis for real estimates. For now, it remains to be stated that, according to experts, in hydrogen storage facilities, “The operating pressure is always lower (0.8 - 0.25) than the surrounding reservoir pressure. Salt rock is extremely gas-tight, with a theoretical leak rate of about 0.01% per year." [Crotogino at al., 2010, p. 43]. This prediction is also confirmed experimentally: at one of the salt storage facilities, a leak of 0.02% per year was established [Final..., 2017]. I.e.. the formation of hydrogen deposits under the salt screen is possible after the release of high pressure.

REFERENCES

Aiuppa, A., H. Shinohara, G. Tamburello, G. Giudice, M. Liuzzo, and R. Moretti. 2011. Hydrogen in the gas plume of an open‐vent volcano, Mount Etna, Italy, J. Geophys. Res., 116, B10204, doi:10.1029/2011JB008461.

Bagriy I.D. 2020. Interview to the site "Glavkom". 08/25/2020 https://glavcom.ua/new_energy/publications/dvichi-pisav-zelenskomu-yak-ukrajinski-vcheni-shukayut-klyuch-do-energetiki-maybutnogo-voden-701046.html (in Ukrainian)

Bagriy I.D. Kuzmenko S.A. 2019. Scientific substantiation of the spatial distribution and mapping of anomalous manifestations of hydrogen - the energy raw material of the XXI century. *Geol. zhurn.* 1. p. 59-77 https://doi.org/10.30836/igs.1025-6814.2019.1.159241 (in Russian)

Bjornstad, B., McKinley J., Stevens T., Rawson S., Fredrickson J. Generation of hydrogen gas as a result of drilling within the saturated zone. *Groundwater Monit. & Rem.,* 1994. 14, p.140– 147.

Bogdanov Yu.A.,. Gurvich E.G., Lein A.Yu., Sagalevich A.M., Novikov G.V., Peresypkin V.I., Bortnikov N.S., Vikentyev I.V. 2000. Hydrothermal ore occurrences of the Logachev and Rainbow fields (Mid-Atlantic Ridge) are a new type of hydrothermal deposits of oceanic rifts. *Russian Journal of Earth Sciences*. 2. 4 (in Russian).

Cannat, M., Fontaine, F. & Escartin, J. 2010. Serpentinization and associated hydrogen and methane fluxes at slow spreading ridges. *AGU Geophys. Monogr.* Ser. 188, p. 241–264.

Coveney R., Goebel E., Zeller E., 1987. Dreschhoff G. Serpentinization and the Origin of Hydrogen Gas in Kansas. *AAPG Bulletin.* 71(1) https://doi.org/10.1306/94886D3F-1704-11D7-8645000102C1865D

Crotogino F., Donadei S., Burger U., Landinger H. 2010. Large-Scale Hydrogen Underground Storage for Securing Future Energy Supplies. *Proceedings 18th World Hydrogen Energy Conference*. Book 4. 45p.

Cvetković V., Erić S., Radivojević M., Šarić K. 2012, Cognate clinopyroxene from Paleogene mantle xenolith-bearing basanite lavas (East Serbia, SE Europe): the role of dissolution of mantle orthopyroxene. *Mineralogy and Petrology*, V.106, 3-4, pp. 131-150.

Ehhalt D., Rohber F. 2009. The tropospheric cycle of H_2: a critical review. Tellus B: *Chemical and Physical Meteoroljgy.* V.61, 3. P. 500-535. https://doi.org/10.1111/j.1600-0889.2009.00416.x

Encyclopedia of volcanoes. H. Sigurdsson, B. Houghton, H. Rymer, J. Stix, S. McNutt. Academic Press. 1999. 1417p.

Environmental Health Criteria. Monographs Carbon monoxide (EHC 13, 1979, 1st edition), Carbon monoxide (EHC 213, 1999, 2nd edition) et al. World Health Organization. Geneva.

Essays on the degassing of the Earth. Ed. V.M. Shestopalov. Kiev: *Itek service.* 2018. 632p. (in Russian).

Final report for executing a study of the effects of hydrogen injection in natural gas networks for the Dutch underground strogates. *Netherlands Enterprise Agency*. Hague, Leipzig, Vienna. 2017. 66p.

Gilat A. L., Vol A. 2012. Degassing of primordial hydrogen and helium as the major energy source for internal terrestrial processes. *Geosci Front*. 3. P. 911–921. doi:10.1016/j.gsf.2012.03.009.

Gontovaya L.I., Gordienko V.V. 2006. Depth processes and geophysical models of the mantle of East Kamchatka and Kronotsky Bay. *Geology and Mineral Resources of the World Ocean*, 2. P. 107-121. (in Russian).

Gordienko V.V. 2019. Earth's crust of the World Ocean and strip anomalies of the magnetic field. *Geology and Minerals of the World Ocean* 4. P. 3-35 (in Russian).

Gordienko V.V., Zavgorodnaya O.V. 1986. Thermal field of the southeastern part of the Russian plate. *Geof. Journal*. 6. P. 3-11 (in Russian).

Gordienko V.V. 2017. Thermal processes, geodynamics, deposits. 285p. https://ivangord2000.wixsite.com/tectonos

Guélard J., Beaumont V., Rouchon V., Guyot F., Pillot D., Jézéquel D., Ader M., Newell D., Deville E. 2017. Natural H_2 in Kansas: deep or shallow origin? https://hal-ifp.archives-ouvertes.fr/hal-01582129/document

Holland H., 2002. Volcanic gases, black smokers, and the great oxidation event. *Geochimica et Cosmochimica Acta*. 6.: P. 3811–3826. doi:10.1016/S0016-7037(02)00950-X.

Holloway J., O'Day P. 2000. Production of CO_2 and H_2 by Diking-Eruptive Events at Mid-Ocean Ridges: Implications for Abiotic Organic Synthesis and Global Geochemical Cycling. *Int. Geol. Rev.* 42. P. 673–683. https://doi.org/10.1080/00206810009465105.

Ikorsky S.V., Nivin V.A., Pripachkin V.A 1992. Geochemistry of gases of endogenous formations. SPb .: *Science.* 179 p. (in Russian)

Ivanov A.V. 2010. Deep-level geodynamics: boundaries of process according to geochemical and petrological data. *Geodynamics and Tectonophysics*. 1. P. 87-102 (in Russian).

Jaehne B., Muennich K., Boesinger R., Dutzi A., Huber W., Libner P. 1987. On the parameters air-water gas exchange. J.G.R. 92. P. 1937-1949.

Kiryukhin A., Manukhin Y. , Fedotov S. , Lavrushin V. , Rychkova N., Ryabinin G. , Polyakov A., Voronin P. 2015. Geofluids of Avachinsky-Koryaksky Volcanogenic Basin, Kamchatka, Russia. Proceedings of World Geothermal Congress. Melbourne. 11p.

Konn C., Charlou J., Holm N., Mousis O. 2015. The Production of Methane, Hydrogen, and Organic Compounds in Ultramafic-Hosted Hydrothermal Vents of the Mid-Atlantic Ridge. *Astrobiology* 15(5). P. 381–399. doi: 10.1089/ast.2014.1198

Krayushkin V.A., Timurziev A.I., Shevchenko N.B. 2018. On the problem of the abiotic (non-biogenic) nature of oil and natural gas. *Materials of 6th KC.* P. 235-238. (in Russian).

Kravchenko O.V., Veligotsky D.A., Avramenko A.N., Khabibullin R.A. 2014. An improved technology of a complex influence on productive layers of oil and gas wells. *Eastern-European Journal of Enterprise Technologies*, *6*(5(72), 4–9. https://doi.org/10.15587/1729-4061.2014.29316

Kravchenko O.V., Suvorova I.G., Baranov I.A., Veligotsky D.A. 2018. Effect of hydrogen on flow and heat transfer in the "fracture-fluid" system. *Integrated technologies and energy saving*. 3. P. 35-46 (in Russian).

Lilley M., de Angelis M., Gordon L. 1982. CH_4, H_2, CO and N_2O in submarine hydrothermal vent waters. *Nature.* **300**, 48–50 https://doi.org/10.1038/300048a0

Lin L., Hall J., Lippmann-Pipke J., Ward J., Sherwood B., DeFlaun M., Rothmel R., Moser D., Gihring T., Mislowack B., Onstott T. 2005. Radiolytic H_2 in continental crust: Nuclear power for deep subsurface microbial communities. Geochem,, Geoph., Geosys. 6. P. 3-13. https://doi.org/10.1029/2004GC000907

Lippmann J., Stute M.,. Torgersen T., Moser D. P., Hall J.A.., Lin L., Borcsik M., Bellamy R. E. S. and Onstott T. C. 2003, Dating ultra-deep mine waters with noble gases and ^{36}Cl, Witwatersrand Basin, South Africa. Geochim. Cosmochim. Acta, 67. P. 4597-4619.

Makarenko G.F. 1997. Periodicity of basalts, biocrises, structural symmetry of the Earth. Moscow: *Geoinformmark.* 98 p. (in Russian).

Malik N.A., Zelenski M.E., Okrugin V.M. 2017. Temperature and gas composition of the Avachinsky volcano fumaroles (Kamchatka) in 2013–2016. *Bulletin of KRAUNZ. Earth sciences*. 1. Vol. 33. P. 21-32 (in Russian).

McMahon P., Chapelle F. 1991. Microbial Organic-Acid Production in Aquitard Sediments and Its Role in Aquifer Geochemistry. *Nature*. 349. P. 233-235. DOI: 10.1038/349233a0

Methodological guidelines for determining the technologically necessary irrecoverable gas losses during the creation and operation of gas storage facilities in porous formations. 1996. Moscow: *RAO Gazprom*. 50 p. (in Russian)

Moussallam Y., Tamburello G., Peters N., Apaza_F. 2017. Volcanic gas emissions and degassing dynamics at Ubinas and Sabancaya volcanoes; implications for the volatile budget of the central volcanic zone. *J. of Volc. and Geoth. Res.* 343, 1 P. 181-191. DOI: 10.1016/j.jvolgeores.2017.06.027

Murich A.T., Reznikov A.L., Abrazhevich E.V., 1975. Serdyukov V.V. The results of deep drilling in the central part of the Donbass. *Soviet geology.* 8. P.125-131 (in Russian).

Nizkous I.V., Kissling E., Sanina I.A., Gontovaya L.I. 2006. Velocity properties of the lithosphere of the transition zone of the ocean-continent in the Kamchatka region according to seismic tomography. *Physics of the Earth*. 4. P. 18-29 (in Russian).

Nivin V.A. 2013. Gas components in igneous rocks: geochemical, mineralogical and environmental aspects and consequences (for example, intrusive complexes of the Kola province). Dis. doc.geol.-min. sciences. *Apatity*. 353 p. (in Russian).

Novelli, P. C., Lang, P. M., Masarie, K. A., Hurst, D. F., Myers, R., Elkins *J.* 1999. Molecular hydrogen in the troposphere: global distribution and budget. *J. Geophys. Res.* 104. P. 30427– 30444.

Onstott T.C., Phelps T.J., Colwell F.S., Ringeberg D., White D.C., and Boone D.R. 1998. Observations pertaining to the origin and ecology of microorganisms recovered from the deep subsurface of Taylorsville basin, Virginia. *Geomicrobiol. J.,* 15. P. 353– 385.

Parnell J., Blamey N. 2017. Global hydrogen reservoirs in basement and basins. *Geochem. Transactions.* 18. 2. doi: 10.1186/s12932-017-0041-4

Petersilier I.A., Pripachkin V.A. 1979. Hydrogen, carbon, nitrogen, and helium in igneous rock gases. *Geochemistry.* 7. P. 1028-1034 (in Russian).

Polevanov V.P., Glazyev S.Yu. 2020. Searches for natural hydrogen deposits in Russia as a basis for integration into a new technological order. *Subsoil use. XXI century*. 4(57). P. 12-23 (in Russian).

Pfeiffer W., Beyer C., Bauer S. 2017. Hydrogen storage in a heterogeneous sandstone formation: dimensioning and induced hydraulic effects. *Petroleum Geoscience* 23 (3). P. 315–326. https://doi.org/10.1144/petgeo2016-050

Pieterse G.. 2012. Modelling the global tropospheric molecular hydrogen cycle. Netherlands. 198 p.

Pieterse, G., Krol, M. C., Batenburg, A. M., Steele, L. P., Krummel, P. B., Langenfelds, R. L., Röckmann, T . 2011. Global modelling of H_2 mixing ratios and isotopic compositions with the TM5 model. *Atmos. Chem. Phys.* 11(14). P. 7001–7026. doi:10.5194/acp–11–7001–2011.

Rodkin M.V. Punanova S.A. 2015. Assessment of the influence of crustal processes on the formation of microelement composition of caustobiolites. *Theses of 4 KR*. Moscow: CGE. (in Russian).

Romanova K. A huge supply of energy is under our feet. Focus. 04.12.20233 https://focus.ua/technologies/610479-ogromnyy-zapas-energii-u-nas-pod-nogami-vo-francii-nashli-krupneyshie-zalezhi-vodoroda (in Russian).

Savary, V., Pagel M. 1997. The effects of water radiolysis on local redox conditions in the Oklo, Gabon, natural fission reactors 10 and 16, *Geochim. et Cosmochim. Acta*, 61. P. 4479– 4494.

Sherwood Lollar B., Onstott T., Lacrampe-Couloume G., Ballentine C. J. 2014. The contribution of the Precambrian continental lithosphere to global H_2 production. *Nature* 516: P.379–382. doi:10.1038/nature14017.

Shumlyansky V.A., Demikhov Yu.N., Derevskaya E.I., Dudar T.V., Zelensky S.A., Zinchuk I.N., Ivantishina O.I., Kurilo M.V., Syngaevsky E .D. 1994. Geological and genetic model of the Bobrikovsky gold-polymetallic deposit. Geological Journal. 3. P. 95-106 (in Russian).

Sleep N., Bird D. 2007;. Niches of the pre-photosynthetic biosphere and geologic preservation of Earth's earliest ecology. *Geobiology* 5: p.101–117. doi:10.1111/j.1472-4669.2007.00105.x.

Tamanyu S., Fujimoto K. 2005, Hydrothermal and Heat Source Model for the Kakkonda Geothermal Field, Japan. *Proceedings World Geothermal Congress*. Antalya, P. 24-29.

Tarkowski R. 2019. Underground hydrogen storage: Characteristics and prospects. *Renewable and Sustainable Energy Reviews.* v. 105. P. 86-94.

Tassi F., Vaselli O., Capaccioni B., Macias J., Nencetti A., Montegrossi G., Magro G.. 2003. Chemical composition of fumarolic gases and springdischarges from El Chicho'n volcano, Mexico:causes and implications of the changes detected overthe period 1998^2000. *Journal of Volcanology and Geothermal restarches.* 123. P. 105-121. https://doi.org/10.1016/S0377-0273(03)00031-3

Truche L., Donze F.-V., Goskolli E. et al. A deep reservoir for hydrogen drives intense degassing in the Bulqizë ophiolite. *Science*. 2024. V. 383, NO. 6683. P. 618-621. DOI: 10.1126/science.adk9099

Tsilmak O.V. 2016. Mineralogical and geochemical model of the Bobrikivsky gold-bearing deposit. *Dis. Geological science.* LNU im. Ivan Franko. 217 p. (in Russian).

Verkhovtsev, V. G., 2006. The newest vertical movements of the earth's crust in Ukraine, their relationship with the linear and ring geostructures. Energy of the Earth, its geological and ecological manifestation, scientific and technological use. "TECHNOLOGICAL AND ENVIRONMENTAL SAFETY AND CIVIL PROTECTION" No. 6. Kyiv: Kyiv University Publishing and Printing Centre, P. 129-137 (in Ukrainian).

Voitov G.I. 1971. On the chemical composition of gases in Krivoy Rog. *Geochemistry.* 11. P. 1324-1331 (in Russian).

Voitov G.I. 1974. To assess the intensity of gas exchange on shields (on the example of the Ukrainian shield). *Geological journal*. 2. P.68-82 (in Russian).

Voitov G.I. 1975. Gas breathing of the Earth. *Nature.* 3. P.91-98 (in Russian).

Voitov G.I. 1986. Chemistry and scale of the modern flow of natural gases in various geostructural zones of the Earth. *Journal All chem. Society named after D I Mendeleev*. 31. P. 533–556. (in Russian).

Vovk I.F. 1982. Brines of the crystalline foundation of shields. Kyiv*: Naukova Dumka.* 163 p. (in Russian).

Vovk, I.F. 1987. Radiolytic salt enrichment and brine in the crystalline basement of the east European platform, in Saline Water and Gases in Crystalline Rocks, *Geol. Assoc. Can. Spec. Pap.,* 33, P.197 – 210.

Xiao, X., Prinn, R. G., Simmonds, P. G., Steele, L. P., Novelli, P. 2007. Optimal estimation of the soil uptake of molecular hydrogen from the Advanced Global Atmospheric Gases Experiments and other measurements. *J. Geophys. Res.* 112, D07303, doi:DOI: 10.1029/2006JD007241.

Warneck, P. 1988. Chemistry of the Natural Atmosphere. *International Geophysics Ser*ies, vol. 41. 757 p.

Welhan J.A., Craig H. 1979. Methane and hydrogen in East Pacific rise hydrothermal fluids. *Geophys. Res. Letters.* 6, 11. P. 829-831. **https://doi.org/10.1029/GL006i011p00829**

Worman S.L, Pratson L.F., Karson J.A., Klein E.M. 2016. Global rate and distribution of H_2 gas produced by serpentinization within oceanic lithosphere. *Geophys Res. Lett.* 43. P. 6435–6443. https://doi.org/10.1002/2016GL069066

Zgonnik V. 2020. The occurrence and geoscience of natural hydrogen: A comprehensive review. *Journal Pre-proof. Earth-Science Reviews*. 203 https://doi.org/10.1016/j.earscirev.2020.103140

Why does Plate Tectonics Continue to Mislead the Geosciences?

Dr James Maxlow
Retired Professional Geoscientist, Australia
james.maxlow@bigpond.com
Free PDF copy of current book: complimentary book

MAXLOW J. 2018. Beyond Plate Tectonics: Unsettling Settled Science. Aracne Editrice.

By far the biggest, albeit unknown problem facing both the geosciences and industry today is appreciating that Plate Tectonics may well be better suited to an increasing radius Earth scenario.

Abstract

While Plate Tectonics continues to dominate the geosciences, modern global geological and geographical observational data tell a completely different story. Since the 1960s, this observational data has traditionally been gathered in support of Plate Tectonic studies and as such, until now, has rarely been looked at other than from a conventional Plate Tectonic perspective. This conventional perspective insists that the origin of the continents and oceans is a random, non-predictable, and sometimes catastrophic process—a process that is understood by very few and remains unchallenged by most. In contrast to what we are currently led to believe, this global observational data is instead telling a completely different story about the origin of Earth's continents and oceans; one that shows a very simple, evolving, predictable, easily understood, and holistic process involving a progressively changing Earth surface area and surface curvature through time. It is suggested that now is the time for science to seriously consider that Plate Tectonics may be better suited to an increasing radius Earth mechanism, rather than continuing to constrain the geological, geographical, and biogeographical observational data to an outdated, blinkered, static radius Earth premise.

Keywords: Expansion Tectonics, Plate Tectonics, Global Tectonics.

Introduction

After over 50 years of research and development, the question never arises as to why Plate Tectonists continue to lead the geosciences astray with outdated assumptions and premises about Earth parameters while modern global geological and geographical observational data tell a completely different story? Similarly, the question never arises as to why do we continue to be constrained to a mind-set that insists that Earth size has remained constant over time, without allowing science to further test or challenge this assumption? Why, because scientists are complacently comfortable with unconscientiously constraining this modern observational data to outdated assumptions and premises; hence they do not need to further test these assumptions and constraints.

Today, the theory of Plate Tectonics is the predominate paradigm in geology that is used to explain a wide variety of global observations, such as the movement of continents, formation of mountains, distribution of volcanoes, and magnetic apparent-polar-wander, to name but a few. However, as noted by Trümpy (2000), *"The theory of plate tectonics was developed primarily by geophysicists at sea, who took little account of the Alpine* [geological] *evidence."* These geophysicists, and similarly oceanographers, proposed a conceptual framework to explain these new observations based on a limited amount of global evidence available during the mid-1960s.

Since first established in the 1960s, it is unfortunate that plate theory has continued to be driven primarily by the mathematical sciences at the expense of geology, geography, and biogeography. If allowed to do so, modern geological and geographical evidence clearly demonstrates that these founding scientists may have made a poorly informed decision to use the long-since rejected Continental Drift theory as the driving mechanism behind the newly observed crustal plate motions on a static radius Earth model. In doing so, these scientists then substantiated their decision by adopting palaeomagnetics as the basis for plate assemblage studies, as well as rejecting and discrediting the alternative theory that this plate motion and assemblage may instead be the result of an increase in Earth radius and surface area over time.

The evidences presented by palaeomagnetic, and similarly space geodetic measurement techniques are, however, derived mathematical entities and the established formulae used are constrained to, and must adhere to, a number of applied constancy assumptions prior to calculation. If these assumptions are varied or changed, as modern observational data suggests they should, then the outcomes of the mathematics will also change. If these assumptions are found to be lacking, or at least partially inadequate, then true science must insist that they be subject to the rigors of scientific scrutiny and challenged as required.

Global Geological Mapping

Subsequent to adoption of plate theory during the 1960s, an extensive program of seafloor magnetic and bathymetric-based geological mapping, accompanied by age dating, was carried out throughout all of the oceans during the 1950s to late 1980s. This geological mapping program was initiated and designed to quantify the distribution of all crustal plates, and hence further quantify Plate Tectonics. Since its completion in 1990 (CGMW & UNESCO, 1990) (Figure 1) this geological mapping, however, has been underutilised in plate modelling studies, and plays very little to no part in constraining past plate assemblages.

What is not being promoted in the geosciences is that the outcomes of this mapping highlights the growth history of each of the seafloor plates over time (Figure 1). This growth history preserves the precise location of all mid-ocean-ridge plate boundaries since the early-Jurassic, and hence is in a readily available format to geologically constrain and assemble each of the plates during this time period.

Prior to completion of the Geological Map of the World in 1990, assembling the ancient plates using a static radius Earth plate tectonic premise can only be done if you ignore the geological and geographical evidence from the oceans and resort to cartoon sketches. In contrast, by utilising this growth history, and removing the historical assumption about Earth radius, the published seafloor mapping shown on the Geological Map of the World can be readily used to reverse engineer geology back in time in order to accurately constrain the location and assemblage of all crustal plates, but only on a smaller radius Earth.

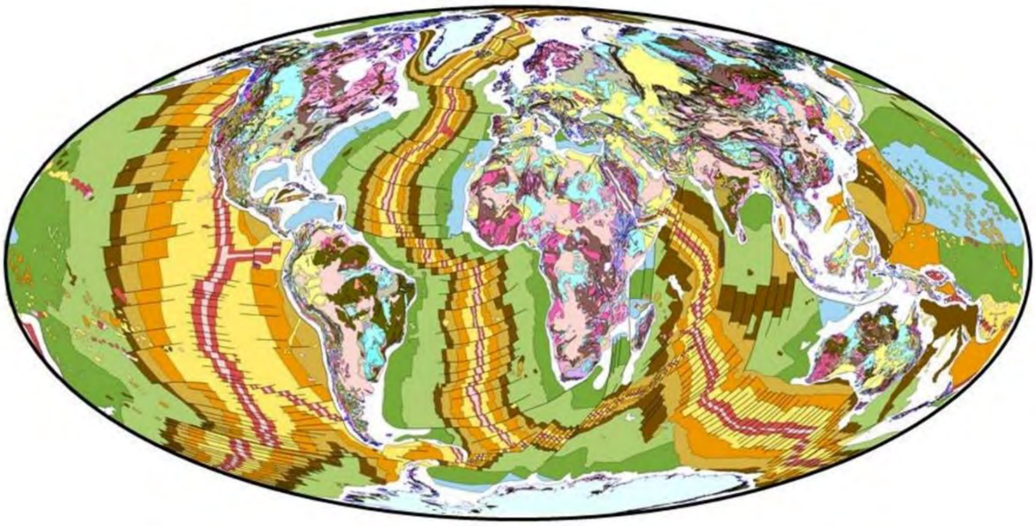

Fig 1. *Geological Map of the World. (Digitized with permission from the Commission for the Geological Map of the World and UNESCO, 1990, shown in Mollweide Projection).*

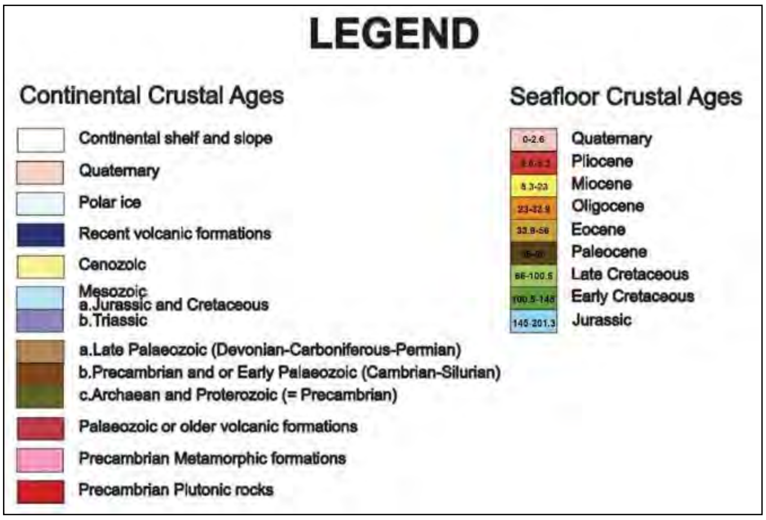

Fig 2. *Geological timescale of the continental and seafloor crustal ages as shown in Figure 1. Seafloor crustal ages are in millions of years before the present-day.*

This reverse engineering and assemblage of seafloor crustal plates (Figure 3) is shown to extend for 200 million years back in time to the early-Triassic Period, and demonstrates the viability and uniqueness of this post-Triassic modelling tool. These resulting plate assemblages contrast strongly with conventional, Continental Drift-based Plate Tectonic reconstructions for the same time interval where assemblage of crustal plates is primarily based on palaeomagnetic apparent-polar-wander, with accompanying poorly constrained multiple plate-fit options to contend with. The uniqueness of small Earth assemblages also contrasts strongly with the conventional Plate Tectonic requirement to arbitrarily fragment continents in order to comply with the seafloor mapping data. It also contrasts with the requirement to dispose of large areas of inferred pre-existing crust beneath subduction zones in order to maintain a constant surface area premise. By removing the implied assumptions about Earth radius and surface area, most of the problems and inconsistencies confronting Plate Tctonics then disappear.

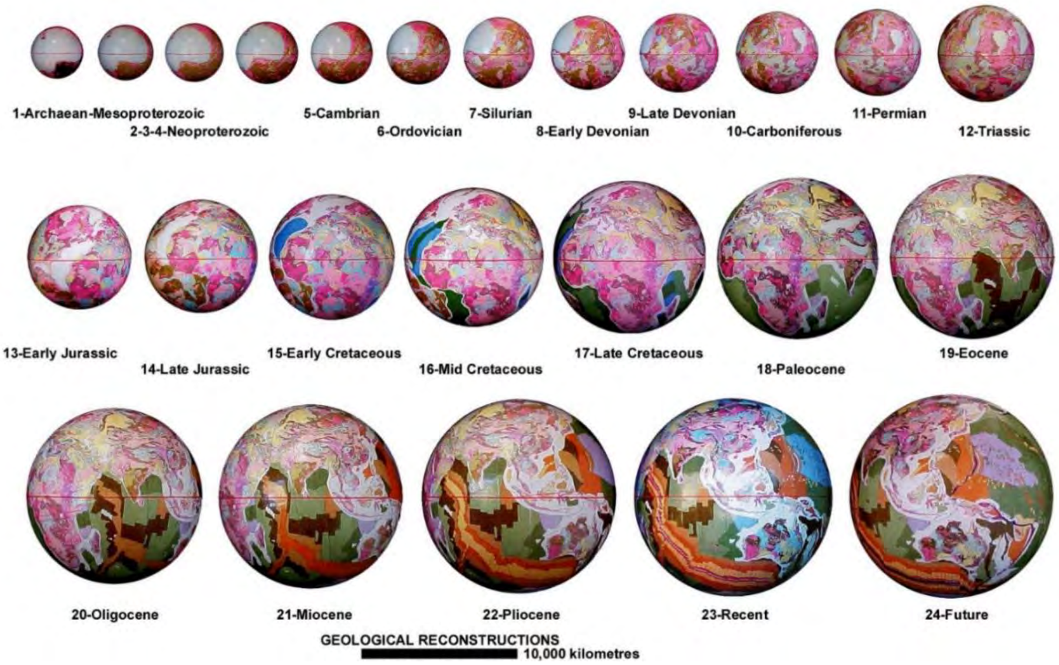

Fig 3. *Spherical Archaean to future small Earth geological models. Models range in age from the early-Archaean to present-day, plus one model projected 5 million years into the future.*

Quantification of an increasing radius Plate Tectonic Earth process back to the early-Archaean requires an extension of the fundamental post-Triassic cumulative seafloor crustal methodology to include continental crusts. Continental crust can be reconstructed on pre-Triassic small Earth models by considering the primary crustal elements cratons, orogens, and basins. In order to assemble the continental plates and construct models, further consideration must be given to an increase in Earth surface area occurring as a result of crustal stretching and extension within an established network of continental sedimentary basins.

Moving back to Precambrian times, this crustal extension is progressively restored to a pre-extension, pre-stretching, or pre-rift configuration by simply removing young sedimentary and intruded magmatic rocks, and reducing the surface areas of each of the sedimentary basins in turn, consistent with the empirical age-constrained data shown on the Geological Map of the World (Figure 1). During this restoration process, the spacial integrity of all existing ancient cratons and orogens is retained until restoration to a pre-basin, or pre-orogenic configuration is required. By removing all basin sediments and magmatic rocks, as well as progressively reducing the surface areas of the sedimentary basins in turn, an ancient primordial Earth is readily achieved comprising an assemblage of the most ancient Archaean cratons and Proterozoic basement rocks; all other rocks, minerals, and elements are simply returned to their places of origin.

From the outcomes of this empirical small Earth modelling exercise, it is concluded that geological crustal modelling studies more than adequately quantify the validity of an increasing Earth radius Plate Tectonic process. The unique assemblage of all continental and seafloor crustal fragments on small Earth models demonstrates conclusively that an increasing radius Earth, extending for 4,000 million years to the beginning of Earth's geological past, is indeed viable. What the full range of Archaean to present-day small Earth models also demonstrates is that, rather than being a random, arbitrary, amalgamation-dispersal-amalgamation cyclical crustal forming process, as we are currently led to believe, crustal development on an increasing radius Earth model is instead shown to be a simple, evolving, and highly predictable crustal process.

Applying this small Earth geological modelling evidence to palaeomagnetics (Figure 4) shows that all ancient magnetic poles cluster as unique, diametrically opposed north and south poles—as they should—and plotted palaeolatitude measurements coincide with, and quantify, predicted climate zones on each small Earth model constructed. Similarly, additional geographical and biogeographical information aptly quantify the location of these ancient magnetic poles, equators, and climate zones. This point cannot be over emphasized: diametrically opposed magnetic poles and an accurately positioned equator located midway between each pole cannot be achieved using the current Plate Tectonics paradigm. Once again, many of the ad-hoc problems and inconsistencies used to explain Plate Tectonics then simply disappear.

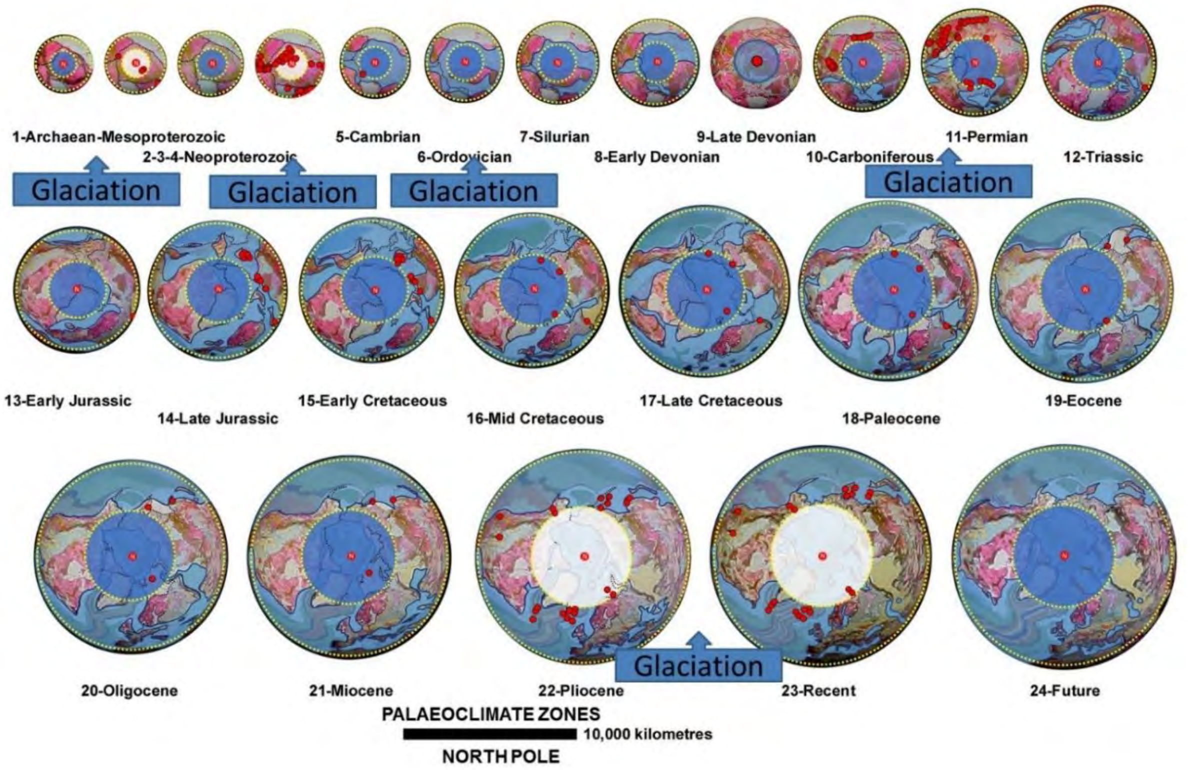

Fig 4. *Locations of ancient North Polar Regions shaded blue on small Earth models. Glacial events are highlighted, the presence of known ice-sheets are shaded white, glacigenic formations are shown as red dots, and ancient seas and modern oceans are shaded pale blue.*

When published coastal geography is plotted on each model (Figure 5) it is shown that large, conventional, Panthalassa, Iapetus, and Tethys Oceans are not required on a smaller radius Earth. Instead, this same coastal geography defines the presence of more restricted continental Panthalassa, Iapetus, and Tethys Seas, which represent precursors to the modern Pacific and Atlantic Oceans and emergent Eurasian continents respectively. From this geography, the coastal outlines and emergent land surfaces further quantify the location of the ancient Rodinia, Gondwana, and Pangaea supercontinents and smaller sub-continents. This coastal geography demonstrates an evolutionary progression and development of each of the ancient seas and supercontinents throughout Earth history, which is shown to be intimately related to changes in sea-level, changes to the outlines of continental sedimentary basins, changes incurred during crustal mobility, and changes to sea-levels once the modern oceans opened to the present-day.

The timing and development of these ancient continental seas and supercontinents, along with formation of the modern continents and oceans, provides an ideal setting for the primitive Precambrian microbe's effectiveness as nurseries of evolution, and to markedly drive subsequent evolutionary change in all life forms. On each of the small Earth models created, warm sea waters during much of the Palaeozoic extended from equatorial regions through to the North Polar Region, allowing newly evolved species to readily colonise and populate throughout each of the interconnected ancient Tethys, Iapetus, and Panthalassa seaways. This distribution of warm seas also limited the presence of a polar ice cap in the North Polar Region, and restricted the presence of ice to the exposed Gondwanan South Polar Region throughout much of that time.

Modelling studies also show that, during the early-Palaeozoic to present-day, there have been a number of drastic and prolonged changes to sea-levels which coincide with known extinction events. On these models, major changes in sea-levels are shown to occur as a result of separation or merging of previous ancient continental seas, as well as onset of geosynclinal activity and orogenesis, breakup of the ancient supercontinents, opening of the modern oceans, and draining of the ancient continental seas. Depending on the severity of these events, sea-level changes may have also adversely affected regional to global-scale climate, as well as ocean-water circulation patterns, species habitats, and the type and location of sedimentary deposition.

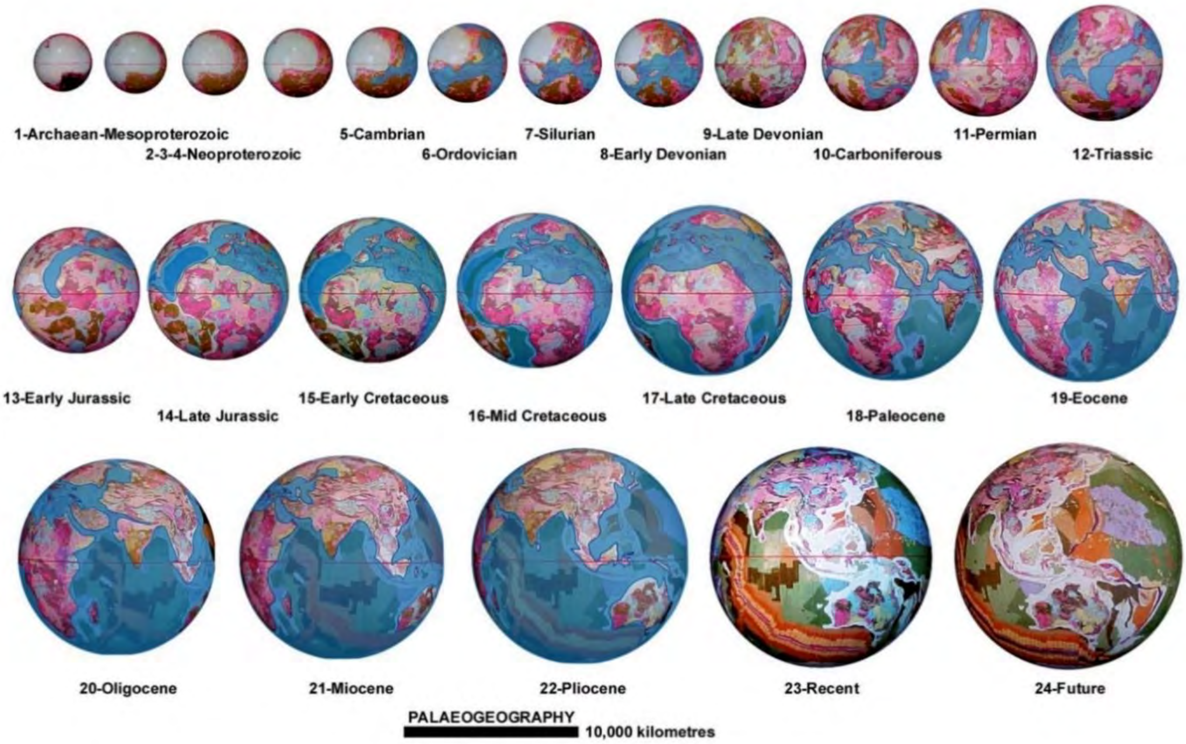

Fig 5. *Shoreline palaeogeography on Archaean to present-day small Earth models. The ancient shorelines are shown as blue lines and the ancient seas and modern oceans are shaded blue. Each image advances 15 degrees longitude throughout the sequence to show a broad coverage of palaeogeographic development. Note: there are no published data available for the late-Devonian model or models prior to the Cambrian Period.*

Modelling metallogenic data and mineralisation settings on small Earth models shows that data and mineral settings are essentially the same as those identified within conventional studies. The difference being that, on an increasing radius Earth, prior to the early-Triassic Period, all continental crusts were assembled together on a smaller radius supercontinental Earth. This enables pre-Triassic metallogenic provinces from otherwise remote locations to be assembled together as unique, inter-related provinces. The assemblage of continents and crustal elements on small Earth models then provides a means to investigate the spatial and temporal distribution of metals across adjoining continents and crustal regimes. Recognition and understanding of past metal distributions on the present-day Earth then potentially enables mineral search and generic relationships to be extended well beyond their known type localities.

Modelling the distribution of all fossil fuels (Figure 6) highlights the global interrelationships of resources coinciding with the distribution of Palaeozoic continental seas and low-lying terrestrial environments, plus post-Permian breakup of Pangaea to form the modern continents. The transition from deposition of oil and gas shale to coal to petroleum and natural gas is found to be consistent with the various periods of maximum to minimum sea level changes occurring during periods of marine transgression and regression, in particular after regression of the continental seas during late-Palaeozoic times, leading to crustal breakup and opening of the modern oceans.

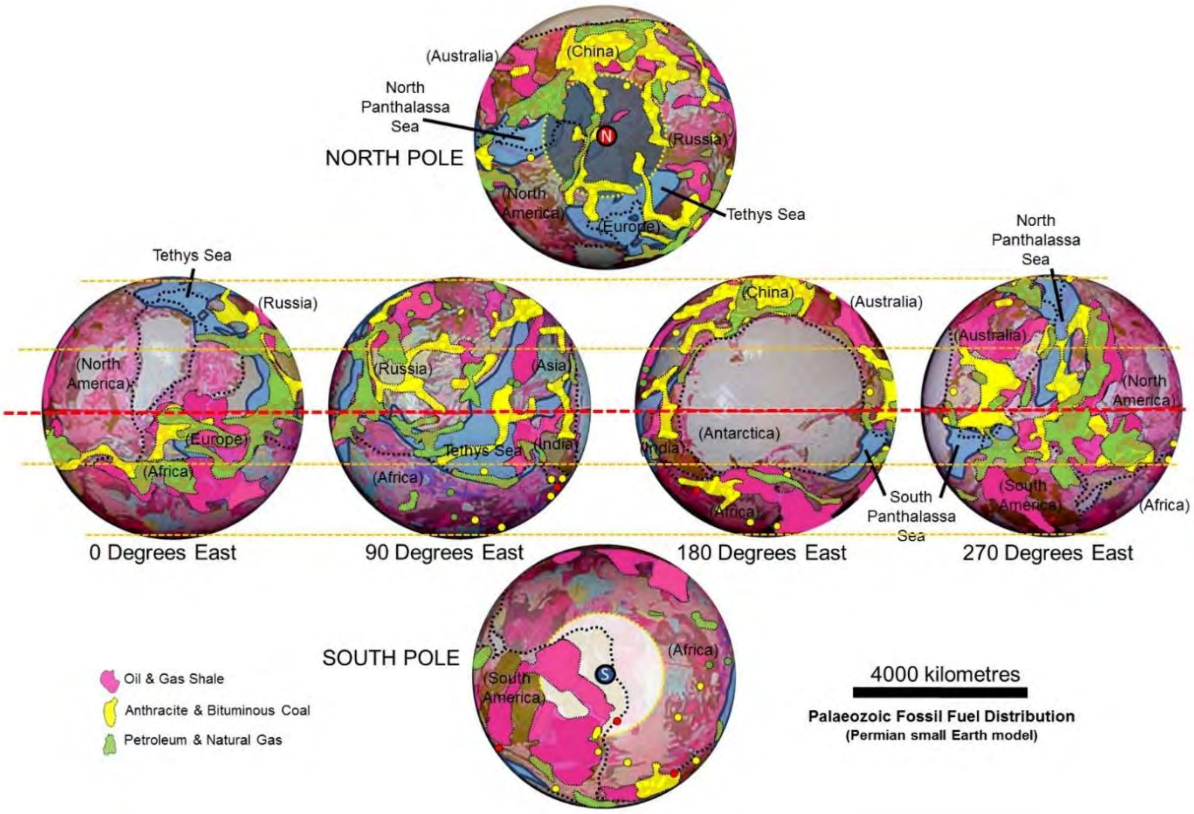

Fig 6. *Compilation of oil and gas shale (magenta), coal (yellow), and petroleum and natural gas (green) distributions shown on the Permian model.*

The Fundamental Problem

However, the fundamental problem that scientists and the general public continue to have is comprehending where did the huge volume of material making up the seafloor crusts and underlying mantle go to when moving back in time in order to reassemble the continents? And, more importantly, where does this huge volume of material come from when moving forward in time?

In year 2000 four identical Cluster II satellites were launched by the European Space Agency. These satellites were launched to study the impact of the Sun's activity on the near-Earth space environment by flying in formation to gather data around Earth. For the first time in space history this mission was able to collect three-dimensional information about how the solar wind interacts with the magnetosphere, how it affects near-Earth space, and how the Earth reacts with the charged particles within the solar wind. This new information, and related discoveries, were considered by the European Space Agency's project scientists to be of great importance because they showed how the Earth's magnetosphere can be readily penetrated by solar particles.

The Earth's magnetosphere is shown to be full of trapped plasma, comprising charged electron and proton particles, originating from the solar wind as it passes the Earth. This flow of plasma into the magnetosphere increases with increase in solar wind density and speed, as well as increases in turbulence in the solar wind. In addition to penetrating the magnetosphere, it was also shown that the plasma travels down along the Earth's magnetic field lines within the auroral zones, entering the Earth at each of the poles. This European study suggested to the scientists that penetration of plasma may be a lot more common than was previously known, and possibly represents a means for the constant flow of charged electrons and protons into the Earth. The question we must ask and seriously take note of is, what happens to these particles—the building blocks of all matter on Earth—once they enter the Earth?

A causal mechanism for an increase in Earth mass and radius over time is speculated to be solar particles entering the Earth at the poles and recombining as new matter, most likely within the 200 to 300 kilometres thick D” region, located at the core-mantle boundary. This matter generation process represents a basis for formation of all new and existing elements and mineral species present on Earth. It is further speculated that formation of new matter within the Earth gives rise to an increase in mass and volume of the mantle over time. Increase in mantle volume is then transferred to the outer crust as continental crustal extension which is currently seen and preserved as extension along all mid-ocean-rift zones. Surface crustal extension within the mid-ocean-rift zones is further accompanied by intrusion of new basaltic lava and expulsion of new sea water and atmospheric gases (Figure 7).

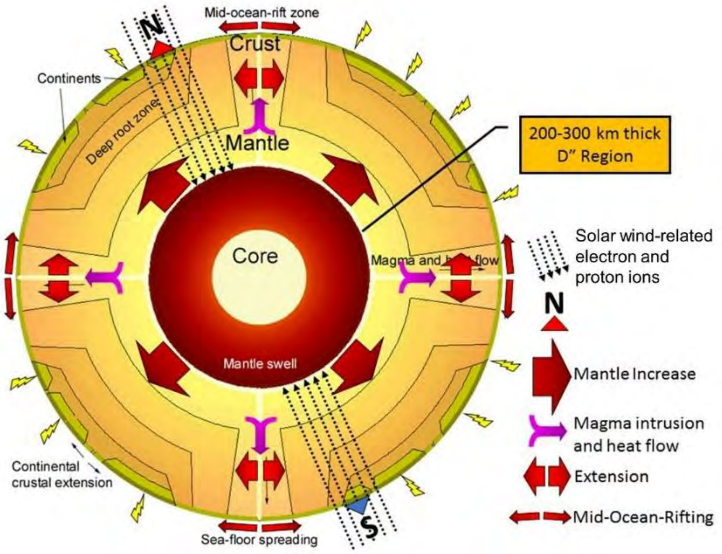

Fig- 7. *A schematic cross-section of the present-day Earth highlighting the influence of charged electrons and protons entering the Earth resulting in increase in mass and radius over time.*

In summary

It is unfortunate that modern, mathematical-based, observational data gathering so firmly constrains Plate Tectonic thinking that scientists are now oblivious to any suggestion that there are viable alternatives to interpretation and utilisation of this, and all other global observational data. Modern global observational data, in particular the geological, geographical, and biogeographical data, are telling a completely different story to what the mathematical-based sciences currently lead us to believe.

This modern data tells us that there is definitely something seriously amiss with continuing to constrain Earth radius to a constant value. The Expanding Earth theory days are long gone but, are we still justified in continuing to think that accurate modelling of this data, as briefly presented here, is mere coincidence. Now is the time for science to seriously consider that Plate Tectonics may be better suited to an increasing radius Earth scenario, rather than continuing to constrain the geological and geographical observational data to an outdated, blinkered, static radius Earth assumption?

References

CGMW & UNESCO 1990. Geological Map of the World. Commission for the Geological Map of the World, Paris.

MAXLOW J. 2018. Beyond Plate Tectonics: Unsettling Settled Science. Aracne Editrice.

TRÜMPY R. 2001. Why Plate Tectonics was not invented in the Alps. International Journal of Earth Sciences. (Geol Rundsch) 90:477-483.

Earthquakes and AI: The Proposal of a New Research Model

Daniele Cataldi[1-2], Gabriele Cataldi[1], Valentino Straser[3]

(1) Radio Emissions Project (I). ltpaobserverproject@gmail.com
(2) LTPA Observer Project (I) - daniele77c@hotmail.it
(3) Department of Science and Environment UPKL Brussel (B). valentino.straser@gmail.com

Abstract

Artificial Intelligences (AIs) have begun to emerge significantly about a decade ago, with rapid advancements in recent years. However, the roots of AI research trace back to the 1950s, with incremental developments along the way. The real explosion of interest and practical applications took hold with the advent of big data, increased computational power, and improvements in machine learning algorithms, especially since the early 2010s. In 2023, the Radio Emissions Project experimented with AIs to enhance the computing capability and data analysis of seismic data related to the research on seismic precursors. This study aims to understand whether AIs are capable of producing useful information for the comprehension of seismogenic mechanisms and interpreting data to perform short-term predictions on Italian seismic activity.

Keywords: AI, Seismic Precursors, Earthquake in Italy.

1 - Introduction

The evolution of Artificial Intelligence (AI) spans decades and is characterized by significant advances, challenges, and periods of stagnation known as "AI winters." This journey has led to revolutionary developments that have transformed the technological field and our way of interacting with machines.

The official history of AI begins in the 1950s when the concept of "intelligent machines" started to take shape through the work of pioneers like Alan Turing. The year 1956 is often cited as the birth year of AI, marked by the Dartmouth Summer Research Project, where the term "Artificial Intelligence" was coined, and researchers shared the vision that machine intelligence could be simulated through symbolic manipulation.

In the 1960s and '70s, AI experienced a period of optimism and progress with the development of expert systems and the promise to revolutionize various sectors. However, the complexity of mimicking human intelligence was underestimated, leading to the first "AI winters," periods during which funding and interest in AI drastically decreased due to unmet expectations.

Despite these obstacles, AI continued to evolve in the '80s and '90s, thanks to advances in machine learning, neural networks, and natural language processing (NLP). These years saw the development of systems capable of performing specific tasks with increasing precision, such as the IBM Deep Blue supercomputer defeating chess champion Garry Kasparov in 1997.

The arrival of the 21st century marked an era of data explosion and significant improvements in computing power, enabling notable advancements in deep learning. These developments led to the creation of AI systems capable of surpassing human performance in specific tasks, such as image recognition, automatic translation, and the game of Go.

The introduction of the Generative Pre-trained Transformer (GPT) by OpenAI in 2018 and the subsequent debut of ChatGPT were key milestones, demonstrating language generation capabilities and advanced conversational interaction. These developments have opened new frontiers for AI, showcasing its potential in enhancing efficiency and creating new modes of interaction between humans and machines.

AI continues to be a rapidly evolving field, with profound implications for the future of work, ethics, and society. Ongoing developments in machine learning, robotics, and brain-computer interfaces promise to take AI in new directions, continually challenging our expectations of what machines can do.

In 2022, the Radio Emissions Project began to consider the use of AI in a scientific context, leveraging the capabilities of Artificial Intelligence to gather seismic monitoring data and tackle new experimental projects that could aid researchers in understanding seismogenic phenomena.

The AIs made available to amateur research did not yet possess advanced functions capable of performing certain calculations or supporting researchers in a research context, but this problem was overcome in mid-2023 with the introduction of new functions made available to users worldwide.

Thus, in February 2024, following some successful seismic prediction trials, the Radio Emissions Project processed predictive data indicating that earthquakes were expected to occur in specific areas of Italy, based on monitoring data from the National Institute of Geophysics and Volcanology.

On February 4, 2024, AI was provided with monitoring data related to earthquakes that occurred in Italy in the last 7 days, from January 29, 2024, to February 4, 2024. During this time, AI was asked to retrieve data from the INGV archive and compile a list of earthquakes, sorting them by Italian province.

2 - Method and Data

For the creation of the map of the probabilistic imminence of earthquake occurrence in Italy, real-time accessible data on the INGV website (www.ingv.it) were utilized. Therefore, all earthquakes of magnitude M2+ that occurred on Italian territory were divided by each Italian region.

In this manner, AI created a ranking among the regions that experienced more earthquakes compared to those with fewer occurrences.

Subsequently, AI was asked if it was possible to expect more earthquakes in particular regions compared to others, and the AI's response, after processing the Italian seismic data, confirmed that more earthquakes were expected in certain regions compared to others, based solely on seismic data.

After carrying out these procedures, AI was used to create a chart showing a ranking of regions most subject to future M2+ earthquakes in a short temporal context (a few days), starting from February 4, 2024 (Fig. 1).

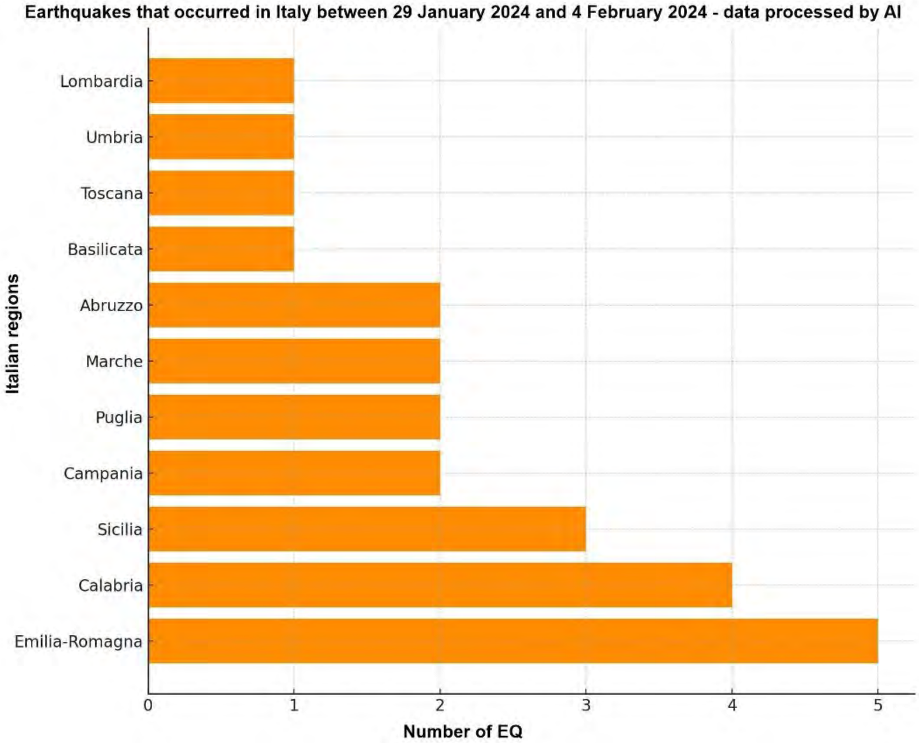

Fig. 1 – Chart related to the number of earthquakes that occurred in Italy between January 29, 2024, and February 4, 2024. In this case, AI compiled a ranking of the regions with the most earthquakes. Credits: Daniele Cataldi.

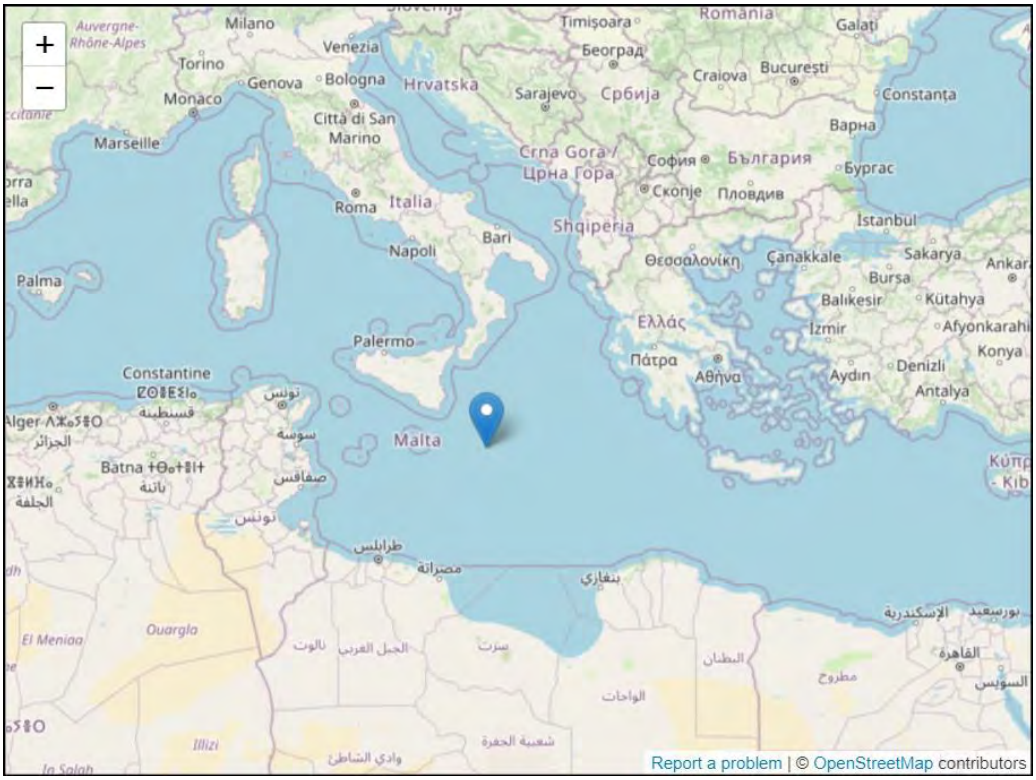

Fig. 2 - Earthquake of magnitude M4.2 on February 5, 2024. Credits: INGV.

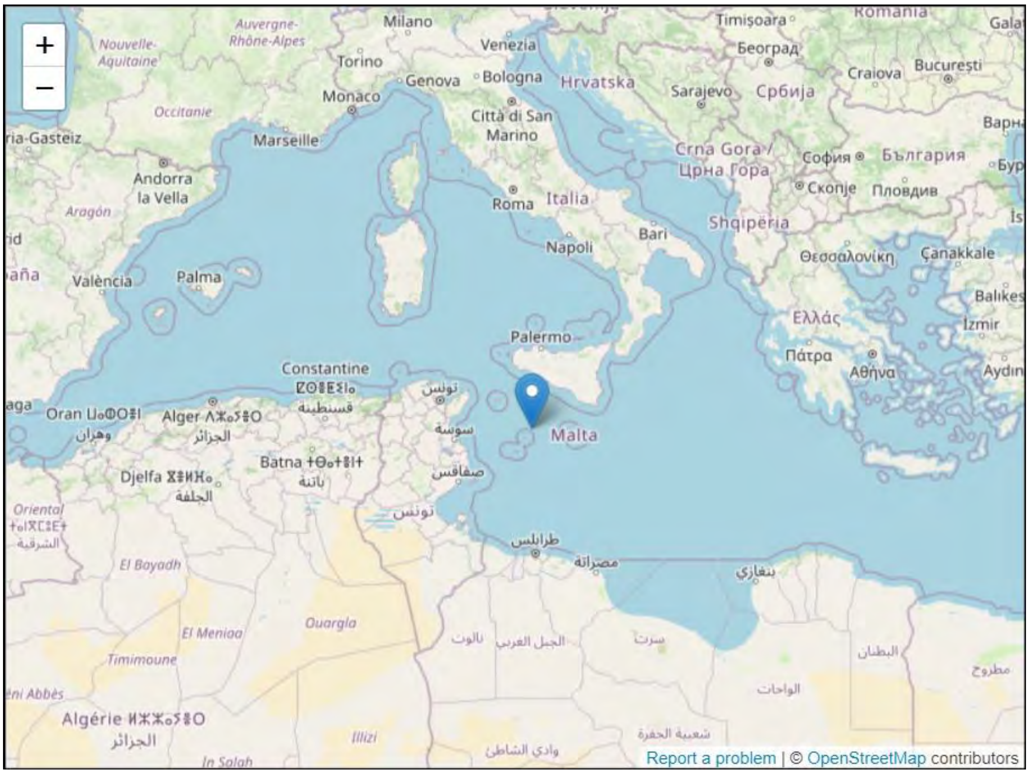

Fig. 3 - Earthquake of magnitude M2.5 on February 6, 2024. Credits: INGV.

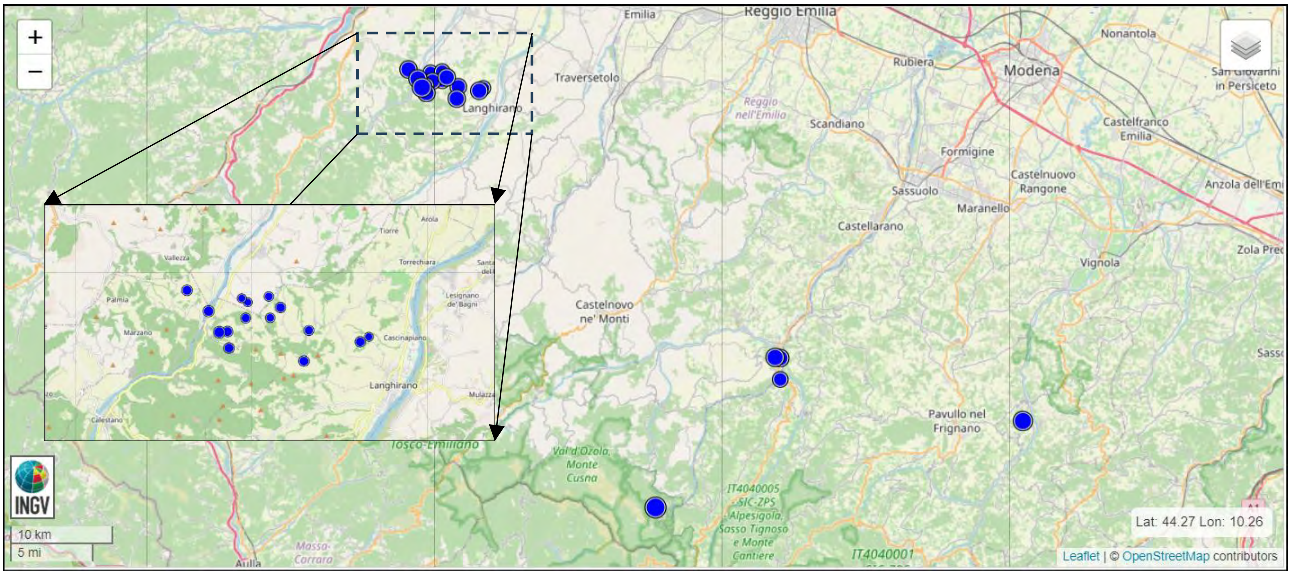

Fig. 4 - Local seismic swarm in Emilia Romagna, Italy, occurred between February 6 and February 7, 2024. Credits: INGV.

The subsequent question posed to the AI concerned the higher likelihood of earthquake occurrences in areas where seismic events had already taken place. The AI's response was positive despite the complexity of the phenomena, where it is not possible to derive certain data from statistical data alone.

The earthquakes considered in this study, referring to the seismic sequence in Emilia, are the following:

- 2024-02-06 22:49:22 ML 2.2 - 2 km NW Montefiorino (MO)
- 2024-02-06 23:37:36 ML 2.5 - 6 km E Calestano (PR)
- 2024-02-07 05:02:02 ML 3.2 - 9 km W Frassinoro (MO)
- 2024-02-07 05:31:42 ML 2.3 - 6 km NW Langhirano (PR)
- 2024-02-07 05:32:00 ML 2.6 - 4 km W Langhirano (PR)
- 2024-02-07 05:41:59 ML 2.8 - 6 km NE Calestano (PR)
- 2024-02-07 05:46:33 ML 2.0 - 7 km W Langhirano (PR)
- 2024-02-07 06:24:29 ML 2.5 - 6 km NE Calestano (PR)
- 2024-02-07 06:26:38 ML 2.1 - 2 km NW Langhirano (PR)
- 2024-02-07 06:33:10 ML 2.2 - 6 km W Langhirano (PR)
- 2024-02-07 07:25:32 ML 2.4 - 6 km W Langhirano (PR)
- 2024-02-07 08:15:18 ML 2.4 - 4 km W Langhirano (PR)
- 2024-02-07 08:20:32 ML 2.1 - 7 km W Langhirano (PR)
- 2024-02-07 08:29:55 ML 2.7 - 6 km NE Calestano (PR)
- 2024-02-07 09:01:13 ML 2.6 - 5 km NW Langhirano (PR)
- 2024-02-07 09:14:58 ML 2.5 - 6 km NE Calestano (PR)
- 2024-02-07 09:27:59 ML 2.6 - 2 km NW Langhirano (PR)

These are the earthquakes that occurred between February 6, 2024, at 22:49 UTC, and February 7, 2024, at 09:27 UTC. (Source: INGV).

3 - Discussion

The pursuit of earthquake prediction research represents a context of significant development, particularly when considering new instruments and technologies capable of supplying a more extensive and diverse array of data. This diversification, when combined with other data within a multidisciplinary framework, may yield more accurate insights into crustal diagnostics and phenomena preceding earthquakes.

The initial seismic event documented was an earthquake of magnitude ML 4.2 on February 5, 2024, at 08:14:56 (UTC) in Italy (offshore), as depicted in Figure 2. Despite occurring at sea, this earthquake is part of the Sicilian region, ranked third by AI as an area prone to seismic activity.

The second seismic event documented was an earthquake of magnitude ML 2.5 on February 6, 2024, at 23:37:10 (UTC) in the southern Sicilian Channel (sea). Though not occurring on land, this event also took place within Italian territory, specifically referring to the Sicilian area (as shown in Figure 3).

The most significant event, from an AI predictive perspective, occurred between the end of February 6, 2024, and February 7, 2024, when a local seismic swarm began in Emilia Romagna (as shown in Figure 4). Given this latest event (swarm), occurring precisely in the area AI had identified as the most likely Italian geographical zone to experience earthquakes with magnitudes over M2, it is evident that data from the INGV archives can have predictive value if interpreted in a certain manner.

The processed data are of a simple type, based on the temporal localization of earthquakes, their number, their magnitude, and their distribution relative to a specific geographical area, in this case, Italy.

Hence, this result takes into account actual seismic data from which predictive information provided by AI could be derived, within a very short temporal context and given the low heterogeneity of the data, it was not possible to provide more precise spatial and temporal indications.

Existing studies are contemplating the use of AI within a seismic research context [10] [11] [12] [13] [14]. These studies represent merely the initial phase of research that, in the coming years, will deliver significant advancements across all fronts of technology and research.

4 - Conclusion

The pursuit of earthquake forecasting represents a highly developed field, particularly when considering new tools and technologies capable of providing a larger and more diversified array of data. Such diversification, when combined with other data already in possession of researchers, can undoubtedly offer more precise indications that may aid in understanding parts of the seismogenic phenomena preceding earthquakes.

In this instance, although the study was based on a limited set of data, it highlighted how AI was capable of retrieving and corroborating data, providing predictive insights that proved to be accurate. It is no coincidence that the seismic swarm, which occurred in Emilia Romagna, Italy, happened precisely in the location the AI had identified as the first Italian region where there would be a higher probability of expecting earthquakes with a magnitude of M2+ (as shown in Fig. 1).

This demonstrates the importance of utilizing increasingly up-to-date tools, of employing multiple data sources, which can then be processed by AI. In this case, this small study was conducted solely with seismic data from INGV, but it is hopeful that in the not-too-distant future it will be possible to provide AI with more types of data, so that it can offer more accurate seismic forecasting indications.

There are already studies in this area that contemplate the use of AI within a seismic research context [10] [11] [12] [13] [14]; these studies are merely the initial phase of research that in the coming years will provide significant developments on all fronts of technology and research. In this scenario, researchers must employ such knowledge and tools to overcome, as soon as possible, the challenges that still exist today in earthquake forecasting research.

References

[1] R. Karjian - The history of artificial intelligence: Complete AI timeline - TechTarget - Enterprise AI - 2023. https://www.techtarget.com/searchEnterpriseAI/tip/The-history-of-artificial-intelligence-Complete-AI-timeline

[2] R. Stuart J.; N. Peter. (2021). Artificial Intelligence: A Modern Approach (4th ed.). Hoboken: Pearson. ISBN 978-0134610993. LCCN 20190474.

[3] Byrne J. G. (8 December 2012). "The John Gabriel Byrne Computer Science Collection". Archived from the original on 16 April 2019. Retrieved 8 August 2019.

[4] L. Torres Quevedo (1914), "Revista de la Academia de Ciencias Exacta", Ensayos sobre Automática – Su definicion. Extension teórica de sus aplicaciones, vol. 12, pp. 391–418.

[5] L. Torres Quevedo (1915), "Revue Génerale des Sciences Pures et Appliquées", Essais sur l'Automatique - Sa définition. Etendue théorique de ses applications, vol. 2, pp. 601–611.

[6] Butler, S. (13 June 1863), "Darwin Among the Machines", The Press, Christchurch, New Zealand, retrieved 10 October 2008.

[7] Chatterjee, S.; N.S. Sreenivasulu; H. Zahid (1 January 2021). "Evolution of artificial intelligence and its impact on human rights: from sociolegal perspective". International Journal of Law and Management. 64 (2): 184–205. DOI:10.1108/IJLMA-06-2021-0156 - ISSN 1754-243X. S2CID 238670666.

[8] P. Gualtiero (1 August 2004). "The First Computational Theory of Mind and Brain: A Close Look at Mcculloch and Pitts's "Logical Calculus of Ideas Immanent in Nervous Activity"". Synthese. 141 (2): 175–215. DOI:10.1023/B:SYNT.0000043018.52445.3e. ISSN 1573-0964. S2CID 10442035.

[9] Widrow, B.; Lehr, M.A. (September 1990). "30 years of adaptive neural networks: perceptron, Madaline, and backpropagation". Proceedings of the IEEE. 78 (9): 1415–1442. DOI:10.1109/5.58323. S2CID 195704643.

[10] Y. Chen; A. Savvaidis; O.M. Saad; G.-C. Dino Huang; D.Siervo; V. O'Sullivan; C. McCabe; B. Uku; P. Fleck; G. Burke; N.L. Alvarez; J. Domino; I. Grigoratos - TXED: The Texas Earthquake Dataset for AI - GeoScienceWorld - Seismological Research Letters (2024). https://doi.org/10.1785/0220230327.

[11] S. Biswas, D. Kumar, M. Hajiaghaei-Keshteli, U. K. Bera - An AI-based framework for earthquake relief demand forecasting: A case study in Türkiye - International Journal of Disaster Risk Reduction (2024).

[12] Chen Wang, Junxian Zhao, Tak-Ming Chan - Artificial intelligence (AI)-assisted simulation-driven earthquake-resistant design framework: Taking a strong back system as an example - Engineering Structures (2023). DOI: 10.1016/j.engstruct.2023.116892.

[13] Xinzheng Lu, Henry Burton, Masayoshi Nakashima - AI and data-driven methods in earthquake engineering - Earthquake Engineering & Structural Dynamics (2022) - DOI: 10.1002/eqe.3647.

[14] Ariska Rudyanto, Danny Gho, Arief Tyastama, Dwi Karyadi, Pei-Yang Lin - Unveiling the potential: preliminary result on an AI-based onsite earthquake early warning system deployment in Denpasar City - E3S Web of Conferences (2023). DOI: 10.1051/e3sconf/202346402002.

Earthquakes, Solar Activity, and Bright Meteors

Daniele Cataldi[1-2], Gabriele Cataldi[1], Valentino Straser[3]

(1) Radio Emissions Project (I). ltpaobserverproject@gmail.com
(2) LTPA Observer Project (I). daniele77c@hotmail.it
(3) Department of Science and Environment UPKL Brussel (B). valentino.straser@gmail.com

Abstract

In recent decades, the observation of the sky has experienced an exponential growth in amateur astronomical observatories, primarily based on high-sensitivity CCTV cameras capable of capturing the night sky, thereby highlighting the transit of meteors. Within this context, there are actual international networks of observatories capable of providing data on the detection of these luminous appearances. In Italy, one of the most active stations is the LTPA Observer Project, established in 2007, which is equipped to monitor the night sky daily and provide key data on astronomical recordings associated with the passage of meteoric bodies in orbit around the Sun, attracted by Earth's gravitational force. In this realm, the study of these events has led to the emergence of a new investigative technique associated with seismic prediction. The LTPA Observer Project and the Radio Emissions Project, two Italian scientific initiatives for studying visible atmospheric luminous phenomena and seismic precursors, have highlighted the need to understand if sometimes the observation of large fireballs can be associated with the occurrence of strong earthquakes, albeit in a temporal context. This study explores precisely this possibility, namely whether the appearance of large fireballs can be considered a new, previously unknown seismic precursor, and whether this meteoric activity could be linked to solar activity.

Keywords: Meteor, Earthquakes, Astronomy, Seismic Precursors, Eliophisics.

1 - INTRODUCTION

The question we posed is whether the observation of large fireballs could be considered a new candidate for seismic precursor, given the emerging relationship between the frequency of large and bright fireballs, solar activity characterized by an increase in space weather phenomena such as M and X class solar flares.

Meteors originate from meteoroids, which are particles of varying sizes, often coming from comets or asteroids and wandering within the solar system, orbiting the Sun. When a meteoroid approaches a celestial body, like Earth, it enters its atmosphere at high speeds, typically between 11 km/s and 72 km/s. This rapid descent causes extreme heating of the meteoroid and the surrounding air, creating a visible glow. The high speed of the meteoroid leads to the ionization of gases in the atmosphere, creating a luminous trail. The brightness of a meteor depends on the size, composition, and speed of the meteoroid, as well as the atmospheric density.

Meteor, Meteoroid, Meteorite: It is important to distinguish between a meteoroid (the rock fragment in space), a meteor (the luminous phenomenon observed when the meteoroid passes through the atmosphere), and a meteorite (any fragment of the meteoroid that survives its passage through the atmosphere and reaches the Earth's surface). [1]

Meteors are classified based on their brightness. The most common are low-luminosity meteors, followed by fireballs and superbolides, which are rare but extremely bright events. A classification of meteors based on brightness, visual magnitude, velocity, distance, and color is as follows:

Low-Luminosity Meteors (Magnitude +5 and above)

- Visual Magnitude: Greater than +5.
- Speed: Varies from 11 km/s (slow meteors) to 72 km/s (very fast).
- Distance: Several tens of kilometers above the Earth's surface.
- Color: Often not very defined due to low brightness; can vary from white to pale yellow.

Bright Meteors (Magnitude from +2 to +5)

- Visual Magnitude: Between +2 and +5.
- Speed: Generally between 30 km/s and 70 km/s.
- Distance: Typically between 70 and 100 km from the observer.
- Color: More defined, with possible shades of yellow, orange, or green depending on the chemical composition.

Fireballs (Magnitude from -1 to +2)

- Visual Magnitude: Between -1 and +2.
- Speed: Often over 20 km/s.
- Distance: Can appear closer due to their greater brightness.
- Color: Variable; yellow, orange, green, and sometimes blue, influenced by composition.

Bright Fireballs (Magnitude from -5 to -1)

- Visual Magnitude: Between -5 and -1.
- Speed: Similar to fireballs, but can appear faster due to greater brightness.
- Distance: Variable, but often closer to the observer.
- Color: Often vivid and variable, with possible long-lasting trails.

Superbolides (Magnitude lower than -5)

- Visual Magnitude: Lower than -5, can reach up to -20.
- Speed: Extremely fast, can exceed 70 km/s.
- Distance: Can be seen from hundreds of kilometers away.
- Color: Very bright and variable, often accompanied by a strong glow and sometimes audible explosions.

The classification of meteors varies based on their brightness, which is closely related to their size, speed, and chemical composition. Visual magnitude is an important parameter as it determines how easily a meteor can be observed with the naked eye. Speed and distance affect the apparent duration of the light trail in the sky. Finally, the color is an indicator of the meteor's chemical composition; for example, sodium produces a yellow color, while iron tends to give a green tint. [2] [3] [4] [10]

1.2 - Solar Activity and Meteoroids

As is known, solar activity plays a fundamental role in the movement of these particles (meteoroids), this interstellar dust, in which we all are immersed, is affected by the variation in solar activity, that is, by the phenomena generated by the Sun. Among these, the ones that we can consider in this study include the following:

- **Coronal Mass Ejections (CMEs)**: CMEs are enormous ejections of plasma and magnetic field emitted by the Sun, capable of traveling through space at high velocities (even 1,000,000 km/h). When these charged particles interact with meteoroids, they can alter their trajectories, especially if the meteoroids are of small size and/or have low mass. [5][7]
- **Solar Wind**: The solar wind, a continuous flow of charged particles emitted by the Sun, can have a cumulative effect on meteoroids over time. This can gradually alter their orbits, especially in relation to smaller bodies. [6]

- **Yarkovsky and YORP Effects**: For larger bodies, thermal effects like the Yarkovsky effect and YORP (Yarkovsky-O'Keefe-Radzievskii-Paddack) can play a significant role. These effects are influenced by solar radiation and can cause changes in the rotation and orbit of celestial bodies. [9]
- **Interaction with the Earth's Magnetic Field**: As meteoroids approach Earth, they can also interact with the Earth's magnetic field, which in turn is influenced by solar activity, particularly during geomagnetic disturbance events. [8]
- **Impact on Space Weather Events**: Space weather events, such as geomagnetic storms, can influence the intensity and direction of the solar wind and CMEs, thus further affecting the trajectories of meteoroids. These interactions illustrate the complex dynamics between solar activity and meteoroids, highlighting the importance of studying these relationships to understand better the movement and behavior of these particles in space. [7]

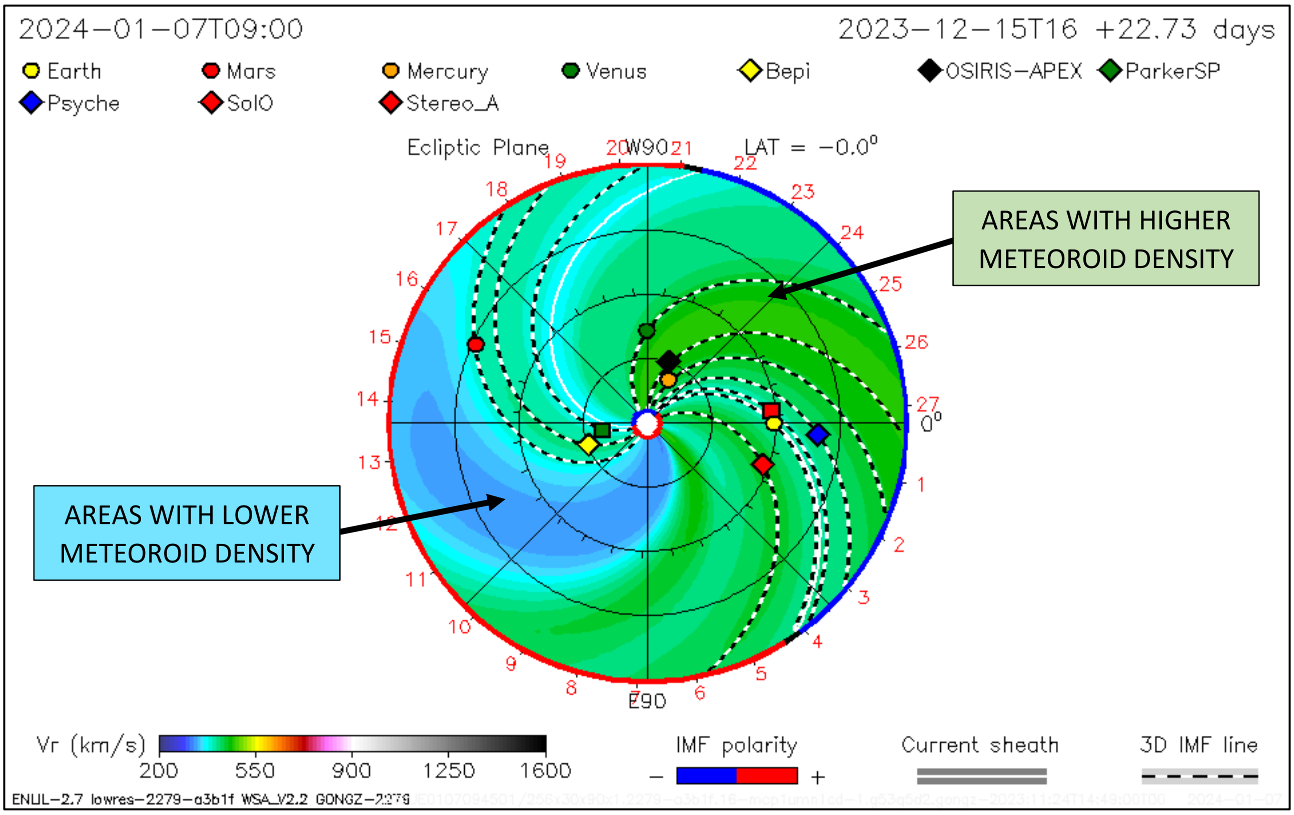

Fig. 1 – Graph showing the velocity of the solar wind. At the center is the Sun, and around it are the various nearest planets, along with the positions of various space probes. Credits: iSWA.

Therefore, as can be understood, this interstellar dust present within the solar system is subject to the flow of the solar wind and the action of shock waves that the sun creates through Flares and CMEs, effectively drawing this dust closer to the planets. This is because the solar wind originates from the Sun and radiates outward from the star, reaching the planets. In this interlude, solar activity moves a mass of dust, the density of which is directly proportional to the extent of the solar activity.

A CME of enormous proportions and speed can carry with it more dust, compared to a CME of lesser magnitude. These characteristics related to solar activity, mentioned so far, are the basis of the hypothesis advanced by researchers engaged in this study.

As visible in Fig. 1, the speed of the solar wind varies with the solar activity itself; there are thus areas in space where the speed of the solar wind is greater compared to other areas, or vice versa, in reference to the presence of sunspots, coronal holes, and general phenomena on the solar chromosphere.

1.3 - L'LTPA Observer Project

In the course of studying space weather, the LTPA Observer Project, based in Italy, has since 2008, begun recording the passage of meteors over Italian territory (central Italy) using a CCTV camera with a sensitivity range between 0.00001 and 0.00045 lux (in Full Time Color), sufficient to observe in color not only the light of the stars but also all astronomical phenomena visible to the naked eye, including the passage of meteors. This CCTV camera is defined as a "Starlight Camera".

Over the years, it has detected a series of extremely luminous meteoric phenomena, determined by the passage of meteorites of a certain size, capable of illuminating the sky, fragmenting, and in some cases falling to the ground.

From 2008 to the present, this CCTV Camera has operated for over 70,450 hours for its sky surveillance work.

This recording system has also required over 5,870 hours of processing the recorded images, sufficient to catalog the types of phenomena recorded over the years.

This system was the first in Italy to use such sensitive equipment to detect LTPAs or Luminous Transient Phenomena in the Atmosphere, the whole series of luminous phenomena that occur in the Earth's atmosphere, including bright meteors.

An example of such recordings is that of July 21, 2011, when at 01:57 local time, the optical detection station, located in Lariano, Rome, Italy, recorded the passage of a large fireball (Fig. 2).

In this case, the system highlighted its passage, detecting the luminous trail. Another example is that of August 12, 2011, when at 22:29 local time, the optical station located in Lariano, Rome, Italy, recorded the passage of a large fireball (Fig. 3).

***Fig. 2** – Bright fireball recorded by the optical monitoring station of the LTPA Observer Project, located in Lariano, Rome, Italy. Credits: Daniele Cataldi; LTPA Observer Project.*

Fig. 3 *– Bright fireball recorded by the optical monitoring station of the LTPA Observer Project, situated in Lariano, Rome, Italy. Credits: Daniele Cataldi; LTPA Observer Project.*

The most intense event ever recorded by the station in February was that of February 12, 2011, at 23:34 local time, when a superbolide entered the Earth's atmosphere, illuminating the entire Tyrrhenian area.

The last two frames recorded even show the saturation of the CCD sensor of the CCTV camera, caused by the high intensity of the light flash produced by the impact between the meteoroid and the Earth's atmosphere at an altitude of 80 km (Fig. 4). In this case, the visual magnitude was calculated to be -18.

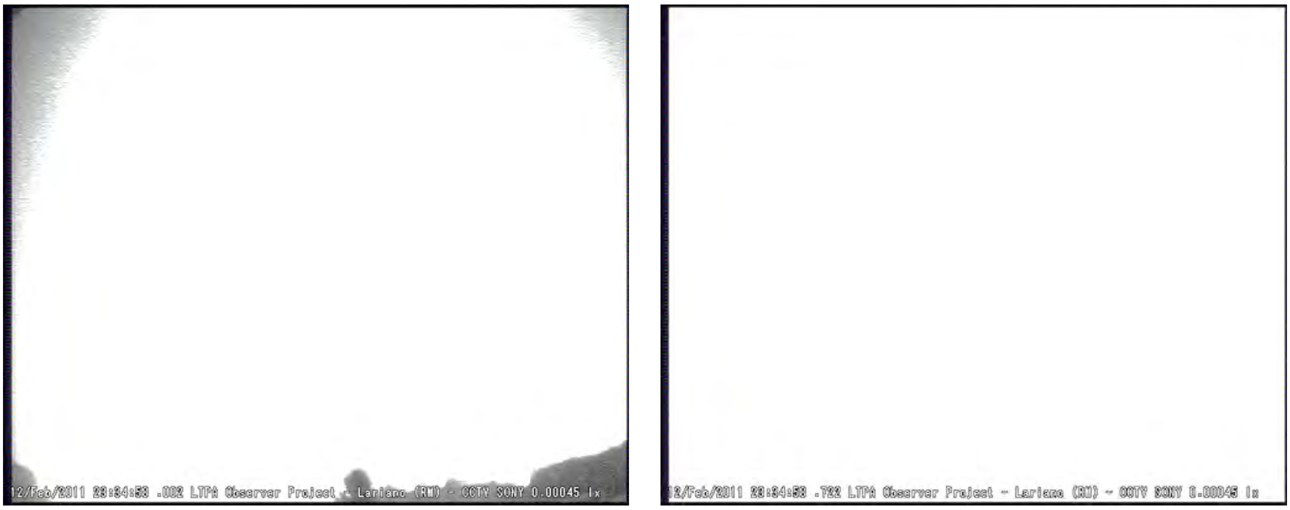

Fig. 4 *– Optical station of the LTPA Observer Project, in Lariano, Rome, Italy, where the recording of the passage of a superbolide, recorded on February 12, 2011, is highlighted. Credits: Daniele Cataldi; LTPA Observer Project.*

The event was subsequently highlighted by various national and international associations and entities, given the exceptional nature of the recording, which had never occurred before in Italy.

2 - METHOD AND DATA

The study conducted by the researchers documented the appearances of large and bright meteors or fireballs on a global scale, limiting the research to large fireballs with a magnitude not exceeding -5.

Similarly, these data were overlaid with solar activity data, namely the count of class M and X Flares that occurred in the same time period, and the global seismic activity of M6+.

The time period covered by the graph, based on the provided data, spans from April 2022 to December 2023. Here is a clarification of the time limits:

- Start: The first event in the graph is a class X solar flare that occurred on April 20, 2022.
- End: The last event in the graph is a class X solar flare that occurred on December 14, 2023.

Therefore, the graph represents a period of approximately 1 year and 8 months, showing the sighting of meteors and the class M and X solar flares that occurred during this time frame. The appearances of the fireballs were obtained through web research on the most important sites for this type of phenomenon.

The retrieval of data related to the passages of luminescent meteors across the sky has been significant and very challenging since typically, these types of appearances last only a few seconds and are not recorded.

2.1 – Meteor and Solar Flares

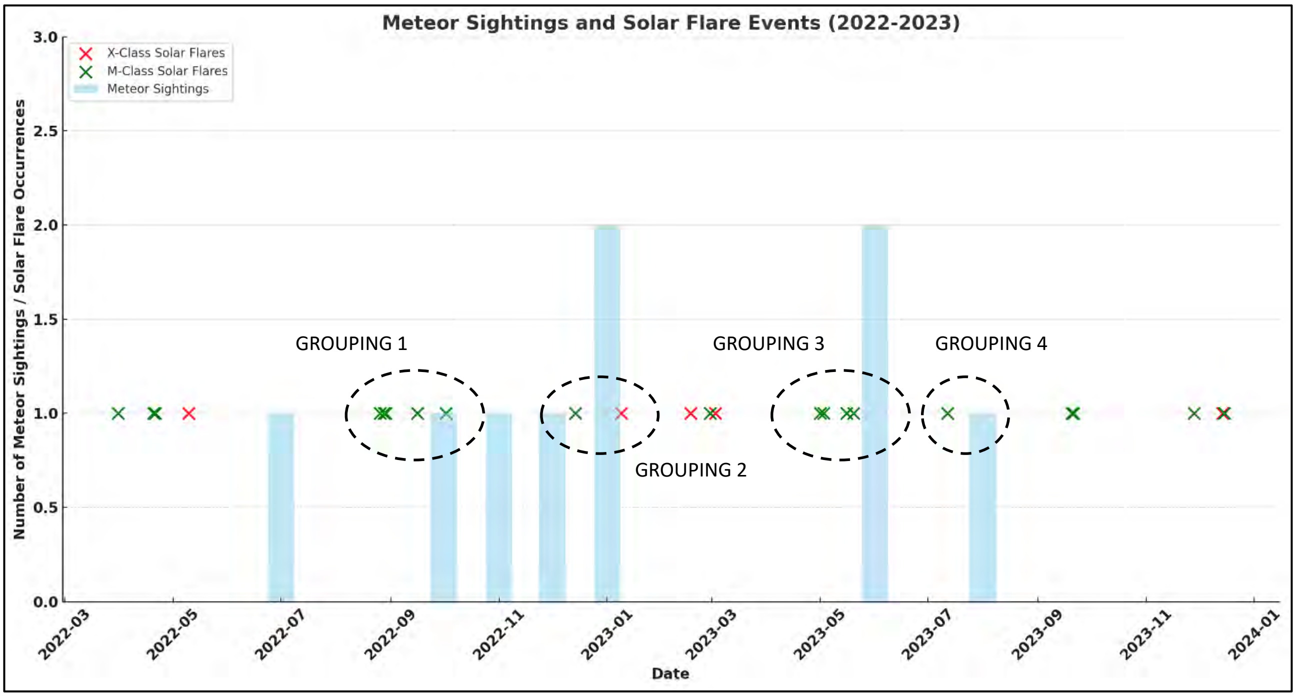

Fig. 5 – Graph showing the trend of solar activity (class M and X Flares) and the appearance of large and bright meteors (Fireballs), observed on a global scale. Credist: iSWA; LTPA Observer Project; International Meteor Organization (IMO); NASA's Meteoroid Environment Office (MEO); European Fireball Network; Global Fireball Observatory (GFO).

Only some of these passages are recorded by the numerous amateur observatories, so the data available to researchers do not include every appearance that occurred, but only those that have been possible to document.

In some cases, the data refer to those reported by a larger number of people, even if not captured by cameras or sensors for detecting this kind of astronomical phenomena. The documentation visible in Fig. 2, 3, and 4 demonstrates that it is possible to detect and study such phenomena and that they are more frequent than one might normally believe.

2.2 – Seismic Events

An important element for this study was to understand when the phenomenon of the appearance of large fireballs could be related to the occurrence of earthquakes on a global scale, that is, whether there existed a second relationship between observing large fireballs and the occurrence of destructive earthquakes with a magnitude of M6+.

The researchers engaged in this study gathered the number of earthquakes that occurred within the same time period in which the large fireballs and class M and X Flares appeared (Source: USGS):

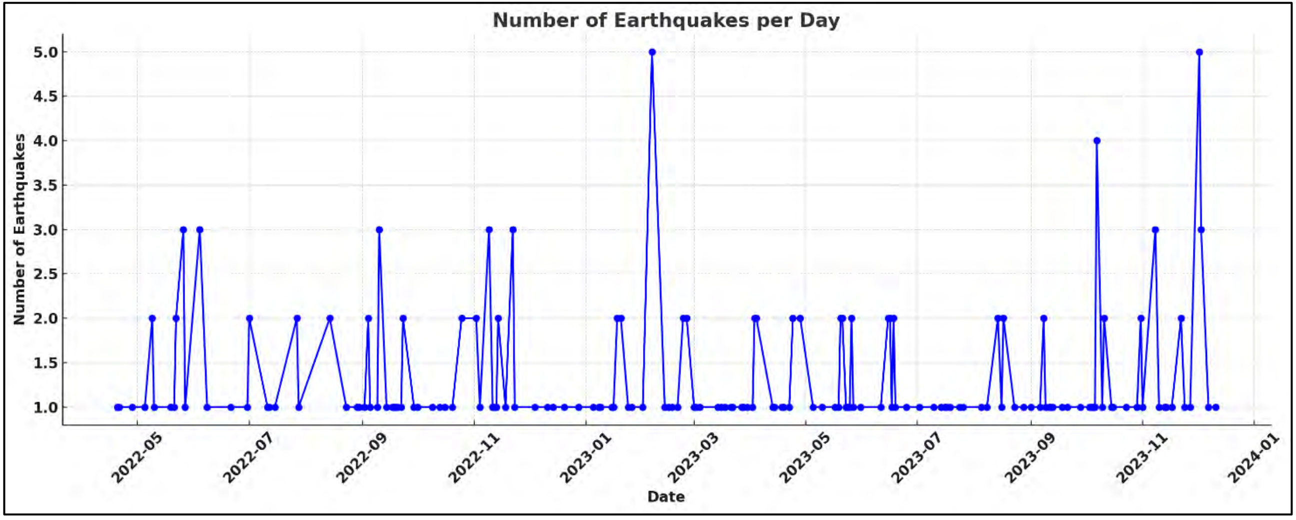

Fig. 6 *– Number of earthquakes that occurred between 20 April 2022 and 14 December 2023, on a global scale and with magnitude M6+. Credits: USGS.*

As can be seen in Fig. 6, there were many earthquakes with magnitude M6+, on a global scale, in the same calculated time frame, i.e. between 20 April 2022 and 14 December 2023.

The next step was to superimpose this graph on the number of meteors observed and the number of class M and X Flares observed in the same period of time (Fig. 7).

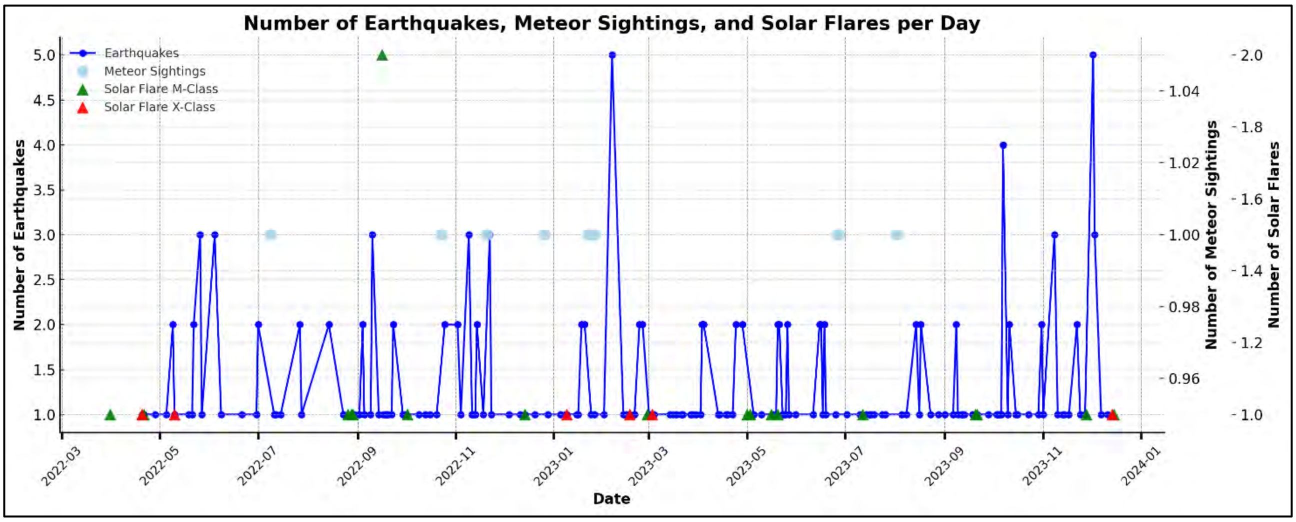

Fig. *7 – Number of M6+ earthquakes, number of M and X class solar flares and number of large bolides observed on a global scale. Credits: LTPA Observer Project, USGS, International Meteor Organization (IMO); NASA's Meteoroid Environment Office (MEO); European Fireball Network; Global Fireball Observatory (GFO); iSWA.*

3 - DISCUSSION

Solar activity generates shock fronts whose speed can reach the Earth in 3 days, traveling at approximately (2,077,748 km/h) 577.15 km per second. If we calculate that medium-sized meteors travel at around 72 km/s we can understand that solar activity creates areas of space in which an enormous acceleration is provided to meteoric bodies (meteoroids), of around 8.2 times compared to their speed. This implies that in certain areas of the space between the Earth and the Sun, there are greater quantities of rocky bodies (dust in which meteoroids are found), as visible in Fig. 1, and that these areas, in which there are greater fragments in motion, they approach the Earth at greater speed.

After acquiring the data, distributing them temporally for a duration of 20 months (1 year and 8 months), relationships were sought between the appearance of individual meteors and solar flares. The result is shown in Fig. 5, where small groupings of Flares (Greater solar activity) and the appearance of the brightest meteors are highlighted. The data collected in the graph are the following (source USGS; NASA's Meteoroid Environment Office (MEO); European Fireball Network; Global Fireball Observatory (GFO):

Meteorite Sightings (Real Data)

- Nottingham, England (9 July 2022).
- Wisconsin, USA (23 October 2022).
- Tennessee and Kentucky, USA (20 November 2022).
- Adelaide, Australia (26 December 2022).
- South Yorkshire, England (22 January 2023).
- Cabo Rojo, Puerto Rico (January 26, 2023).
- Germany (26 June 2023).
- New Zealand (27 June 2023).
- United States (August 2, 2023).

Class X Solar Flares (2022 - 2023)

- X2.25: April 20, 2022.
- X1.5: May 10, 2022.
- X2.87: December 14, 2023.
- X2.2: February 17, 2023.
- X2.07: March 3, 2023.
- X1.9: January 9, 2023.

M-Class Solar Flares (2022 - 2023)

- M9.7: April 21, 2022.
- M9.67: March 31, 2022.
- M8.77: October 2, 2022.
- M8.6: August 29, 2022.
- M7.9: September 16, 2022.
- M7.29: April 20, 2022.
- M7.2: August 26, 2022.
- M6.7: August 28, 2022.
- M6.3: December 14, 2022.
- M6.2: September 16, 2022.
- M9.82: November 28, 2023.
- M9.62: May 16, 2023.
- M8.96: May 20, 2023.
- M8.72: September 21, 2023.
- M8.62: February 28, 2023.
- M8.23: September 20, 2023.
- M7.2: May 3, 2023.
- M7.1: May 1, 2023.
- M6.97: December 15, 2023.
- M6.97: July 12, 2023.

As it is possible to understand, the appearances of large fireballs (meteors) are not very frequent, but in any case there are a total of 9. There were 5 class X Flares that occurred on the Sun, and 20 were M class Flares. The graph (Fig 5) show:

- **Grouping 1**: between the end of August 2022 and October 2022 there was a large fireball sighted, preceded by a Series of M-class Flares.
- **Grouping 2**: another interesting grouping is that between December 2022 and January 2023, when a class
- **Grouping 3**: the presence of numerous M-class Flares was highlighted, followed by the appearance of two large meteors (May 2023 – June 2023).
- **Grouping 4**: the presence of a class M Flare in the local vicinity of a luminous fireball between July 2023 and August 2023 is highlighted.

It is evident that most of the bright meteors appeared close (temporally) to a grouping of solar flares.

Other important data are the seismic data relating to the same time period, i.e. all the M6+ earthquakes that occurred on a global scale.

The researchers' study focused on verifying whether there could be a relationship between all these phenomena; in the past, a clear relationship between earthquakes and solar phenomena has already been observed [11] [12] [13] [14] [15], in this case it was possible to ascertain this relationship again by observing Fig. 7 where the number of M6+ earthquakes, the number of M and X class solar flares, and the number of appearance of large fireballs are visible.

For the first time ever this study shows what was previously a hypothesis of the researchers and which in this case the data confirmed, that is, that the number of large fireballs follows the groupings of earthquakes, especially those with the greatest number of cases occurring in short time.

In addition to this, it is highlighted that the Flares are always associated with the presence of strong earthquakes and in this case, again as already described for Fig. 5, there is a clear relationship between the number of large fireballs spotted and solar activity.

4 - CONCLUSION

It is concluded that, at least on a hypothesis level but supported by data, solar activity can be associated with the occurrence of M6+ earthquakes on a global scale.

Solar activity, in this context, plays an important role in bringing interstellar dust, in which fragments of more or less large rocks move, closer to celestial bodies such as the Earth.

In particular, the number of luminous fireballs with a magnitude no lower than -5 in brightness, analyzed in this study, is linked to solar activity and earthquakes.

Solar activity also appears to interact on the orbits of larger fragments, which are usually less susceptible to variations in their orbit than smaller fragments.

This could explain the existence of a direct relationship between the appearance of large meteors and intense solar activity. More evident, however, seems to be the relationship between solar activity and earthquakes, summarized in Fig. 7, while at present the relationship between solar activity and meteoric phenomena is less evident, if referred to the analysis of events lasting 1 year and 8 months.

REFERENCES

[1] Коротышкин Д.В., Шерстюков О.Н., Валиуллин Ф.С. - Meteor observations at the radar station of Kazan Federal University - INASAN Science Reports. Vol 8(6). M.: Janus-K, 2023, 58 pp. - DOI: 10.51194/INASAN.2023.8.6.002 - ISSN 2658-5669 e-ISSN 2712-8318

[2] V.́ı. Porubcan, M. Bucek, G. Cevolani, P. Zigo. Variation of Meteor Heights and Solar-Cycle Activity - PASJ: Publ. Astron. Soc. Japan 64, 86, 2012 August 25 (C) 2012. Astronomical Society of Japan - (Received 2011 December 9; accepted 2012 February 24). DOI: 10.1093/pasj/64.4.86.

[3] P. Matlovič, J. Tóth. Meteors: Light from Comets and Asteroids - 2019 - Computational Structural Engineering Institute of Korea - Online ISSN: 2287-2302 - Print ISSN: 1229-3059 - DOI: 10.7734/COSEIK.2019.32.2.133.

[4] S. Feng, R. Wang. Meteoroid and Space Debris Risk Assessment for Satellites Orbiting the Earth/Moon - Received: Nov 3, 2022 Accepted: Jun 25, 2023 Published: Sep 19, 2023 - Chinese Journal of Space Science, Volume 43, Issue 4: 724 - 735 (2023) - DOI: 10.11728/cjss2023.04.2022-0065.

[5] S. E. Gibson, U. Bąk-Stęślicka, R. Casini, J. Dahlin, E. DeLuca, G. de Toma, Y. Fan, J. Karpen, L. A. Rachmeler, S. Tomczyk, A. Caspi, B. Chen, M. Corchado-Albelo, S. Farid, N. Karna, T. Kucera, A. Paraschiv, N. E. Raouafi, T. Schad, D. Seaton, S. Begum Shaik, M. L. Wilson, J. Zhang. Coronal Polarimetry: Determining the Magnetic Origins of Coronal Mass Ejections - 2023 - Heliophysics 2024 Decadal Whitepapers- Vol. 55, Issue 3 - DOI: 10.3847/25c2cfeb.8528ec7b.

[6] R. Reda, M. Stumpo, L. Giovannelli, T. Alberti, G. Consolini. Disentangling. the solar activity–solar wind predictive causality at Space Climate scales - 2024 - Frontiers in Italian studies on Space Weather and Space Climat - DOI: 10.1007/s12210-023-01213-w.

[7] H. Raju, S. Das. Interpretable ML-Based Forecasting of CMEs Associated with Flares - 2023 - Solar Physics - 298(8) - DOI: 10.1007/s11207-023-02187-6.

[8] C.D. Watkins, R. Eames, T.F. Nicholson. Further studies of the effect of the Earth's magnetic field on meteor trains - Journal of Atmospheric and Solar-Terrestrial Physics - Elsevier BV - 33(12):1907–1921 - DOI: 10.1016/0021-9169(71)90167-X.

[9] F. Marzari, A. Rossi, O. Golubov, D. J. Scheeres. Evolution of an Asteroid Family under YORP, Yarkovsky, and Collisions - The Astronomical Journal - Published 2020 August 21 © 2020 - DOI 10.3847/1538-3881/aba7be.

[10] R. Sennlaub, M. Hofmann, M. Hankey, M. Ennes, T. M Uller, P. Kroll, P. Mader. Patrick MäderPatrick Mäder. Object classification on video data of meteors and meteor-like phenomena: algorithm and data - Monthly Notices of the Royal Astronomical Society - Published by Oxford - University Press - Print ISSN: 0035-8711 - DOI: 10.1093/mnras/stac1948.

[11] V. Straser, G. Cataldi. 2014. Solar wind proton density increase and geomagnetic background anomalies before strong M6+ earthquakes. Space Research Institute of Moscow, Russian Academy of Sciences, MSS-14. Moscow, Russia – 2014.

[12] G. Cataldi, D Cataldi, V. Straser. Solar wind proton density variations that preceded the M6+ earthquakes occurring on a global scale between 17 and 20 April 2014. European Geosciences Union (EGU) General Assembly 2015, Natural Hazard Section (NH5.1), Sea & Ocean Hazard - Tsunami, Geophysical Research Abstract, Vol. 17, Vienna, Austria. Harvard-Smithsonian Center for Astrophysics, High Energy Astrophysics Division, SAO/NASA Astrophysics Data System.

[13] G. Cataldi, D. Cataldi, V. Straser. Solar wind proton density variations that preceded the M6,1 earthquake occurred in New Caledonia on November 10, 2014. European Geosciences Union (EGU) General Assembly 2015, Natural Hazard Section (NH5.1), Sea & Ocean Hazard - Tsunami, Geophysical Research Abstract, Vol. 17, Vienna, Austria. Harvard-Smithsonian Center for Astrophysics, High Energy Astrophysics Division, SAO/NASA Astrophysics Data System.

[14] G. Cataldi, D. Cataldi, V. Straser. Solar activity correlated to the M7.0 Japan earthquake occurred on April 15, 2016. New Concepts in Global Tectonics (NCGT) Journal, Vol. 4, No 1, 2016, Australia.

[15] G. Cataldi, D. Cataldi, V. Straser. Solar and Geomagnetic Activity Variations Correlated to Italian M6+ Earthquakes Occurred in 2016. European Geosciences Union (EGU) General Assembly 2017. Seismology (SM1.2)/Natural Hazards (NH4.7)/Tectonics & Structural Geology (TS5.5) The 2016 Central Italy Seismic sequence: overview of data analyses and source models. Geophysical Research Abstracts Vol. 19, EGU2017-3681, 2017.

Happy 55th Birthday Plate Tectonics Theory

Keith James – Consulting Geologist

(**Editor's note:** *red numbers in brackets refer to Powerpoint slides in accompanying linked appendix on the NCGT Journal website immediately after the link to issue V12 N1***).**

The Plate tectonic paradigm (PT) – "the unifying theory of geology" – has just turned 55. It is an enormous topic with a convoluted history. Theories explaining separating continents used the fit of Atlantic coastlines and fossil distributions as arguments for the former juxtaposition of South America and Africa (Wegener, 1924; (also Green, 1857; Pellegrini, 1857)). Mantle convection moved continents apart (Holmes, 1944).

PT consolidated in the mid-60s as ocean floor data were gathered. They revealed a global system of "mid-ocean" ridges and magnetic sea floor stripes interpreted to record a history of sea-floor spreading (Hess, 1962; Vine & Mathews, 1965.

An episode of exciting collaboration between American and British institutions (see Oreskes, 2001, ***3***) saw new ideas consolidated in a "scientific revolution, analogous to quantum mechanics in physics or genetic code and biology" (Encyclopedia Britannica). Remarkably, cautions noted at that time (e.g. Beloussov, 1970 (4); Heirtzler, Vine & Mathews, 106, 110) were ignored.

Not much has changed since the 60s, apart from sophistication of illustrations. Few question the theory (but see Pratt, 2000 and references therein; Smoot, 2012 records how marine data were misinterpreted/mismanaged).

This article highlights some problems, emerging data and some different possibilities.

PT summary: Supercontinent Pangaea began to fragment in the Triassic. From the Jurassic onward, mid-ocean ridges (MORs) generated new seafloor that moved continents apart. Here, magnetic stripes record Earth's magnetic field, its reversals and spreading progress. This crust is consumed by subduction, which creates blueschists and new continental crust below volcanic arcs. Collision raises mountains.

The United States Geological Survey defines a tectonic plate as a massive, irregularly shaped slab of solid rock (5). This focuses upon 12 - 13 larger crustal elements of continent and ocean that form Earth's crust (6). Boundaries are defined by "oceanic" spreading zones, volcanic island arcs and strike-slip zones. Continental and oceanic plates are different, distinguished by silica content and crustal thickness ***remove comma*** but is this correct? (7, 8, see also below 115 - 117).

For Sylvester (1988) (9, 10, 11), strike-slip faults define plate boundaries. These are abundant and many are major (12, 13, 14, 15, 16, 17). There are many plates.

Dextral and sinistral faults dominate global tectonics in a conjugate northwest and northeast global pattern, (James, 2018). Plates are not irregularly shaped (78, 79).

While normal faults might involve tens of kilometers of displacement and thrusts up to several hundreds, strike-slip displacements can be many hundreds (12 – 15). Wrench faults are the most important structures on Earth. They produce all other structures (16). Stress/strain migration generates basins and uplifts (17). Transtension/transpression generates secondary north-trending extension and east-trending compression (18). The polygonal blocks these define are repeatedly shuffled within this global fabric (see hexagons, below).

Middle America illustrates such faults at work (Fig.1). The area manifests a regional N35°E, N60°W tectonic fabric of reactivated Proterozoic/Palaeozoic faults. It controlled intra-continental extension of the Gulf of Mexico, Yucatán and Caribbean basins. The NE trend corresponds to orogenic lineaments of N and S America. The NW trend occurs as fractures in the western Central Atlantic that continue into the N American continent to offset the NE trends. Several traverse southern N America with offsets of hundreds of kilometres. They bracket the Gulf of Mexico and Caribbean basins (the latter is today bracketed by Eocene – Recent strike-slip along its northern and southern boundaries).

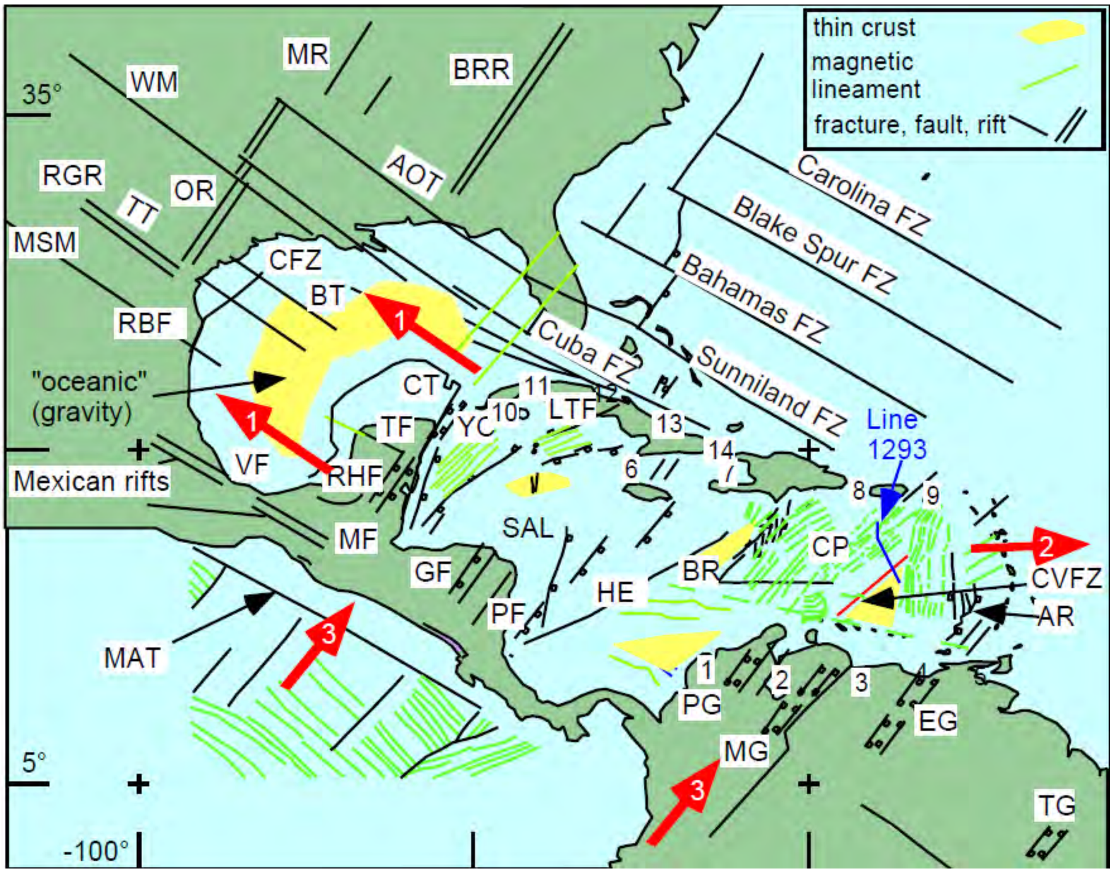

Fig. 1 Tectonic fabric of Middle America - Gulf of Mexico, Yucatán and Caribbean basins.

Key: Arrows – 1) NW migration of SW N America, with extension opening the Gulf of Mexico, Yucatan and Caribbean basins behind it, 2) eastward movement of the Caribbean with eastward extension and radial dispersal of the Lesser Antilles over the Atlantic; 3) NE convergence between the Pacific and the Caribbean in Central America, causing NE-SW shortening of the western Caribbean (James, 2007, fig. 11.12).

Note preservation of regional, Proterozoic NE-SW and NW-SE tectonic fabric

Model-driven interpretations of the Gulf of Mexico derive its opening by anticlockwise rotation of the Yucatan Block (Maya), most recently "supported" by over-interpretation (e.g. Pindell et al., 2016, Fig. 4) of vague gravity and magnetic indications of spreading fabric (Sandwell et al., 2014).

Faults of Maya (Rio Hondo, RHF, Ticul, TF. Fig. 1) conform to regional tectonic fabric and deny rotation. Modelled rotation of the Chortis Block (Guayape, GF; Patuca, PF faults) is also denied.

Rotation of the Iberian plate (Van der Voo, 1969) is similarly disproved by its European fabric. Yet it remains popular and is invoked to explain geology of the Pyrenees. These show dextral strike-slip tectonics.

Plates do not rotate, they move along NE and NW bounding faults.

Rotation around vertical axes (bookshelf) occurs *within* strike-slip zones. If this is not recognized, related magnetic data are incorrectly used to support regional block rotations.

Continental Drift and Reconstruction (19 - 33)

Along with conjugate coastline restoration palaeontology was used to reconstruct the mega-continent Gondwanaland (21). In today's PT, palaeontology takes a back seat.

PT relates India to Antarctica using geochronological data/petrology. Fossil data relate India to neighboring Eurasia.

Monkeys, rodents, freshwater snails, catfish, cichlid fish, angiosperms, flightless birds and manatees evidence Eocene communication between supposedly long-separated (120 my) areas (24 – 27). PT invents bizarre explanations (29 – 32).

According to PT, sea floor spreading (33), driven by mantle convection (34), carried continents apart. Subduction slab pull is the major driver. This is a non-starter – no spreading, no pull, and vice-versa.

2-D models of mantle convection cells rising at MORs, diving below subduction zones and carrying continents apart are still alive but could they be segmented in the third dimension? MOR offsets up to several hundreds of kilometers along fractures rule them out (36, 37).

An alternative proposal is that mid-ocean ridge spreading drives plates apart (see below). Seismic data show ridge rifts bounded by inward-dipping normal faults and increasing oceanward continental extension (see below). Extension does not push (39, 40).

There are 75,000 km of "oceanic" spreading ridges, 30,500 km of trenches and 9,000 km of collision zones (41, 42) – more crust is generated than consumed. Earth is expanding.

Mountains form by collision (PT, 43). Data do not support this (44 – 51). They form by strike-slip transpression, inverting predecessor basins.

Mid-ocean ridges are offset by ocean floor fractures (52, 53). Between offset ridges these are ¨transform" faults (Wilson, 1965, 54). The concept does not hold if Earth is expanding.

Pangaean reconstructions and continental migrations are fraught with unreal changes of direction (e.g. 55, 58).

The hexagon, the strongest known shape, is common in nature. Its energy-efficient geometry involves sides that meet at 120 degrees (59 - 77). Like basalt columns, Earth's primordial crust formed with this pattern (78, 79). It controls today´s plate movements.

Spreading ridges meet at triple junctions. These can only exist if Earth is expanding (80 - 82).

Earth´s magnetic field, ocean floor magnetic stripes, World magnetic map (99 – 123) Pangaean reconstruction

Earth´s structures are fractal (91 – 98). They exist at all scales.

The Earth has a magnetic field (99), currently with a south pole in the north and vice versa. Theory is that it periodically reverses, producing magnetic striping of oceanic crust (101, 102).

A major pillar of PT is that sea floor magnetic stripes, sometimes attributed to magnetic field reversal (Vine & Mathews, 1965), others to high versus low intensity (Red Sea, open University; the famous Eltanin profile (Cox, 1973)) record spreading. They also occur in continental rifts. Vine & Mathews noted that magnetic contrasts in ocean crust could be explained, without reversals of Earth's magnetic field, by presence of strongly magnetized material adjacent to weakly magnetized material, a statement never repeated in subsequent literature (103 -106).

Magnetic stripes are calibrated on Iceland, for the last 4 Ma. (103 -106). Heirtzler et al. (1968) extrapolated the data to 34 stripes - 84 Ma (27x!) in the western South Atlantic (no mention was made of the 51 stripes (150 Ma??) in the Pacific west of S. America). They cautioned that this could involve possible error, and that if the Vine & Mathews 1963 theory were wrong, their conclusions were also.

Beloussov (1970) noted that the Vine & Mathews and Heirtzler ideas were major pillars of PT spreading theory.

Moving ever further offshore (144 – 123), seismic surveys reveal lightly stretched continental crust followed by thinning from 30 kilometers to less than 10 kilometers, and thence to highly extended crust, presumed continent-ocean boundaries and "oceanic" crust (see Karner, 2008 for detailed discussion of extension of 100's %). The crust is being stretched. That rules out ridge push as a spreading driver.

Extended crust carries asymmetric basins, 60 to 200 kilometers wide and up to 25 kilometers deep, where reflections, some with sedimentary architecture (truncation, onlap), dip toward bounding faults (seaward dipping reflections, SDRs). Here, magma rises to intrude sills and extrude basalt. Stretching results in serpentinization (with magnetite) of exhumed peridotite, generating magnetic anomalies unrelated to MOR spreading. They explain seafloor magnetic stripes (ref. Vine & Mathews, above). They do not record magnetic field reversals. This rules out the Heirtzler et al. 1968 extrapolation of magnetic stripes from Iceland (4Ma) to 84 Ma.

Serpentinization of shallow mantle peridotite olivine (the most abundant mineral) results in up to 45% volume increase and release of heat. Is this responsible in part for Earth expansion?

Deep sea drilling (8, see also 113) aimed at calibrating increasing age of oceanic crust away from MORs encountered basalts assumed to be "basement," but some contained sediment clasts and some deeper basalts were interbedded with sediments. Perhaps "oceanic" crust includes extended continental crust far offshore. Is there any evidence?

The Korhonen et al. (2007) Magnetic Anomaly Map of the World (see figure 2; James 2010, 2018) shows an important alternative to coastlines/bathymetric contours for Pangaean reconstruction (124 – 126). Large areas without magnetic stripes below the South Atlantic adjacent to South America and Africa supposedly record the Cretaceous Quiet Period, when magnetic field reversal paused for 40 million years. Similar magnetic signatures show they are foundered parts of adjacent continents. They reconstruct well. A similar signature appears off eastern North America where seafloor fractures that continue onshore to Palaeozoic/older Appalachian offsets indicate ancient, continental origins (see also, data from southern N America, above).

Numerous samples of continental crust have been retrieved from "oceanic" areas (128 – 129) (e.g., Storetvedt, 2003; Vasiliev and Yano, 2007; Yano et al., 2009). They are ignored or "explained" as glacial ***erratics*** or jettisoned ballast.

The Magnetic Anomaly Map of the World records very large areas of subsided continental crust James (2010b). They are not represented in palaeogeographic reconstructions. Pre-extension "Pangaea" was global.

Rocks as old as 2 billion years occur on the Mid-Atlantic Ridge Peter and Paul's Islands. Proterozoic-Paleozoic zircons occur in gabbros on the Mid-Atlantic Ridge. Continental isotopes are widespread in Indian Ocean basalts. Schneider & Johnson (1970) described salt diapirs from deep oceans, some from the western flank of the Mid-Atlantic Ridge.

Proterozoic zircons in lavas on Mauritius evidence ancient basement below the island and adjacent Mascarene Plateau. Torsvik et al. (2013) christened microcontinent "Mauritia" in 2013 (131). The Magnetic Anomaly Map indicates a large submerged continental area to the east. Mauritia is very large.

Proterozoic-Devonian zircons occur in Galapagos Islands lavas (Rojas-Agramonte, et al., 2016) a 20-million-year-old supposed hotspot 1,000 kilometers west of South America. Mesozoic zircons occur on Iceland, 13-15 million years old, on the Mid-Atlantic Ridge.

In 2013 granite was discovered on the ***NW*** - SE Rio Grande Ridge (outer edge of South America's magnetic extension). Basalts on the "conjugate" Walvis Ridge east of Africa show continental signature. Both are seen as migration tracks over the same Tristan da Cunha hot spot. They are oblique to seafloor fractures (flowlines). Both ridges are associated with those large extensions of neighboring continents and SDRs are present.

In 2017, Zealandia (130) was nominated as a newly recognized continent (Mortimer et al; see also, Luyendik, 1995). This fragmented, largely submerged area, as large as Australia, between Australia and New Zealand, explains plant and animal distributions in the South Pacific. There is much more, however. Magnetic data indicate very large extensions to the north and east. Permian-lower Cretaceous sandstones in New Zealand's eastern Torlesse Terrane, 3,500 kilometers long, 300 kilometers wide and 30 kilometers thick, came from here.

Ancient zircons occur on the SW Indian Ridge (Cheng, et al., 2016). Magnetic data show Madagascar to be continental and part of, not migrated from east Africa (131 – 133). We should not write off Lemuria or Atlantis (135,136)

Foulger et al. (2022) nominated Icelandi**a** and 10 other continental candidates (134).

Pangaean Reconstructions and Earth Size

Proliferating models of Pangaea, its breakup and dispersal show Increasing complexity, recognizing ever more small terranes and their migrations. Many include unlikely major changes in direction and/or plate rotations (56 – 58).

One objective, to model palaeoclimate and thence hydrocarbon source rock presence, requires knowledge of ocean currents. Mid-Jurassic/Miocene shallow-water deposits and subaerially weathered rocks, now 1 – 7 kilometers deep, in Deep Sea Drilling Project sites in the Atlantic, Indian and Pacific Oceans must have been influenced by these, but reconstructions do not show them. Those large subsided continental masses need to be taken into account as well; they do not appear on reconstructions.

Models show oceanic crust east of Japan and New Zealand and west of South America. But

Japan received sediments from the east in the Palaeozoic-Paleogene. Geological, geophysical and dredge data evidence Proterozoic and younger continental crust under northwestern Pacific abyssal plains. It subsided below deep sea at the end of the Jurassic, but you can still see it on the magnetic map. A million cubic kilometers of Devonian micaceous sediments in Bolivia and Argentina came from the west.

Reconstructions use a constant size Earth (137 – 140). Total length of mid-ocean ridge ocean crust creation, greater than subduction consumption, and triple junctions (earlier) evidence expansion. Triple junctions on the mid-ocean ridge that surrounds Antarctica evidence ridge extension. Coupled with separation of continents as they move northwards towards the equator, they give rise to four spreading ridges spaced at 90° (138) with a repeated pattern of N - S in the south and westerly convex curves in the north. We have to explain the geometry.

Fractures between Antarctica and Australia and Africa indicate NE migration of the latter. Fractures SW of S America indicate NW migration of SW Pacific crust. Fractures in the Central – N Atlantic indicate NW separation of N America from Africa. NEE fractures west of the Mid Pacific Rise show SSW separation of the western Pacific from N America.

Earth expansion.

Serpentinization of shallow mantle peridotite olivine (the most abundant mineral) results in up to 45% volume increase and release of heat. Is this responsible in part for Earth expansion.

Cluster II satellites record arrival of electrons, protons **and atoms in the solar wind. Earth's magnetic field focuses these earthwards**. Space-geodetic data show that the solid Earth expanded about 0.24 millimeters annually in recent decades (Shen et al., 2015). Growth increments on fossil corals and brachiopods show that days per year declined from 424 in the Middle Cambrian to 365 today (141 – 142). Like a pirouetting ballerina extending her arms, Earth grows and slows. Radial growth results in continental separation, extension and subsidence - continents separate radially; they do not drift circumferentially.

Origin of Continental Crust (143 – 158)

Intra-oceanic volcanic arcs are characterized by high silica andesite (named from the Andes of South America) with the same composition as continental rocks. This cannot derive from subducting slab low-silica basalt so we have an "andesite problem."

For PT, the rock reflects "new" continental crust formed by complex partial melting of sediments, the slab, the mantle or the mantle wedge (or combinations of these) in "subduction factories." This is where continental crust forms.

Recently discovered Proterozoic and Palaeozoic zircons produced by the volcanoes of and continental seismic velocities below island arcs Izu-Bonin, Luzon, Vanuatu, Solomon Islands, East Java and the Lesser Antilles show they are underpinned by original continent. There is no andesite problem and subduction factories are not required.

The arcs are highly curved, convex to the east, and segmented, reflecting radially dispersing blocks of continental crust. The data do not support active descent of oceanic crust (subduction). The arcs are overriding the ocean.

PT theory is supposed to explain the origin of mountains (160 – 167, 180 -183).

Africa is supposed to have moved 2-3,000 km northwards, pushing up the Alps (Dewey et al., 1989). The Africa – Europe boundary runs E-W. There are no mountains along its continuation in the Atlantic. The Alps and Carpathians carry European brachiopods. There is nothing African present.

India is supposed to have migrated 7,500 kilometers north across the Indian Ocean to push up the Himalayas, but fossils relate India to Eurasia. Head-on collision of far travelled continents is not indicated. Perhaps strike-slip plays a role.

Major mountains (Andes, Alaska, western N America, east Siberia) occur where collision does not occur.

Mountains are supposed to have roots. Molnar (1992) stated that the image of a lithospheric root mirroring the overlying topographic high is more belief than fact. Meissner (1986) pointed out that only young (Cenozoic) mountains have roots. The Caledonides, Appalachians and Variscides have flat Moho discontinuities. The Moho migrates upwards, equilibrating with pressure and temperature.

Unlike the Atlantic, the Pacific is markedly asymmetric – the East Pacific Rise (EPR) approaches South America and converges with North America. Magnetic data indicate large areas of extended, subsided continent west of the Rise but none to the east. Here, strike-slip dominates plate interaction.

Extended/thinned continental crust is perhaps easily thrust onto continental margins. This results from transpression associated with strike-slip faults.

Since the EPR hit the trench Pacific/North America strike-slip motion has occurred along the San Andreas Fault. From Alaska to Mexico the North American Cordillera carries ***far-travelled*** (hundreds of kilometers) distal/oceanic thrust sheets, detached from subducted Pacific crust to overly Precambrian-Mesozoic shelf sequences.

Similarly, large amounts of conglomerates/sandstones in the Andes came from the Pacific. Crustal thicknesses here**,** up to 70 kilometers, speak of merger. Paleozoic and Mesozoic troughs in Peru, with steep western boundaries and gentle eastern slopes, contain 10-12 kilometer thick prisms of shallow to deepwater deposits (basinward velocity decline would generate upward concave SDRs). Bounding growth faults acted as volcanic conduits. They resonate with those asymmetric basins seen on deepwater seismic.

These “vanished continents“ once linked North America, southeast Asia, Australia and South America. They explain plant and animal fossil distributions and resolve biodispersal problems.

Blueschists (168 - 179) - (high-pressure/low temperature metamorphism) are seen as classic indicators of fossil subduction zones, involving descent of material to 40–80 kilometers over millions of years, metamorphism, and then unexplained resurrection. However, radiometric data suggest metamorphism only slightly younger than predecessor rocks. There are no blueschists in the Central American or Lesser Antilles subduction arcs. Along the north and south Caribbean margins, metamorphism increases and high-pressure/low-temperature rocks occur close to strike slip faults. Some are even interbedded with sedimentary equivalents.

ParagraphThere is an informative, highly dynamic, current strike-slip laboratory along northern South America (173 - 179). Dextral offset since the Eocene has generated eastward-younging foreland basins followed by inversion into overriding uplifts (James, 2009a).

The 200 milligal negative gravity anomaly, the world’s largest at sea level, over the eastern, Maturín – Columbus Basin suggests a root **with~~out~~** a mountain yet to arrive (the northern Coastal and Interior ranges). Major hydrocarbon reserves occur here. Industry data (sediment thickness, overpressures, low heat flow) point to blueschist conditions at depth.

ParagraphThe 210 milligal positive anomaly over Colombia's 5,800 meter Sierra Nevada de Santa Marta, the world's highest ocean-side mountain, indicates a mountain without a root, overriding the Caribbean.

The Mérida Andes, also strike-slip related, lie halfway over the 150 milligal negative gravity anomaly in the southern Maracaibo Basin – the mountain is arriving over its root. It has already covered the Guarumen Basin and inversion further north exposes blueschists in the Coastal Range. Thick, graphitic rocks here record former hydrocarbon systems.

Summary (184 – 191)

Published PT is complacent and replete with unlikely models. It should respect and adapt to data, include multiple working hypotheses and enable students to think and choose.

If not, the writing in stone will eventually read "RIP."

References, including those in the accompanying PowerPoint File

Beloussov, V. V., 1970, Against the hypothesis of ocean-floor spreading: Tectonophysics, v. 9, p.489-511.

Cheng, H., H. Zhou, Q. Yang, L. Zhang, F. Ji and H. Dick, 2016, Jurassic zircons from the Southwest Indian Ridge: Scientific Reports, open.9p.

Cloos, H., 1948, The ancient European basement blocks-preliminary note: Am. Geoph. Union Trans., v.29, p. 99-103.

Clouard, V. and A. Bonneville, 2005, Ages of seamounts, island, and plateaus on the Pacific plate: In: Foulger, G. R., J. H. Natland, D. C. Presnall and D. L. Anderson (Eds.), Plates, plumes, and paradigms, GSA Special Paper 388, p. 71 - 90.

Cox, A., 1973, Plate Tectonics and Geomagnetic Reversals: Freeman, San Francisco. 702 p.

Dewey, J. F., M. L. Helman, E. Turco, D. H. W. Hutton and S. D. Knott, 1989, Kinematics of the western Mediterranean: In: Coward, M.P., D. Dietrich and R. G. Park (eds.) Alpine Tectonics, Geological Society, London, Special Publication 45, 265-283.

Escalona, A. and P. Mann, 2006, An overview of the petroleum system of Maracaibo Basin: AAPG Bull., v. 90, p. 657-678.

Foulger, G. R., L. Gernigon, and I Geoffroy, 2022, Icelandia: In: Foulger et al., 2022, In the footsteps of Warren B. Hamilton: New Ideas in Earth Science, GSA Sp. Paper 553, p. 29-40.

Heirtzler, J. R., G. O. Dickson, E. M. Herron, W. C. Pitman III and X. Le Pichon, 1968, Marine magnetic anomalies, geomagnetic field reversals, and motions of the ocean floor and continents: **J.** Geophysical Research, v. 73, issue 6, p. 2119-2136.

Heirtzler, J. R., G. O. Dickson, E. M. Herron, W. C. Pitman III and X. Le Pichon, 1968, Marine Magnetic Anomalies, Geomagnetic Field Reversals, and Motions of the Ocean Floor and Continents: J. Geophysical Research, v. 73, no. 6, p. 2119-2136.

Hess, H. H.,1960, Nature of the great oceanic ridges: Preprints of the 1st International Oceanographic Congress (New York, August 31-September 12, 1959). Washington: American Association for the Advancement of Science. (A). pp. 33–34.

Hess, H. H., 1962, History of Oceanic Basins, Petrologic studies, A Volume In Honour of A.F. Buddignton In A. E. J. Engel, Harold L. James, and B. F. Leonard: GSA, p. 599-620.

Holmes, A., 1944, 45, Principles of Physical Geology: Thomas Nelson and Sons Ltd., 532p.

James, K. H., The Venezuelan Hydrocarbon Habitat, Part 1: Tectonics, Structure, Palaeogeography and Source Rocks, J. Petroleum Geology, c.23 (1), p. 5-53.

James, K. H., 2007, Structural Geology: from local elements to regional synthesis: In: Bundschuh, J. and G. E. Alvarado (eds.) Central America: Geology, Resources and Hazards, Ed. Balkema, Chapter 11, p. 277-321.

James, K. H., 2010, Observations on new magnetic map from the Commission for the Geological Map of the World, New Concetpts in Global Tectonic, no. 57.

James, K. H., 2018, "Intra-oceanic¨volcanic arcs; Lesser Antilles and Central America arcs": AAPG Hedberg Conference, 2-5 July, Sig enza, Spain, abstracts, p. 52-53.

James, K. H., 2018, Plate Tectonics at 50: Not Written In Stone, AAPG Explorer, February, p. 18 – 24.

James, K. H., 2018, Middle America – intracontinental extension along ancient structures: AAPG Hedberg Conference, 2-5 July, Sigüenza, Spain, abstracts, p. 49.

Karner, G. D., 2008, Depth-dependent extension and mantle exhumation: an extreme passive margin end-member or a new paradigm? Central Atlantic Conjugate Margin Conference, Halifax, Canada, Extended abstract, 10-16.

Karner, G. D. and A. B. Watts, 1983, Gravity Anomalies and Flexure of the Lithosphere at Mountain Ranges: J. Geophys. Res.,v. 88, no. B12, p. 10,447-10.477.

King, L.C, 1983, Wandering Continents and Spreading Sea Floors on an Expanding Earth: J. Wiley & Sons, 232p.

Kopp H., W. Weinzierl, A. Becel, P. Charvis, M. Evain, E. R. Flueh, A. Gailler, A. Galve, A. Hirn, A. Kandilarov, D. Klaeschen, M. Laigle, C. Papenberg, L. Planert and E. Roux, 2011, Deep structure of the central Lesser Antilles Island Arc: Relevance for the formation of continental crust: Earth Planet. Sci. Lett. v. 304 (1–2), p. 121–134.

Korhonen, J. V., J. D. Fairhead, M. Hamoudi, K. Hemant, V. Lesus, M. Mandea, S. Maus, M. Purucker, D. Ravat, T. Sazonova and E. Thebault, 2007, Magnetic Anomaly Map of the World, 1:50,000,000: Commission for the Geological Map of the World, Paris.

Luyendyk, B. P., 1995, Hypothesis for Cretaceous rifting of east Gondwana caused by subducted slab capture: Geology, v. 23 , no. 4, p. 373–376.

McCall, R. A., 1997, Implications of recent geological investigations of the Mozambique Channel for the mammalian colonization of Madagascar Proc. R. Soc. Lond. B, v. 264, p. 663-665.

Meissner, R., 1986, Continental Geophysics: The Continental Crust. A Geophysical Approach: International Geophysics Series, v., 34. p. 206.
Molnar, P., 1992, Crust in mantle overdrive: Nature, v. 358, p. 105-106.

Meyerhoff, A. A. and H. A. Meyerhoff, 1972, "The new global tectonics": age of linear magnetic anomalies of ocean basins: AAPG Bull., v. 56, p. 337-359.

Moody, J.D., 1973, Petroleum Exploration Aspects of Wrench-Fault Tectonics: AAPG Bull. v. 57, no. 3, p.449–476.

Mortimer, N., H. J. Campbell, A. J. Tulloch, P. R. King, V. Stagpooel R. A. Wood, M. S. Rattenbury, R. Sutherland, C. J. Adams, J. Collot and M. Seton, 2017, Zealandia: Earth´s HIdden Continent: GSA Today, v. 27, issue 3, p. 27-35.

Nur, A. and Z. Ben-Avraham, 1977, Lost Pacifica continent: Nature, v. 270, p. 41 - 43.

Oreskes (Ed.), Plate Tectonics: An Insider's History of the Modern Theory of the Earth, Westview Press, Boulder, Colorado, p. 3-27.

Pindell, J., M. C. Ernesto, A. Ceron and L. Hernandez, 2016, Aeromagnetic Map Constrains Jurassic-Early Cretaceous Synrift, Break Up, and Rotational Seafloor Spreading History in the Gulf of Mexico : In: Lowry, C. D., et al, (Eds:) Mesozoic of the Gulf Rim and Beyond: New Progress in Science and Exploration of the Gulf of Mexico Basin, SEPM 35 th Ann. Res. Conf., p. 1-24.

Pratt, D.., 2000, Plate Tectonics: A Paradigm Under Threat10: J. Scientific Exploration, v. 14, no. 3, p. 307—352.10.

Rabinowitz, P., and S. Woods, 2006, The Africa–Madagascar connection and mammalian migrations: J. of African Earth Sciences, v. 44, issue 3, p. 270-276.

Rojas-Agramonte, Th. Toulkeridis, A. Kröner, T. Kemp, A. Garcia-Casco, N. Suhr, H. Xie and D. Liu, Palaeozoic to Archaean zircons in rocks derived from the Galapagos mantle hotspot: where do they come from? American Geosciences Institute, 35th Int. Geol. Congress, Abstracts, Paper Number: 5295.

Sandwell, D. T., R. D. Muller, E. H. F. Smith, E. Garcia and R. Francis, 2014, New global marine gravity model from CryoSat-2 and Jason-1 reveals buried tectonic structure: Science, v. 345, issue 6205, p. 65-67.

Sapin, F., J.-C- Ringenbach and C. Clerc, 2021, Rifted margins classification and forcing parameters: Nature, Scientific Reports, p. 1 - 17

Schneider, E. D. and G. L. Johnson, 1970, Deep-Ocean Diapir Occurrences: AAPG Bull., v. 54, no. 11, p. 2151-2169.

Shen, W., S. Ziyu , S. Rong and B. Yuri, 2015, Evidences of the expanding Earth from space-geodetic data over solid land and sea level rise in recent two decades: Geodesy and Geodynamics, v. 6, Issue 4, p. 248–252.

Smoot, N. C., 2012, Tectonic Globalony, Closing: AuthorHouse, Bloomington IN 47403, 157p.).

Stephenson, R., 2017, Intraplate orogenesis: Eurekan Orogen: Geological Society of London, William Smith Meeting 2017, Plate Tectonics at 50, Abstracts, p. 80.

Storetvedt, K., 2003. Global Wrench Tectonics. Fagbokforlaget, Poland, 397p.

Sylvester, A. G., 1988, Strike-slip faults: GSA Bull., v. 100, p. 1666-1703.

Thomas, W. A., 2014, A Mechanism for tectonic Inheritance at Transform Faults of the Iapetan Margin of Laurentia: Geoscience Canada, v. 41, p. 321-344.

Torsvik, T. H., H. Amunden, E. H. Hartz, F. Corfu, N. Kuznir, C. Gaina, P. V. Doubrovine, B. Steinberger, L. D. Ashwal and B. Jamtveit, 2013, A Precambrian microcontinent in the Indian Ocean: nature geoscience, v. 6, p. 223-227.

Vasiliev, B.I. and Yano, T., 2007. Ancient and continental rocks discovered in the ocean floors. New Concepts in Global Tectonics Newsletter , no. 43, p. 3-17.

Van der Voo, R., 1969, Paleomagnetic evidence for the rotation of the Iberian Peninsula: Tectonophysics, v. 7, issue 1, p. 5-56.

Vine, F. J. and D. H. Matthews, 1963, Magnetic anomalies over ocean ridges: Nature, v. 199, p. 947-949.

Wegener, A., 1924, The Nature of the Drift Theory and Its Relationship to Hitherto Prevalent Accounts of Changes in the Earth's Surface Configuration in Geological Times: In: The Origin of Continents and Oceans, 3rd edition Methuen, London, 212p.

Westbrook, G. K., J. W. Ladd, P. Buhl, N. Bangs and G. J. Tiley, 1988, Cross section of an accretionary wedge: Barbados Ridge complex: Geology, v. 16, no. 87, p. 631-635.

Wilson, J. T., 1965, A New Class of Faults and their Bearing on Continental Drift: Nature, v. 207, p. 343-347.

Wood, L. J., 2000, Chronostratigraphy and Tectonostratigraphy of the Columbus Basin, Eastern Offshore Trinidad: AAPG Bull., v. 84, no. 12, p. 1905-1928

Yano, T., Choi, D.R., Gavrilov, A.A., Miyagi, S. and Vasiliev, B.I., 2009. Ancient and continental rocks in the Atlantic
Ocean. New Concepts in Global Tectonics Newsletter , no. 53, p. 4- 37.

Zhirov, N. 1970 Atlantis: Atlantology: Basic Problems, UIV Press of the Pacific, reprinted from 1970 edition.

ABOUT THE NCGT JOURNAL

The NCGT Newsletter, the predecessor of the NCGT Journal, was begun as a result of discussions at the symposium “Alternative Theories to Plate Tectonics” held at the 30th International Geological Congress in Beijing in August 1996. The name is taken from an earlier symposium held in association with the 28th International Geological Congress in Washington, D. C. in 1989. The first issue of the NCGT Newsletter was December 1996. The NCGT Newsletter changed its name in 2013 to the NCGT Journal. Aims of the NCGT Journal include:

1. Providing an international forum for the open exchange of new ideas and approaches in the fields of geology, geophysics, solar and planetary physics, cosmology, climatology, oceanography, electric universe, and other fields that affect or are closely related to physical processes occurring on Earth from its core to the top of its atmosphere.

2. Forming an organisational focus for creative ideas not fitting readily within the scope of dominant tectonic models.

3. Forming the basis for the reproduction and publication of such work, especially where there has been censorship or discrimination.